AN ABSTRACT OF THE DISSERTATION OF

Nathan J. Slegers for the degree of Doctor of Philosophy in Mechanical Engineering presented on June 25, 2004.

Title: Dynamic Modeling, Control Aspects and Model Predictive Control of a Parafoil and Payload System.

Abstract approved: Redacted for privacy

Mark F. Costello

Control issues are investigated for a parafoil and payload system with left and right parafoil brakes used as the control mechanism. It is shown through dynamic modeling and simulation that parafoil and payload systems can exhibit two basic modes of lateral control, namely, roll and skid steering. Using a small parafoil and payload aircraft, glide rates and turn performance were measured and compared against a 9 DOF simulation model. This work shows that to properly capture control response of parafoil and payload aircraft, tilt of the parafoil canopy must be accounted for along with left and right parafoil brake deflection. Alternative methods of controlling a parafoil and payload by tilting the canopy for lateral control and changing rigging angle for longitudinal control are evaluated. A model predictive control strategy is developed for an autonomous parafoil and payload system. It is demonstrated in flight tests that a model predictive control strategy is a natural and effective method of achieving trajectory tracking in a parafoil and payload system.

Dynamic Modeling, Control Aspects and Model Predictive Control of a Parafoil and Payload System

by

Nathan J. Slegers

A DISSERTATION

submitted to

Oregon State University

in partial fulfillment of

the requirements for the

degree of

Doctor of Philosophy

Presented June 25, 2004

Commencement June 2005

Doctor of Philosophy dissertation of Nathan J. Slegers presented on June 25, 2004.

APPROVED:

Redacted for privacy

Major Professor, representing Mechanical Engineering

Redacted for privacy

Head of the Department of Mechanical Engineering

Redacted for privacy

Dean of the Graduate School

I understand that my dissertation will become part of the permanent collection of Oregon State University libraries. My signature below authorizes release of my dissertation to any reader upon request.

Redacted for privacy

Nathan J. Slegers, Author

TABLE OF CONTENTS

TABLE OF CONTENTS (Continued)

TABLE OF CONTENTS (Continued)

TABLE OF CONTENTS (Continued)

LIST OF FIGURES

LIST OF FIGURES (Continued)

LIST OF FIGURES (Continued)

LIST OF FIGURES (Continued)

LIST OF FIGURES (Continued)

LIST OF TABLES

DYNAMIC MODELING, CONTROL ASPECTS AND MODEL PREDICTIVE CONTROL OF A PARAFOIL AND PAYLOAD SYSTEM

GENERAL INTRODUCTION

A parafoil and payload configuration is lightweight, flies at low speed, provides "soft" landing capability, and is compact before deployment. As the name suggests, the vehicle is comprised of a parafoil canopy connected to a payload body with suspension lines. Control is commonly achieved by two primary means, namely, deflection of left and right parafoil brakes and movement of the mass center of the complete system. Parafoil and payload aircraft are also particularly well suited as autonomous air vehicles for sensing applications. For autonomous control, each individual sensor payload is fitted with an inexpensive guidance and control module. These air vehicles can be released at altitude from a delivery aircraft and have a larger payload capacity and similar packed dimensions compared to micro aircraft.

Implementation of autonomous control on parafoil and payload systems requires a fundamental understanding of how the system is controlled. Modeling the parafoil and payload system is a necessary step in the investigation of how the parafoil and payload respond to different control inputs. This work investigates three models that were created to represent the dynamics of the parafoil and payload system. The first model has 9 degrees-of-freedom (DOF), including three inertial positions as well as the three Euler orientation angles of the parafoil canopy and the payload. Panels are used for modeling the canopy in the 9 DOF model allowing for detailed investigation of control effects. The second is a 6 DOF model that assumes the parafoil and payload cannot rotate independently and reduces the aerodynamics to lumped coefficients including effects of both canopy and parafoil. The final model is a reduced order linearized version of the 6 DOF model that includes only the body roll and yaw angles. The parafoil and payload models were verified with flight data and used to investigate the feasibility of canopy tilting and dynamic rigging as alternative control methods.

Aviation enthusiasts commonly use parafoils as recreational air vehicles. In this case, the pilot pulling down on the right and left side control lines deflects the

right and left parafoil brakes. The pilot through appropriate body movement changes the center of mass of the system. The dynamics are sufficiently slow such that expert paraglider pilots can track a desired trajectory and attain accurate ground impact. Subconsciously these pilots continuously project the trajectory forward in time and compare the results with the desired path. The error between the projected and desired path are used to determine control action. A control strategy that mimics how human pilots control paragliders is model predictive control. In model predictive control, a dynamic model of the system is used to project the state into the future and subsequently used to estimate future states and determine control action. It has been verified through flight tests that model predictive control is a practical and powerful control technique when future reference states are known or can be estimated.

ASPECTS OF CONTROL FOR A PARAFOIL AND PAYLOAD SYSTEM

Nathan Slegers and Mark Costello

Journal of Guidance, Control and Dynamics
1801 Alexander Bell Drive, Suite 500
Reston, VA 20191
Vol. 26, No. 6, December 2003

ASPECTS OF CONTROL FOR A PARAFOIL AND PAYLOAD SYSTEM

Nathan Slegers,* Mark Costello†
Department of Mechanical Engineering
Oregon State University
Corvallis, Oregon 97331

ABSTRACT

A parafoil controlled by parafoil brake deflection offers a lightweight and space efficient control mechanism for autonomous placement of air dropped payloads to specified ground coordinates. The work reported here investigates control issues for a parafoil and payload system with left and right parafoil brakes used as the control mechanism. It is shown that parafoil and payload systems can exhibit two basic modes of lateral control, namely, roll and skid steering. These two modes of lateral steering generate lateral response in opposite directions. For example, a roll steer configuration turns left when the right parafoil brake is activated while a skid steer configuration turns right under the same control input. In transition between roll and skid lateral steering, the lateral response is zero and the system becomes uncontrollable. Angle of incidence, canopy curvature of the parafoil and magnitude of brake deflections are important design parameters for a controllable parafoil and payload system and greatly effect control response, including whether the basic lateral control mode is roll or skid steering. It is shown how the steering mode switches when fundamental design parameters are altered and as the magnitude of the brake deflection increases. The mode of directional control transitions towards roll steering as the canopy curvature decreases or the angle of incidence becomes more negative. The mode of directional control transitions away from the roll steering mode as the

---

* Graduate Research Assistant, Department of Mechanical Engineering, Member AIAA.
† Assistant Professor, Department of Mechanical Engineering, Member AIAA.

magnitude of the brake deflection increases and for "large" brake deflections most parafoils will always skid steer.

NOMENCLATURE

x, y, z : Components of position vector of point C in an inertial frame.

ϕ_b, θ_b, ψ_b : Euler roll, pitch and yaw angles of payload.

ϕ_p, θ_p, ψ_p : Euler roll, pitch and yaw angles of parafoil.

$\tilde{\phi}_b, \tilde{\theta}_b, \tilde{\psi}_b$: Payload Euler roll, pitch and yaw angles for roll constraint moment computation.

$\tilde{\phi}_p, \tilde{\theta}_p, \tilde{\psi}_p$: Parafoil Euler roll, pitch and yaw angles for roll constraint moment computation.

$\dot{x}, \dot{y}, \dot{z}$: Components of velocity vector of point C in an inertial frame.

p_b, q_b, r_b : Components of angular velocity of payload in payload reference frame (b).

p_p, q_p, r_p : Components of angular velocity of parafoil in parafoil reference frame (p).

m_b, m_p : Mass of payload and parafoil.

F_{xc}, F_{yc}, F_{zc} : Components of joint constraint force in an inertial frame.

M_{xc}, M_{yc}, M_{zc} : Components of joint constraint moment in an inertial frame.

u_i, v_i, w_i : Components of relative air velocity of aerodynamic center of panel i in i^{th} frame.

V_s : Magnitude of velocity vector of mass center of payload.

u_b, v_b, w_b : Components of relative air velocity of mass center of payload in payload reference frame.

u_A, v_A, w_A : Components of relative air velocity of apparent mass center in parafoil reference frame.

x_{cb}, y_{cb}, z_{cb}: Components of vector from point C to mass center of payload in payload reference frame.

x_{cp}, y_{cp}, z_{cp}: Components of vector from point C to mass center of parafoil in parafoil reference frame.

x_{ca}, y_{ca}, z_{ca}: Components of vector from point C to apparent mass center in parafoil reference frame.

x_{pa}, y_{pa}, z_{pa}: Components of vector from parafoil mass center to apparent mass center in parafoil reference frame.

I_b, I_p: Inertia matrix of payload and parafoil.

I_F, I_M: Apparent mass force and moment coefficient matrices.

C_D^b: Drag coefficient of payload.

C_{Li}: Lift coefficient of i^{th} panel of parafoil canopy.

C_{Di}^p: Drag coefficient of i^{th} panel of parafoil canopy.

η: Angle of incidence

K_c, C_c: Rotational stiffness and damping coefficients of joint C.

A_b: Payload reference area.

A_i: Reference area of i^{th} panel of parafoil canopy.

T_p: Transformation matrix from inertial reference frame to parafoil reference frame.

T_b: Transformation matrix from inertial reference frame to payload reference frame.

T_i: Transformation matrix from i^{th} panel's reference frame to parafoil reference frame.

T_{ti}: Transformation matrix from inertial reference frame to i^{th} command trajectory reference frame.

ψ_{t_i}: Angle between inertial reference frame and i^{th} command trajectory reference frame.

F_A^b, F_A^p : Aerodynamic force on payload and parafoil in their respective frames.

M_A : Moment on parafoil due to steady aerodynamic forces.

M_{UA} : Moment on payload due to unsteady aerodynamic forces.

INTRODUCTION

To produce rapidly deployable and ready fighting units, weapon system developers have recognized the driving need to quickly station large numbers of soldiers, along with their equipment in low density over a large land area. Use of this troop and equipment deployment strategy requires autonomous air delivery of many individual equipment packages to specific rendezvous points. One concept to realize this goal is to equip each individual package with a parafoil and inexpensive guidance and control module so that each package can steer itself to a prespecified rendezvous point after release from a delivery aircraft.

Detailed dynamic simulation of the flight mechanics of parachute and load systems appear to have commenced with the work of Wolf [1] who considered the stability of a parachute connected to a load. Using a 10 degree-of-freedom (DOF) representation, Wolf established that stability is reduced as riser length is increased or parachute weight is increased, and that stability is improved by increasing parachute axial and normal aerodynamic force. Later, Doherr and Schilling [2] reported on the development of a 9 DOF dynamic model. By comparing results from 6 and 9 DOF models they conclude a 9 DOF adequately predicts stability characteristics. Furthermore, their work established the sensitivity of the motion of a parachute and load system to atmospheric winds. Hailiang and Zizeng [3] used a 9-degree of freedom model to study the motion of a parafoil and payload system. In contrast to Doherr and Schilling, they reported only small differences in the motion and stability between 6 and 9 DOF dynamic models. In studying stability characteristics as a function of the pitch inertia of the payload, Hailiang and Zizeng found the decay ratio

and period increase as pitch inertia is increased. Iosilevskii [4] established center of gravity and lift coefficient limits for a gliding parachute. Brown [5] analyzed the effects of scale and wing loading on a parafoil using a linearized model based on computer calculated aerodynamic coefficients.[5] Brown found that steady state turn response of small parafoils is more sensitive to control inputs than larger parafoils. More recent efforts by Zhu, Moreau, Accorsi, Leonard, and Smith [6] as well as Gupta, Xu, Zhang, Accorsi, Leonard, Benney, and Stein [7] have incorporated parafoil structural dynamics into the dynamic model of a parachute and payload system. A significant amount of literature has been amassed in the area of experimental parafoil dynamics beginning with Ware and Hassell [8] who investigated ram-air parachutes in a wind tunnel by varying wing area and wing chord. More recently extensive flight tests have been reported on NASA's X-38 parafoil providing steady-state data and aerodynamics for large-scale parafoils [9], [10]. This paper considers a payload that has an attached parafoil with brakes used as the control mechanism. Using a dynamic modeling approach similar to Doherr and Schilling and Hailiang and Zizeng, stability and control characteristics of this system are examined. Particular attention is paid to steady state control response as a function of fundamental design parameters such as parafoil canopy geometry, angle of incidence and varying control deflection.

PARAFOIL AND PAYLOAD DYNAMIC MODEL

Figure 1.1 shows a schematic of the dynamic system that consists of a payload body connected to a parafoil canopy. A constant velocity joint couples the parafoil and payload components at point C. The inertial frame shown in Figure 1.1 is fixed to the surface of the earth.

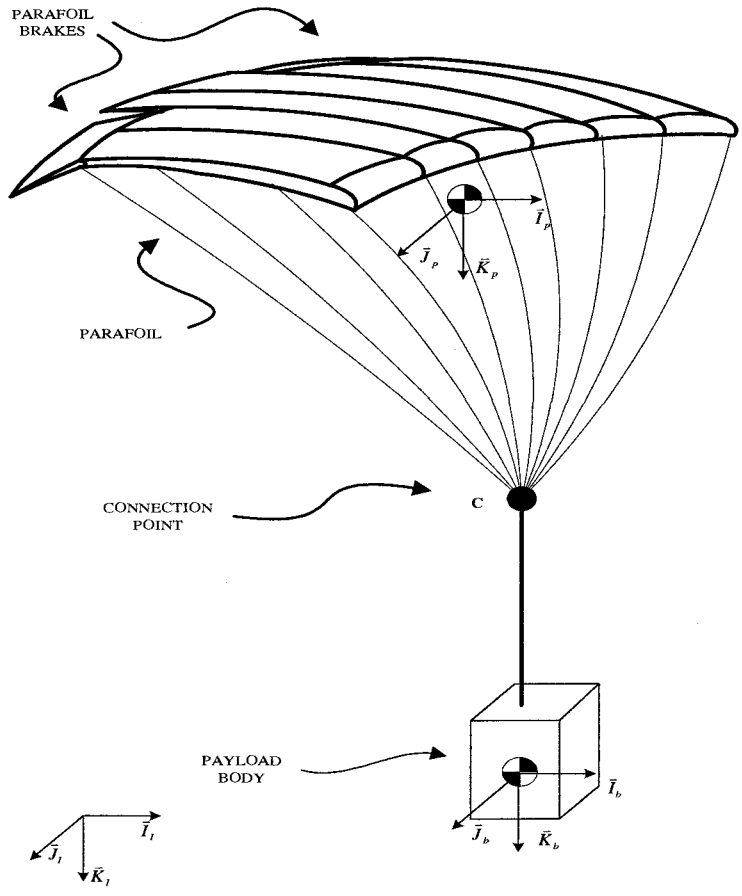

Figure 1.1 Parafoil and Payload system

With the exception of movable parafoil brakes, the parafoil canopy is considered to be a fixed shape once it has completely inflated. Figures 1.2 and 1.3 show a schematic of the parafoil canopy geometry. Connected to each panel are brakes that change the aerodynamic loads on the parafoil when they are deflected.

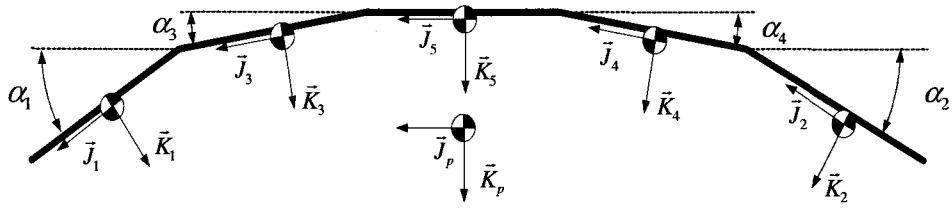

Figure 1.2 Parafoil Canopy Geometry

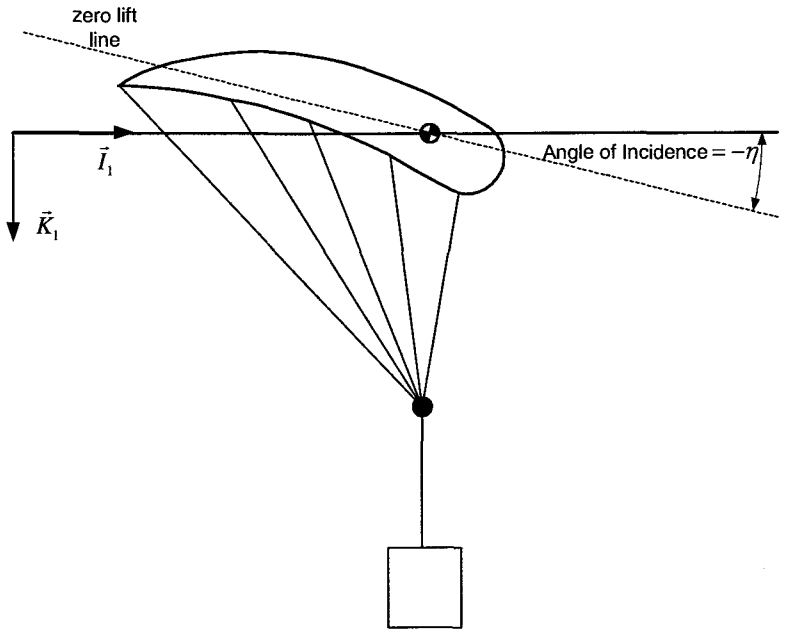

Figure 1.3 Angle of incidence

The parafoil canopy is connected to joint C by a rigid massless link from the mass center of the canopy. The payload is connected to joint C by a rigid massless link from the mass center of the payload. Both the parafoil and the payload are free to rotate about joint C but are constrained by the force and moment at the joint. The combined system of the parafoil canopy and the payload are modeled with 9 DOF, including three inertial position components of the joint C as well as the three Euler orientation angles of the parafoil canopy and the payload. The kinematic equations for the parafoil canopy and the payload are provided in Equations 1 through 3.

$$\begin{Bmatrix} \dot{x}_c \\ \dot{y}_c \\ \dot{z}_c \end{Bmatrix} = \begin{Bmatrix} u_c \\ v_c \\ w_c \end{Bmatrix} \tag{1}$$

$$\begin{Bmatrix} \dot{\phi}_b \\ \dot{\theta}_b \\ \dot{\psi}_b \end{Bmatrix} = \begin{bmatrix} 1 & s_{\phi_b} t_{\theta_b} & c_{\phi_b} t_{\theta_b} \\ 0 & c_{\phi_b} & -s_{\phi_b} \\ 0 & s_{\phi_b}/c_{\theta_b} & c_{\phi_b}/c_{\theta_b} \end{bmatrix} \begin{Bmatrix} p_b \\ q_b \\ r_b \end{Bmatrix} \tag{2}$$

$$\begin{Bmatrix} \dot{\phi}_p \\ \dot{\theta}_p \\ \dot{\psi}_p \end{Bmatrix} = \begin{bmatrix} 1 & s_{\phi_p} t_{\theta_p} & c_{\phi_p} t_{\theta_p} \\ 0 & c_{\phi_p} & -s_{\phi_p} \\ 0 & s_{\phi_p}/c_{\theta_p} & c_{\phi_p}/c_{\theta_p} \end{bmatrix} \begin{Bmatrix} p_p \\ q_p \\ r_p \end{Bmatrix} \tag{3}$$

The dynamic equations are formed by first separating the system at the coupling joint, exposing the joint constraint force and moment acting on both bodies. The translational and rotational dynamics are inertially coupled because the position degrees of freedom of the system are the inertial position vector components of the coupling joint. The constraint force is a quantity of interest to monitor during the simulation so it is retained in the dynamic equations rather than being algebraically eliminated. Equation 4 represents the translational and rotational dynamic equations of both the parafoil and payload concatenated into matrix form.

$$\begin{bmatrix} -m_b S_c^b & 0 & m_b T_b & -T_b \\ 0 & -I_F S_c^a - m_p S_c^p & I_F T_p + m_p T_p & T_p \\ I_b & 0 & 0 & S_c^b T_b \\ 0 & I_M + I_p - S_p^a I_F S_c^a & S_p^a I_F T_p & -S_c^p T_p \end{bmatrix} \begin{Bmatrix} \dot{p}_b \\ \dot{q}_b \\ \dot{r}_b \\ \cdots \\ \dot{p}_p \\ \dot{q}_p \\ \dot{r}_p \\ \cdots \\ \ddot{x}_c \\ \ddot{y}_c \\ \ddot{z}_c \\ \cdots \\ F_{xc} \\ F_{yc} \\ F_{zc} \end{Bmatrix} = \begin{Bmatrix} \mathrm{B}_1 \\ \mathrm{B}_2 \\ \mathrm{B}_3 \\ \mathrm{B}_4 \end{Bmatrix} \tag{4}$$

The matrix in Equation 4 is a block 4 x 4 matrix where each element is a 3 x 3 matrix. Rows 1-3 in Equation 4 are forces acting on the payload mass center expressed in the payload frame and rows 7-9 are the moments about the payload mass center also in the payload frame. Rows 4-6 in Equation 4 are forces acting on the parafoil mass center expressed in the parafoil frame and rows 10-12 are the moments about the parafoil mass center also in the parafoil frame. The S_i^j matrices are cross product operator matrices, working on different vectors from i to j associated with the system configuration.

$$S_i^j = \begin{bmatrix} 0 & -z_{ij} & y_{ij} \\ z_{ij} & 0 & -x_{ij} \\ -y_{ij} & x_{ij} & 0 \end{bmatrix} \tag{5}$$

The matrix T_b represents the transformation matrix from an inertial reference frame to the payload reference frame,

$$T_b = \begin{bmatrix} c_{\theta_b} c_{\psi_b} & c_{\theta_b} s_{\psi_b} & -s_{\theta_b} \\ s_{\phi_b} s_{\theta_b} c_{\psi_b} - c_{\phi_b} s_{\psi_b} & s_{\phi_b} s_{\theta_b} s_{\psi_b} + c_{\phi_b} c_{\psi_b} & c_{\theta_b} s_{\phi_b} \\ c_{\phi_b} s_{\theta_b} c_{\psi_b} + s_{\phi_b} s_{\psi_b} & c_{\phi_b} s_{\theta_b} s_{\psi_b} - s_{\phi_b} c_{\psi_b} & c_{\phi_b} c_{\theta_b} \end{bmatrix} \tag{6}$$

while, T_p represents the transformation matrix from an inertial reference frame to the parafoil reference frame.

$$T_p = \begin{bmatrix} c_{\theta_p} c_{\psi_p} & c_{\theta_p} s_{\psi_p} & -s_{\theta_p} \\ s_{\phi_p} s_{\theta_p} c_{\psi_p} - c_{\phi_p} s_{\psi_p} & s_{\phi_p} s_{\theta_p} s_{\psi_p} + c_{\phi_p} c_{\psi_p} & c_{\theta_p} s_{\phi_p} \\ c_{\phi_p} s_{\theta_p} c_{\psi_p} + s_{\phi_p} s_{\psi_p} & c_{\phi_p} s_{\theta_p} s_{\psi_p} - s_{\phi_p} c_{\psi_p} & c_{\phi_p} c_{\theta_p} \end{bmatrix} \tag{7}$$

The common shorthand notation for trigonometric functions is employed where $\sin(\alpha) \equiv s_\alpha$, $\cos(\alpha) \equiv s_\alpha$ and $\tan(\alpha) \equiv t_\alpha$. The matrices I_b and I_p represent the mass moment of inertia matrices of the payload and the parafoil body with respect to their respective mass centers and the matrices I_F and I_M represent the apparent mass force coefficient matrix and apparent mass moment coefficient matrix respectively.

$$I_F = \begin{bmatrix} A & 0 & 0 \\ 0 & B & 0 \\ 0 & 0 & C \end{bmatrix} \tag{8}$$

$$I_M = \begin{bmatrix} I_A & 0 & 0 \\ 0 & I_B & 0 \\ 0 & 0 & I_C \end{bmatrix} \tag{9}$$

Equations 10 through 13 provide the right hand side vector of Equation 4.

$$\mathrm{B}_1 = W_b + F_A^b - m_b S_w^b S_w^b \begin{Bmatrix} x_{cb} \\ y_{cb} \\ z_{cb} \end{Bmatrix} \tag{10}$$

$$\mathrm{B}_2 = W_p + F_A^p - I_F \dot{T}_p \begin{Bmatrix} \dot{x} \\ \dot{y} \\ \dot{z} \end{Bmatrix} - S_\omega^p I_F \begin{Bmatrix} u_A \\ v_A \\ w_A \end{Bmatrix} - m_p S_w^p S_w^p \begin{Bmatrix} x_{cp} \\ y_{cp} \\ z_{cp} \end{Bmatrix} \tag{11}$$

$$\mathrm{B}_3 = M_c - S_w^b I_b \begin{Bmatrix} p_b \\ q_b \\ r_b \end{Bmatrix} \tag{12}$$

$$\mathrm{B}_4 = M_A - T_p T_b^T M_c - S_w^p \left(I_p + I_M\right) \begin{Bmatrix} p_p \\ q_p \\ r_p \end{Bmatrix} - S_p^a I_F \dot{T}_p \begin{Bmatrix} \dot{x} \\ \dot{y} \\ \dot{z} \end{Bmatrix} - S_p^a S_\omega^p I_F \begin{Bmatrix} u_A \\ v_A \\ w_A \end{Bmatrix} \tag{13}$$

where,

$$S_w^b = \begin{bmatrix} 0 & -r_b & q_b \\ r_b & 0 & -p_b \\ -q_b & p_b & 0 \end{bmatrix} \tag{14}$$

$$S_w^p = \begin{bmatrix} 0 & -r_p & q_p \\ r_p & 0 & -p_p \\ -q_p & p_p & 0 \end{bmatrix} \tag{15}$$

The weight force vectors on both the parafoil and payload in their respective body axes are given in Equations 16 and 17.

$$W_b = m_b g \begin{Bmatrix} -s_{\theta_b} \\ s_{\phi_b} c_{\theta_b} \\ c_{\phi_b} c_{\theta_b} \end{Bmatrix} \tag{16}$$

$$W_p = m_P g \begin{Bmatrix} -s_{\theta_p} \\ s_{\phi_p} c_{\theta_p} \\ c_{\phi_p} c_{\theta_p} \end{Bmatrix} \tag{17}$$

Equation 18 gives aerodynamic force on the payload from drag, which acts at the center of pressure of the payload assumed to be located at the payload's center.

$$F_A^b = -\frac{1}{2}\rho A_b V_b C_D^b \begin{Bmatrix} u_b \\ v_b \\ w_b \end{Bmatrix} \tag{18}$$

The payload frame components of the payload's mass center velocity that appear in Equation 18 are computed using Equation 19.

$$\begin{Bmatrix} u_b \\ v_b \\ w_b \end{Bmatrix} = T_b \begin{Bmatrix} \dot{x} \\ \dot{y} \\ \dot{z} \end{Bmatrix} + S_w^b \begin{Bmatrix} \rho_x^b \\ \rho_y^b \\ \rho_z^b \end{Bmatrix} \tag{19}$$

The shape of the parafoil canopy is modeled by joining panels of the same cross section side by side at angles with respect to a horizontal plane. The i^{th} panel of the parafoil canopy experiences lift and drag forces that are modeled using Equations 20 and 21, where u_i, v_i, w_i are the velocity components of the center of pressure of the i^{th} canopy panel in the i^{th} canopy panel frame [11].

$$L_i = \tfrac{1}{2}\rho A_i \sqrt{u_i^2 + w_i^2}\, C_{Li} \begin{Bmatrix} w_i \\ 0 \\ -u_i \end{Bmatrix} \tag{20}$$

$$D_i = -\tfrac{1}{2}\rho A_i V_i C_{Di}^p \begin{Bmatrix} u_i \\ v_i \\ w_i \end{Bmatrix} \tag{21}$$

Equation 22 provides the total aerodynamic force on the parafoil canopy.

$$F_A = \sum_{i=1}^{n} T_i (L_i + D_i) \tag{22}$$

The opening of the parafoil is modeled as the area increasing non-linearly over time similar to the approach taken by Wolfe and Peterson [12]. When the parafoil is

released from its pack each panel area A_i of the parafoil is small and increases over time until reaching the final panel area. The increase in panel area is modeled as a known nonlinear function. Computationally the panel area is obtained at an arbitrary time by linear interpolation of a table of data. This approach is not meant to completely model the complicated process of parafoil inflation but rather provide a realistic initial disturbance.

The applied moment about the parafoil's mass center contains contributions from the steady aerodynamic forces and the coupling joint's resistance to twisting. The moment due to a panel's steady aerodynamic forces is computed with a cross product between the distance vector from the mass center of the parafoil to the center of pressure of the panel and the force itself. Equation 23 gives the total moment from the steady aerodynamic forces.

$$M_A = \sum_{i=1}^{n} S_p^{CP_i} T_i \left(L_i + D_i \right) \tag{23}$$

where,

$$T_i = \begin{bmatrix} 1 & 0 & 0 \\ 0 & c_{\alpha_i} & -s_{\alpha_i} \\ 0 & s_{\alpha_i} & c_{\alpha_i} \end{bmatrix} \tag{24}$$

The resistance to twisting of the coupling joint is modeled as a rotational spring and damper given by Equation 25.

$$M_c = \begin{Bmatrix} 0 \\ 0 \\ K_c \left(\tilde{\psi}_p - \tilde{\psi}_b \right) + C_c \left(\dot{\tilde{\psi}}_p - \dot{\tilde{\psi}}_b \right) \end{Bmatrix} \tag{25}$$

The angles $\tilde{\psi}_p$ and $\tilde{\psi}_b$ are the modified Euler yaw angles of the parafoil and payload that come from a modified sequence of rotations where the Euler yaw angle is the final rotation. The Euler yaw angles $\tilde{\psi}_p$ and $\tilde{\psi}_b$ for the modified sequence of rotations can be related to the original Euler angles by Equations 26 and 27.

$$\tilde{\psi}_p = \tan^{-1}\left(\frac{s_{\phi_p} s_{\theta_p} c_{\psi_p} - c_{\phi_p} s_{\psi_p}}{c_{\theta_p} c_{\psi_p}}\right) \tag{26}$$

$$\tilde{\psi}_b = \tan^{-1}\left(\frac{s_{\phi_b} s_{\theta_b} c_{\psi_b} - c_{\phi_b} s_{\psi_b}}{c_{\theta_b} c_{\psi_b}}\right) \tag{27}$$

From the same modified sequence of rotations $\dot{\tilde{\psi}}_p$ and $\dot{\tilde{\psi}}_b$ are given in Equations 28 and 29.

$$\dot{\tilde{\psi}}_p = -c_{\tilde{\psi}_p} t_{\tilde{\theta}_p} p_p + s_{\tilde{\psi}_p} t_{\tilde{\theta}_p} q_p + r_p \tag{28}$$

$$\dot{\tilde{\psi}}_b = -c_{\tilde{\psi}_b} t_{\tilde{\theta}_b} p_b + s_{\tilde{\psi}_b} t_{\tilde{\theta}_b} q_b + r_b \tag{29}$$

where,

$$t_{\tilde{\theta}_p} = \frac{c_{\phi_p} s_{\theta_p} c_{\psi_p} + s_{\phi_p} s_{\psi_p}}{c_{\theta_p} c_{\psi_p}} c_{\tilde{\psi}_p} \tag{30}$$

$$t_{\tilde{\theta}_b} = \frac{c_{\phi_b} s_{\theta_b} c_{\psi_b} + s_{\phi_b} s_{\psi_b}}{c_{\theta_b} c_{\psi_b}} c_{\tilde{\psi}_b} \tag{31}$$

Given the state vector of the system, the 12 linear equations in Equation 4 are solved to obtain derivatives of the state vector along with the coupling joint constraint force components required for numerical simulation.

RESULTS

The system of equations given in Equation 4 is solved using LU decomposition and the equations of motion described above are numerically integrated using a fourth order Runge-Kutta algorithm to generate the trajectory of the system from its point of release. Simulations under different conditions are performed so that the performance of the controllable parafoil and payload system can be evaluated. The payload is a

cube measuring 1.0 ft on a side and has a weight of 10 lbf with uniform density. The parafoil consists of five panels as shown in Figure 1.2, each having dimensions of 1.25 ft x 2.5 ft and having a combined weight of 0.5 lbf. The mass center of each panel from its base is 1.3 ft. The parafoil panel area remains small from the release of the parafoil until 0.6 sec when the panel areas increase until 2.9 sec when the final areas are reached. The length of the rigid links from the coupling joint to the payload mass center and the coupling joint to the parafoil mass center are $\vec{r}_{c\to b} = 3.0\vec{K}_b \;\; ft$ and $\vec{r}_{c\to p} = -0.5\vec{I}_p - 4.0\vec{K}_p \;\; ft$ respectively. The rotational stiffness and damping at joint C were chosen to be 0.35 $lb \cdot ft/rad$ and 0.025 $lb \cdot ft/rad^2$ which were sufficient to maintain the parafoil and payload within 10 deg of yaw angle. The panel aerodynamic coefficients used in the simulations are shown in Figure 1.4.

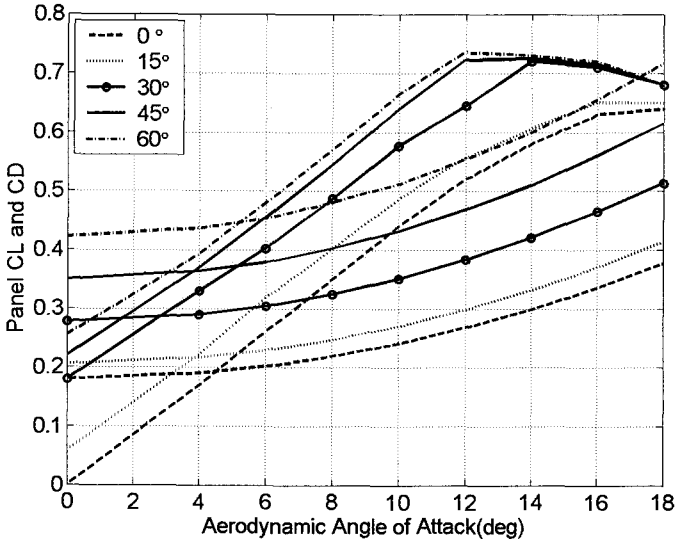

Figure 1.4 Lift and Drag Coefficients for Varying Brake Deflections

The generated coefficients are representative of the general parafoil simulated and have the same trends as data collected for parafoils over a broad range of dimensions [8], [10], [13]. The six apparent mass coefficients are based of the following formulas of Lissaman and Brown [14] where, t, c and b are the thickness,

chord and span of the parafoil. The appropriate air density must multiply the coefficients in Equations 32 through 37.

$$A = k_A \pi \frac{t^2 b}{4} \tag{32}$$

$$B = k_B \pi \frac{t^2 c}{4} \tag{33}$$

$$C = k_C \pi \frac{c^2 b}{4} \tag{34}$$

$$I_A = k_A^* \pi \frac{c^2 b^3}{48} \tag{35}$$

$$I_B = k_B^* \frac{4c^4 b}{48\pi} \tag{36}$$

$$I_C = k_C^* \pi \frac{t^2 b^3}{48} \tag{37}$$

The apparent mass coefficients in Equations 32-37 have three-dimensional correction factors that are also given by Lissaman and Brown that depend on the aspect ratio A^*, and the arc-to-span ratio a^*. Equations 32 through 37 and the three-dimensional correction factors are evaluated for the properties listed in Table 1 and listed in Table 2.

Table 1.1 Parafoil Dimensions

t	0.33 ft
c	2.5 ft
b	6.0 ft
a^*	0.17
A^*	2.4

Table 1.2 Apparent Mass and Correction Coefficients

Correction Coefficients		Apparent Mass Coefficients	
k_A	0.913	A	0.0001
k_B	0.339	B	0.0002
k_C	0.771	C	0.0466
k_A^*	0.630	I_A	0.1141
k_B^*	0.872	I_B	0.0111
k_C^*	1.044	I_C	0.0033

For the baseline simulation the parafoil and payload system is released from an altitude of 5000 ft with a level speed of 50 ft/s. The panel angles α_1, α_3 as shown in Figure 1.2 are 35 deg and 15 deg respectively, α_5 is 0 deg and the angle of incidence is –8.5 deg. Baseline simulation results are shown in Figures 5-10. Figure 1.5 plots pitch angle versus time of the payload and parafoil, which shows a large negative pitch of the parafoil and payload due to the large aerodynamic forces on the payload and the small aerodynamic forces on the parafoil before it fully opens. The opening of the parafoil at 0.6 sec begins an increase in aerodynamic forces on the parafoil and the pitch angles of both the payload and parafoil begin to increase before settling to –7.0 deg for the payload and –29.5 deg for the parafoil. The body pitch rates of the payload and parafoil shown in Figure 1.6 oscillate at a frequency of 2 Hz during the opening of the parafoil at 0.6 sec and decay to near 0 by 12.0 sec. The vertical velocity, forward velocity, aerodynamic angle of attack, and constraint forces shown in Figures 7 through 9 also show similar oscillatory characteristics during the opening of the parafoil and reach steady states by 12.0 sec.

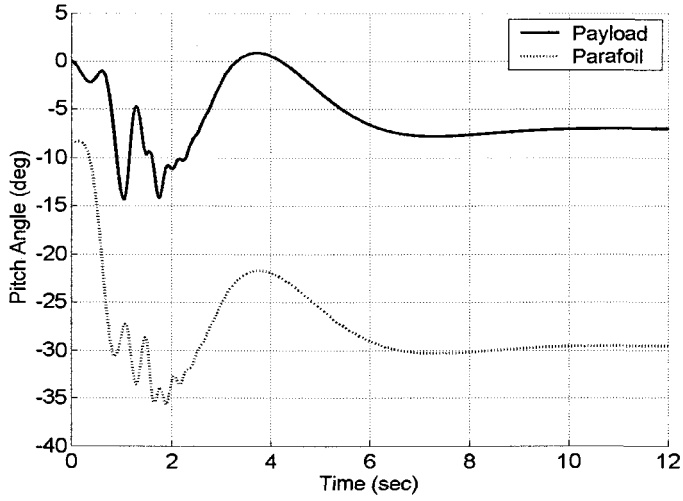

Figure 1.5 Pitch Angle vs. Time

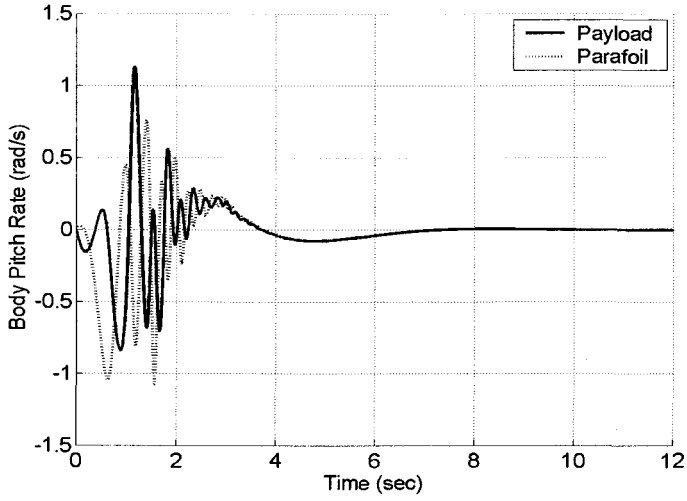

Figure 1.6 Body Pitch Rate vs. Time

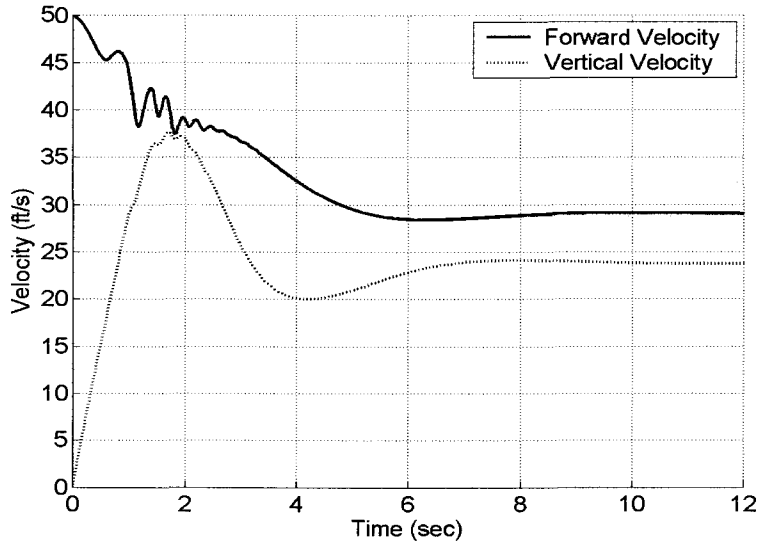

Figure 1.7 Velocity vs. Time

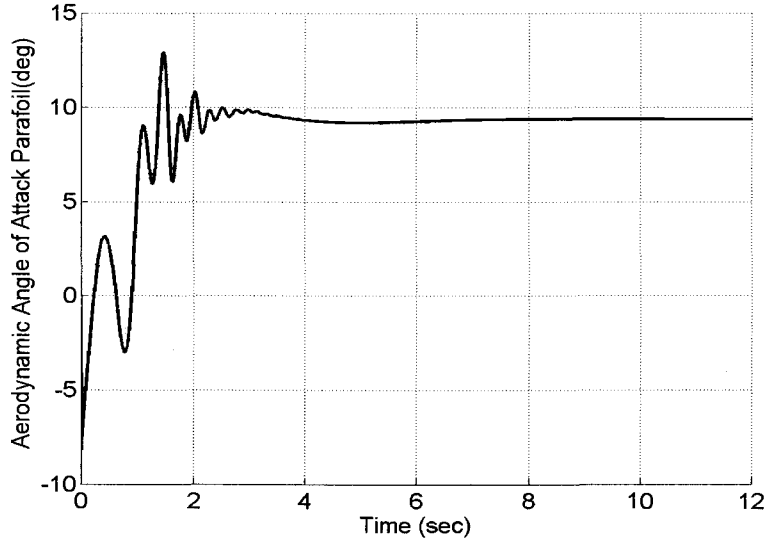

Figure 1.8 Aerodynamic Angle of Attack vs. Time

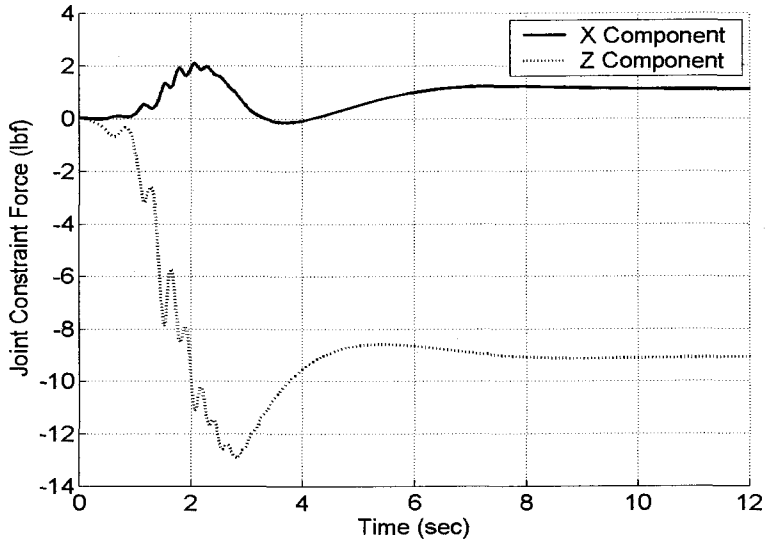

Figure 1.9 Constraint Forces vs. Time

The altitude of the payload mass center versus time shown in Figure 1.10 begins to decrease rapidly during the opening of the parafoil but reaches a steady glide rate after the pitch angle of the payload and parafoil have reached their steady state values.

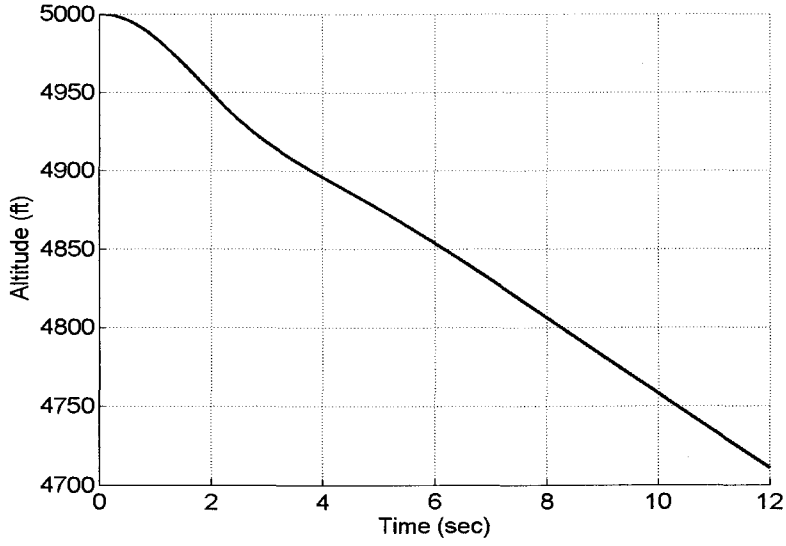

Figure 1.10 Altitude vs. Time

For a controllable parafoil a subject of interest is the control authority of both large and small brake deflections. The control response to a brake deflection is dependent on the orientation of the panel angles. A set of 9 different cases of panel orientation is used in the following trade studies and is defined in Table 3. Figure 1.11 shows the response of the baseline parafoil with a –3.0 deg angle of incidence and a constant small right side brake of 10 deg applied after a 10 second settling period. Cases C, D and E have negative turn rates for the small right side brake while cases F and G have positive turn rates. The control authority of small braking reverses as the orientation of the panel angles become more curved. The baseline parafoil with a –3.0 deg angle of incidence demonstrates two modes of control. The mode of control for the less curved cases A through E is roll steering. The flatter parafoil uses increased lift that dominates drag from the 10 deg brake to roll the parafoil and subsequently yaw. The mode of control for the more curved cases F through I is skid steering. Increased drag dominates lift and increased drag on the right side of the parafoil generates yawing of the parafoil. Figure 1.12 shows the turn rates versus time for the five parafoil cases shown in Figure 1.11. The negative sign on the turn rate signifies the turn is counterclockwise if looking down on the parafoil. It can be seen that the turn rates settle to a near constant value by 22 seconds for all five panel cases. A critical panel orientation occurs between cases E and F where the parafoil switches from roll steering to skid steering and a small brake would fail to generate yawing. Turn rates are shown in Figure 1.13 versus panel case for three angles of incidence: –3.0 deg, -7.0 deg and –13.0 deg. The critical panel orientation changes as the angle of incidence is decreased. The critical panel orientation for a –3.0 deg angle of incidence is between cases E and F, for –7.0 deg the critical angle is between F and G and for –13.0 deg the critical angle is between G and H. Reducing the angle of incidence or reducing the curvature of the parafoil canopy moves the mode of steering towards roll steer and decreases the control authority of a nominally skid steering parafoil, and increases the control authority of a nominally roll steer parafoil. Iacomini and Cerimele observed this trend in NASA's X-38, which is a skid steering parafoil,

noting that making the angle of incidence more severe "decreased turn rates for a given turn setting."[9]

Table 1.3 Panel Angles

CASE	Panel Angle (deg)				
	Panel 1	Panel 2	Panel 3	Panel 4	Panel 5
A	15	-15	10	-10	0
B	19	-19	11	-11	0
C	23	-23	12	-12	0
D	27	-27	13	-13	0
E	31	-31	14	-14	0
F	35	-35	15	-15	0
G	39	-39	16	-16	0
H	43	-43	17	-17	0
I	47	-47	18	-18	0

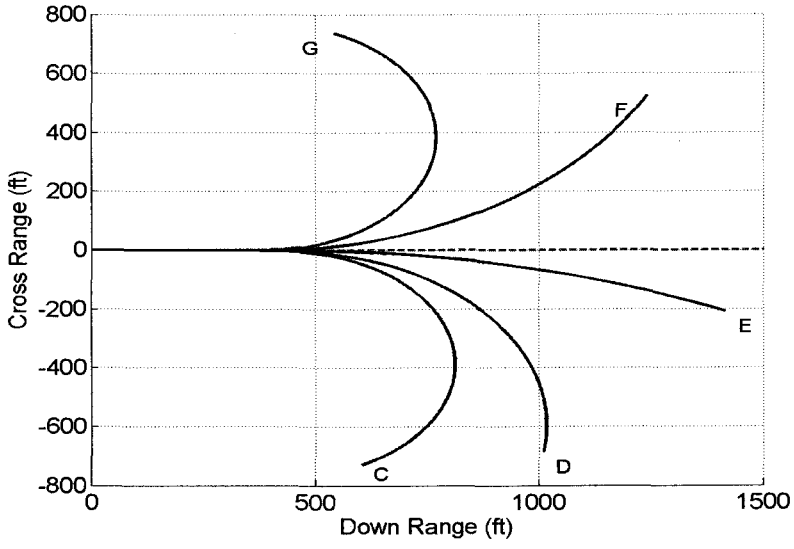

Figure 1.11 Cross Range vs. Time (Angle of incidence = -3.0°, 10° Right Brake)

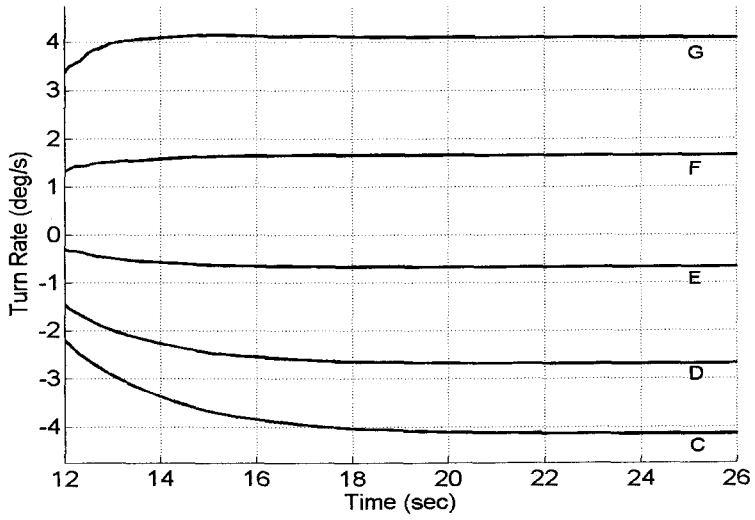

Figure 1.12 Turn Rate vs. Time (Angle of incidence = -3.0°, 10° Right Brake)

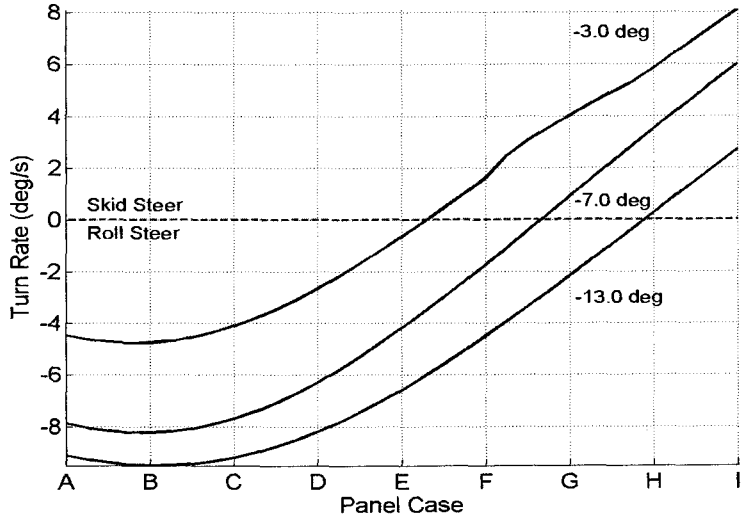

Figure 1.13 Turn Rate vs. Panel Case (10° Right Brake)

In order to investigate the sensitivity of the control response due to the lift to drag ratio of the parafoil, the drag curves shown in Figure 1.4 were held constant while the lift curves were varied +/- 15 percent. The control response is dependent on the lift to drag ratio of the panels and the turn rates are shown in Figure 1.14 versus steady state lift to drag ratio for three angles of incidence: –3.0 deg, -7.0 deg and –13.0

deg. Similar to varying panel curvature, a critical lift to drag ratio occurs where the parafoil switches from roll steering to skid steering and a small break fails to generate yawing. The critical lift to drag ratio changes as the angle of incidence is decreased. The critical lift to drag ratio for a –3.0 deg angle of incidence is 2.04 deg, for–7.0 deg and –13.0 deg no critical lift to drag ratio is reached and a skid steering mode does not occur.

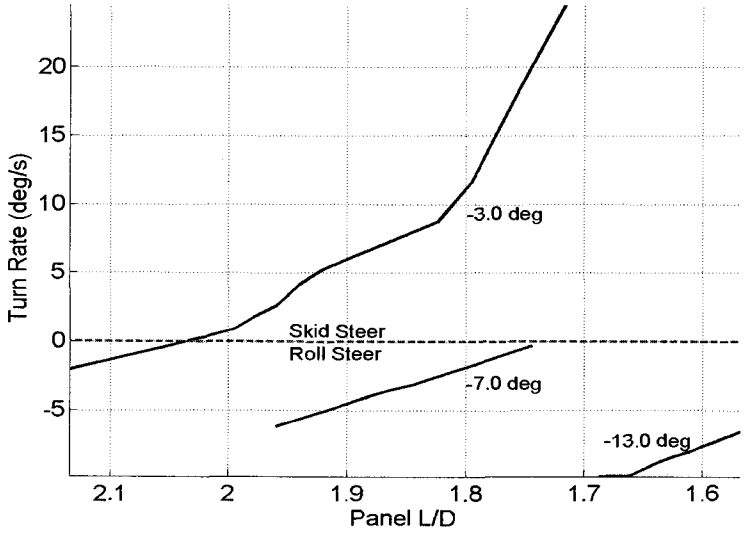

Figure 1.14 Turn Rate vs. Lift to Drag Ratio (10^{o} Right Brake)

The control authority of the parafoil also depends on the magnitude of the control input. The turn rate is shown versus control input in Figure 1.15 for panel case F and an angle of incidence of –7.0 deg. As shown in Figure 1.13 this corresponds to a roll steer mode at small brake deflections. It can be seen in Figure 1.15 that the roll steering mode increases its control authority until a brake deflection of 15 deg is reached. After 15 deg the steering transitions toward a skid steering mode as brake deflection is increased until the parafoil reaches skid steering at 17.5 deg. The roll steering mode transitions to skid steering as the brake deflection increases and drag begins to dominate. Iacomini and Cerimele have observed, (while attributed to brake reflex) the phenomenon of a control reversal for small brake deflections in NASA's X-38 program.[10] In fact, parafoils mostly operate in a skid steering mode when the brake

deflections are large. It should be clear from the trends in Figures 1.13 and 1.15 that a parafoil can be designed to never roll steer even for the smallest brake deflections. A parafoil that skid steers for all the brake deflections, curvatures and angles of incidence however maintains the observed trends namely that skid steering control authority is increased as brake deflection is increased, panel curvature is increased and the angle of incidence becomes less negative. More importantly a parafoil that demonstrates roll steering only for small brake deflections such as the parafoil in Figure 1.15 can be modified to eliminate all roll steering tendencies by changing the curvature or angle of incidence.

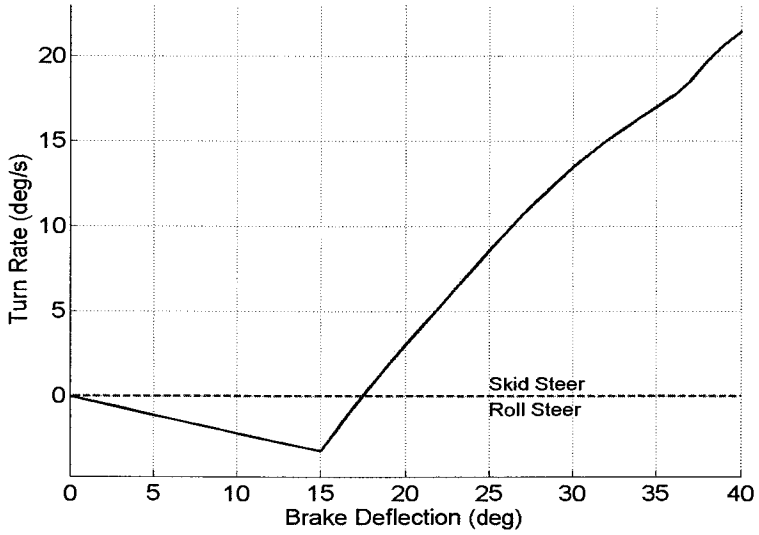

Figure 1.15 Turn Rate vs. Brake Deflection

CONCLUSIONS

Using a 9 DOF flight dynamic model, it has been shown that parafoil and payload systems exhibit two basic modes of directional control, skid steering and roll steering for small brake deflections. For a particular configuration the mode of

directional control depends on the angle of incidence and the panel orientation. The parafoil's mode of directional control is skid steering for canopies of "high" curvature and "smaller" negative angles of incidence. The mode of directional control transitions towards roll steering as the canopy curvature decreases or the angle of incidence becomes more negative. The mode of directional control also transitions away from the roll steering mode as the magnitude of the brake deflection increases and for "large" brake deflections most parafoils will always skid steer. Control reversal is usually undesirable and since parafoils have a tendency to skid steer for large brake deflections, care needs to be taken to know and avoid the range of small braking that may induce roll steering. With careful design a parafoil and payload system can be properly modified so that roll steering can be eliminated all together.

REFERENCES

[1] Wolf, D., "Dynamic Stability of Nonrigid Parachute and Payload System," *Journal of Aircraft*, Vol. 8 No. 8, pp. 603-609, 1971.

[2] Doherr, K., Schiling, H., "9 DOF-simulation of Rotating Parachute Systems," AIAA 12th. Aerodynamic Decelerator and Balloon Tech. Conf, 1991.

[3] Hailiang, M., Zizeng, Q., "9-DOF Simulation of Controllable Parafoil System for Gliding and Stability," *Journal of National University of Defense Technology*, Vol. 16 No. 2, pp. 49-54, 1994.

[4] Iosilevskii, G., "Center of Gravity and Minimal Lift Coefficient Limits of a Gliding Parachute," *Journal of Aircraft*, Vol. 32 No. 6, pp. 1297-1302, 1995.

[5] Brown, G.J, "Parafoil Steady Turn Response to Control Input," AIAA Paper 93-1241.

[6] Zhu, Y., Moreau, M., Accorsi, M., Leonard J.,Smith J., "Computer Simulation of Parafoil Dynamics," AIAA 2001-2005, AIAA 16th Aerodynamic Decelerator Systems Technology Conference, May 2001.

[7] Gupta, M., Xu, Z., Zhang, W., Accorsi, M., Leonard, J., Benney R., Stein., "Recent Advances in Structural Modeling of Parachute Dynamics," AIAA 2001-2030, AIAA 16th Aerodynamic Decelerator Systems Technology Conference, May 2001.

[8] Ware, G.M., Hassell, Jr., J.L., "Wind-Tunnel Investigation of Ram-Air_Inflated All-Flexible Wings of Aspect Ratios 1.0 to 3.0," NASA TM SX-1923,1969.

[9] Iacomini, C.S., Cerimele, C.J., "Lateral-Directional Aerodynamics from a Large Scale Parafoil Test Program," AIAA Paper 99-1731.

[10] Iacomini, C.S., Cerimele, C.J., "Longitudinal Aerodynamics from a Large Scale Parafoil Test Program," AIAA Paper 99-1732.

[11] McCormick, B., "Aerodynamics and Aeronautics and Fight Mechanics", John Wiley and Sons Inc, New York, NY, 1979.

[12] Wolfe, W.P., Peterson, C.W., "Modeling of Parachute Line Wrap," AIAA 2001-2030, AIAA 16th Aerodynamic Decelerator Systems Technology Conference, May 2001.

[13] Ellison, R.K., "Determination of a parafoil Submunition Payload and Aerodynamic Control," AFATL-TR-85-74.

[14] Lissaman, P.B.S., Brown, G. J., "Apparent Mass Effects on Parafoil Dynamics," AIAA Paper 93-1236.

COMPARISON OF MEASURED AND SIMULATED MOTION OF A CONTROLLABLE PARAFOIL AND PAYLOAD SYSTEM

Nathan Slegers and Mark Costello

AIAA Atmospheric Flight Mechanics Conference and Exhibit
AIAA Paper 2003-5611, Austin, Texas

COMPARISON OF MEASURED AND SIMULATED MOTION OF A CONTROLLABLE PARAFOIL AND PAYLOAD SYSTEM

Nathan Slegers* Mark Costello†
Department of Mechanical Engineering
Oregon State University
Corvallis, Oregon 97331

ABSTRACT

For parafoil and payload aircraft, control is affected by changing the length of several rigging lines connected to the outboard side and rear of the parafoil leading to complex changes in the shape and orientation of the lifting surface. Flight mechanics of parafoil and payload aircraft most often employ a 6 or 9 degree-of-freedom (DOF) representation with the canopy modeled as a rigid body during flight. The effect of control inputs is idealized by the deflection of parafoil brakes on the left and right side of the parafoil. Using a small parafoil and payload aircraft, glide rates and turn performance were measured and compared against a 9 DOF simulation model. This work shows that to properly capture control response of parafoil and payload aircraft, tilt of the parafoil canopy must be accounted for along with left and right parafoil brake deflection.

* Graduate Research Assistant, Department of Mechanical Engineering, Member AIAA.
† Associate Professor, Department of Mechanical Engineering, Member AIAA.

NOMENCLATURE

x, y, z : Components of position vector of point C in an inertial frame.

ϕ_b, θ_b, ψ_b : Euler roll, pitch and yaw angles of payload.

ϕ_p, θ_p, ψ_p : Euler roll, pitch and yaw angles of parafoil.

$\tilde{\phi}_b, \tilde{\theta}_b, \tilde{\psi}_b$: Payload Euler roll, pitch and yaw angles for roll constraint moment computation.

$\tilde{\phi}_p, \tilde{\theta}_p, \tilde{\psi}_p$: Parafoil Euler roll, pitch and yaw angles for roll constraint moment computation.

$\dot{x}, \dot{y}, \dot{z}$: Components of velocity vector of point C in an inertial frame.

p_b, q_b, r_b : Components of angular velocity of payload in payload reference frame (b).

p_p, q_p, r_p : Components of angular velocity of parafoil in parafoil reference frame (p).

m_b, m_p : Mass of payload and parafoil.

F_{xc}, F_{yc}, F_{zc} : Components of joint constraint force in an inertial frame.

M_{xc}, M_{yc}, M_{zc} : Components of joint constraint moment in an inertial frame.

u_i, v_i, w_i : Components of relative air velocity of aerodynamic center of panel i in i^{th} frame.

V_s : Magnitude of velocity vector of mass center of payload.

u_b, v_b, w_b : Components of relative air velocity of mass center of payload in payload reference frame.

u_A, v_A, w_A : Components of relative air velocity of apparent mass center in parafoil reference frame.

x_{cb}, y_{cb}, z_{cb} : Components of vector from point C to mass center of payload in payload reference frame.

x_{cp}, y_{cp}, z_{cp} : Components of vector from point C to mass center of parafoil in parafoil reference frame.

x_{ca}, y_{ca}, z_{ca}: Components of vector from point C to apparent mass center in parafoil reference frame.

x_{pa}, y_{pa}, z_{pa}: Components of vector from parafoil mass center to apparent mass center in parafoil reference frame.

I_b, I_p: Inertia matrix of payload and parafoil.

I_F, I_M: Apparent mass force and moment coefficient matrices.

C_D^b: Drag coefficient of payload.

C_{Li}: Lift coefficient of i^{th} panel of parafoil canopy.

C_{Di}^p: Drag coefficient of i^{th} panel of parafoil canopy.

η: Angle of incidence

K_c, C_c: Rotational stiffness and damping coefficients of joint C.

A_b: Payload reference area.

A_i: Reference area of i^{th} panel of parafoil canopy.

T_p: Transformation matrix from inertial reference frame to parafoil reference frame.

T_b: Transformation matrix from inertial reference frame to payload reference frame.

T_i: Transformation matrix from i^{th} panel's reference frame to parafoil reference frame.

T_{ti}: Transformation matrix from inertial reference frame to i^{th} command trajectory reference frame.

F_A^b, F_A^p: Aerodynamic force on payload and parafoil in their respective frames.

M_A: Moment on parafoil due to steady aerodynamic forces.

M_{UA}: Moment on payload due to unsteady aerodynamic forces.

INTRODUCTION

New concepts for gathering real-time battlefield information rely on autonomous parafoil and payload aircraft. Relative to other air vehicles, parafoil and payload aircraft enjoy the advantage of low speed flight, long endurance, and low ground impact velocity. Control is affected by changing the length of several of the parafoil rigging lines connected to the outboard side and rear of the parafoil lifting surface. To efficiently tailor this type of aircraft to a particular design environment, dynamic modeling and simulation is applied to an idealized representation of this complex system. Flight mechanics of parafoil and payload aircraft are typically modeled using a 6 or 9 degree-of-freedom (DOF) representation. In both cases, the parafoil canopy is considered a rigid body once it is inflated. There are two methods used to represent control. Perhaps the simplest method to model control forces and moments is through the use of control derivatives with the coefficients identified from flight data. The advantage of this method lies in the simplicity of the approach. The disadvantage is that little insight is provided into design parameters that affect the control response. Another method to model the control force and moment caused by the action of changes in rigging line length on each side of the parafoil is a plain flap or parafoil brake that can be deflected downward only. While more complicated, the advantage of this method lies in the close connection to design parameters of the parafoil.

Wolf and later Doherr and Schilling reported on the development of dynamic models for parachute and payload aircraft [1], [2]. Hailiang and Zizeng [3] used a 9-degree of freedom model to study the motion of a parafoil and payload system. Iosilevskii [4] established center of gravity and lift coefficient limits for a gliding parachute. Brown [5] analyzed the effects of scale and wing loading on a parafoil using a linearized model based on computer calculated aerodynamic coefficients. More recent efforts by Zhu, Moreau, Accorsi, Leonard, and Smith [6] as well as Gupta, Xu, Zhang, Accorsi, Leonard, Benney, and Stein [7] have incorporated parafoil

structural dynamics into the dynamic model of a parachute and payload system. A significant amount of literature has been amassed in the area of experimental parafoil dynamics beginning with Ware and Hassell [8] who investigated ram-air parachutes in a wind tunnel by varying wing area and wing chord. More recently extensive flight tests have been reported on NASA's X-38 parafoil providing steady-state data and aerodynamics for large-scale parafoils [9], [10].

This paper focuses on proper modeling of the control response as a function of fundamental design parameters by modeling control response from both left and right brake deflection and canopy tilt. A comparison of flight test data and 9 DOF simulation results for a small parafoil and payload aircraft is presented.

PARAFOIL AND PAYLOAD AIRCRAFT MODEL

Figures 2.1 and 2.2 show schematics of parafoil canopy geometry. With the exception of movable parafoil brakes, the parafoil canopy is considered to be a fixed shape once it has completely inflated.

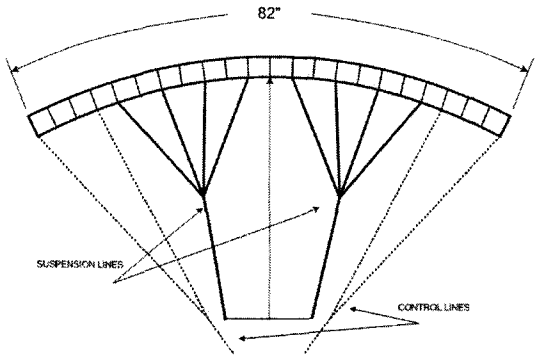

Figure 2.1 Front View of Parafoil Canopy

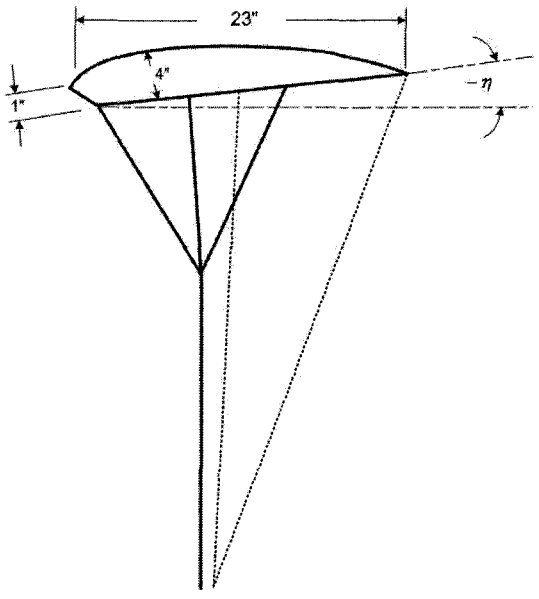

Figure 2.2 Side View of Parafoil Canopy

The canopy shape is modeled as a collection of panels oriented at fixed angle with respect to each other as shown in Figure 2.3. Deflection of the control arms on the payload causes deflection of two lines on the parafoil canopy. Connected to the outboard end and side panels are brakes that locally deflect the canopy downward. Due to the fact that the parafoil canopy is a flexible membrane, deflection of the control arms on one side of the parafoil also creates tilt of the canopy.

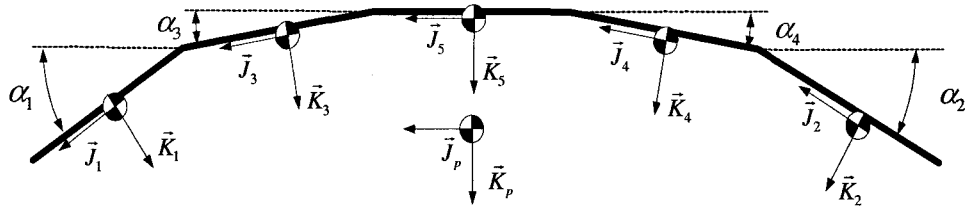

Figure 2.3 Parafoil Canopy Geometry

Both these effects combine together to form the overall turning response. The parafoil canopy is connected to joint C by a rigid massless link from the mass center of the canopy. The payload is connected to joint C by a rigid massless link from the mass

center of the payload. Both the parafoil and the payload are free to rotate about joint C but are constrained by the force and moment at the joint. The combined system of the parafoil canopy and the payload are modeled with 9 degrees-of-freedom, including three inertial position components of the joint C as well as the three Euler orientation angles of the parafoil canopy and the payload. The kinematic equations for the parafoil canopy and the payload are provided in Equations 1 through 3.

$$\begin{Bmatrix} \dot{x}_c \\ \dot{y}_c \\ \dot{z}_c \end{Bmatrix} = \begin{Bmatrix} u_c \\ v_c \\ w_c \end{Bmatrix} \tag{1}$$

$$\begin{Bmatrix} \dot{\phi}_b \\ \dot{\theta}_b \\ \dot{\psi}_b \end{Bmatrix} = \begin{bmatrix} 1 & s_{\phi_b} t_{\theta_b} & c_{\phi_b} t_{\theta_b} \\ 0 & c_{\phi_b} & -s_{\phi_b} \\ 0 & s_{\phi_b}/c_{\theta_b} & c_{\phi_b}/c_{\theta_b} \end{bmatrix} \begin{Bmatrix} p_b \\ q_b \\ r_b \end{Bmatrix} \tag{2}$$

$$\begin{Bmatrix} \dot{\phi}_p \\ \dot{\theta}_p \\ \dot{\psi}_p \end{Bmatrix} = \begin{bmatrix} 1 & s_{\phi_p} t_{\theta_p} & c_{\phi_p} t_{\theta_p} \\ 0 & c_{\phi_p} & -s_{\phi_p} \\ 0 & s_{\phi_p}/c_{\theta_p} & c_{\phi_p}/c_{\theta_p} \end{bmatrix} \begin{Bmatrix} p_p \\ q_p \\ r_p \end{Bmatrix} \tag{3}$$

The dynamic equations are formed by first separating the system at the coupling joint, exposing the joint constraint force and moment acting on both bodies. The translational and rotational dynamics are inertially coupled because the position degrees of freedom of the system are the inertial position vector components of the coupling joint. The constraint force is a quantity of interest to monitor during the simulation so it is retained in the dynamic equations rather than being algebraically eliminated. Equation 4 represents the translational and rotational dynamic equations of both the parafoil and payload concatenated into matrix form.

$$\begin{bmatrix} -m_b S_c^b & 0 & m_b T_b & -T_b \\ 0 & -I_F S_c^a - m_p S_c^p & I_F T_p + m_p T_p & T_p \\ I_b & 0 & 0 & S_c^b T_b \\ 0 & I_M + I_p - S_p^a I_F S_c^a & S_p^a I_F T_p & -S_c^p T_p \end{bmatrix} \begin{Bmatrix} \dot{p}_b \\ \dot{q}_b \\ \dot{r}_b \\ \cdots \\ \dot{p}_p \\ \dot{q}_p \\ \dot{r}_p \\ \cdots \\ \ddot{x}_c \\ \ddot{y}_c \\ \ddot{z}_c \\ \cdots \\ F_{xc} \\ F_{yc} \\ F_{zc} \end{Bmatrix} = \begin{Bmatrix} \mathrm{B}_1 \\ \mathrm{B}_2 \\ \mathrm{B}_3 \\ \mathrm{B}_4 \end{Bmatrix} \tag{4}$$

The matrix in Equation 4 is a block 4 x 4 matrix where each element is a 3 x 3 matrix. Rows 1-3 in Equation 4 are forces acting on the payload mass center expressed in the payload frame and rows 7-9 are the moments about the payload mass center also in the payload frame. Rows 4-6 in Equation 4 are forces acting on the parafoil mass center expressed in the parafoil frame and rows 10-12 are the moments about the parafoil mass center also in the parafoil frame. The S_i^j matrices are cross product operator matrices, working on different vectors from i to j associated with the system configuration.

$$S_i^j = \begin{bmatrix} 0 & -z_{ij} & y_{ij} \\ z_{ij} & 0 & -x_{ij} \\ -y_{ij} & x_{ij} & 0 \end{bmatrix} \tag{5}$$

The matrix T_b represents the transformation matrix from an inertial reference frame to the payload reference frame,

$$T_b = \begin{bmatrix} c_{\theta_b} c_{\psi_b} & c_{\theta_b} s_{\psi_b} & -s_{\theta_b} \\ s_{\phi_b} s_{\theta_b} c_{\psi_b} - c_{\phi_b} s_{\psi_b} & s_{\phi_b} s_{\theta_b} s_{\psi_b} + c_{\phi_b} c_{\psi_b} & c_{\theta_b} s_{\phi_b} \\ c_{\phi_b} s_{\theta_b} c_{\psi_b} + s_{\phi_b} s_{\psi_b} & c_{\phi_b} s_{\theta_b} s_{\psi_b} - s_{\phi_b} c_{\psi_b} & c_{\phi_b} c_{\theta_b} \end{bmatrix} \tag{6}$$

while, T_p represents the transformation matrix from an inertial reference frame to the parafoil reference frame.

$$T_p = \begin{bmatrix} c_{\theta_p} c_{\psi_p} & c_{\theta_p} s_{\psi_p} & -s_{\theta_p} \\ s_{\phi_p} s_{\theta_p} c_{\psi_p} - c_{\phi_p} s_{\psi_p} & s_{\phi_p} s_{\theta_p} s_{\psi_p} + c_{\phi_p} c_{\psi_p} & c_{\theta_p} s_{\phi_p} \\ c_{\phi_p} s_{\theta_p} c_{\psi_p} + s_{\phi_p} s_{\psi_p} & c_{\phi_p} s_{\theta_p} s_{\psi_p} - s_{\phi_p} c_{\psi_p} & c_{\phi_p} c_{\theta_p} \end{bmatrix} \tag{7}$$

The common shorthand notation for trigonometric functions is employed where $\sin(\alpha) \equiv s_\alpha$, $\cos(\alpha) \equiv s_\alpha$ and $\tan(\alpha) \equiv t_\alpha$. The matrices I_b and I_p represent the mass moment of inertia matrices of the payload and the parafoil body with respect to their respective mass centers and the matrices I_F and I_M represent the apparent mass force coefficient matrix and apparent mass moment coefficient matrix respectively.

$$I_F = \begin{bmatrix} A & 0 & 0 \\ 0 & B & 0 \\ 0 & 0 & C \end{bmatrix} \tag{8}$$

$$I_M = \begin{bmatrix} I_A & 0 & 0 \\ 0 & I_B & 0 \\ 0 & 0 & I_C \end{bmatrix} \tag{9}$$

Equations 10 through 13 provide the right hand side vector of Equation 4.

$$\mathrm{B}_1 = W_b + F_A^b - m_b S_w^b S_w^b \begin{Bmatrix} x_{cb} \\ y_{cb} \\ z_{cb} \end{Bmatrix} \tag{10}$$

$$\mathrm{B}_2 = W_p + F_A^p - I_F \dot{T}_p \begin{Bmatrix} \dot{x} \\ \dot{y} \\ \dot{z} \end{Bmatrix} - S_\omega^p I_F \begin{Bmatrix} u_A \\ v_A \\ w_A \end{Bmatrix} - m_p S_w^p S_w^p \begin{Bmatrix} x_{cp} \\ y_{cp} \\ z_{cp} \end{Bmatrix} \tag{11}$$

$$\mathrm{B}_3 = M_c - S_w^b I_b \begin{Bmatrix} p_b \\ q_b \\ r_b \end{Bmatrix} \tag{12}$$

$$\mathrm{B}_4 = M_A - T_p T_b^T M_c - S_w^p (I_p + I_M) \begin{Bmatrix} p_p \\ q_p \\ r_p \end{Bmatrix} - S_p^a I_F \dot{T}_p \begin{Bmatrix} \dot{x} \\ \dot{y} \\ \dot{z} \end{Bmatrix} - S_p^a S_\omega^p I_F \begin{Bmatrix} u_A \\ v_A \\ w_A \end{Bmatrix} \tag{13}$$

where,

$$S_w^b = \begin{bmatrix} 0 & -r_b & q_b \\ r_b & 0 & -p_b \\ -q_b & p_b & 0 \end{bmatrix} \tag{14}$$

$$S_w^p = \begin{bmatrix} 0 & -r_p & q_p \\ r_p & 0 & -p_p \\ -q_p & p_p & 0 \end{bmatrix} \tag{15}$$

The weight force vectors on both the parafoil and payload in their respective body axes are given in Equations 16 and 17.

$$W_b = m_b g \begin{Bmatrix} -s_{\theta_b} \\ s_{\phi_b} c_{\theta_b} \\ c_{\phi_b} c_{\theta_b} \end{Bmatrix} \tag{16}$$

$$W_p = m_P g \begin{Bmatrix} -s_{\theta_p} \\ s_{\phi_p} c_{\theta_p} \\ c_{\phi_p} c_{\theta_p} \end{Bmatrix} \tag{17}$$

Equation 18 gives aerodynamic force on the payload from drag, which acts at the center of pressure of the payload assumed to be located at the payload's center.

$$F_A^b = -\frac{1}{2} \rho A_b V_b C_D^b \begin{Bmatrix} u_b \\ v_b \\ w_b \end{Bmatrix} \tag{18}$$

The payload frame components of the payload's mass center velocity that appear in Equation 18 are computed using Equation 19.

$$\begin{Bmatrix} u_b \\ v_b \\ w_b \end{Bmatrix} = T_b \begin{Bmatrix} \dot{x} \\ \dot{y} \\ \dot{z} \end{Bmatrix} + S_w^b \begin{Bmatrix} \rho_x^b \\ \rho_y^b \\ \rho_z^b \end{Bmatrix} \tag{19}$$

The shape of the parafoil canopy is modeled by joining panels of the same cross section side by side at angles with respect to a horizontal plane. The i^{th} panel of the parafoil canopy experiences lift and drag forces that are modeled using Equations

20 and 21, where u_i, v_i, w_i are the velocity components of the center of pressure of the i^{th} canopy panel in the i^{th} canopy panel frame [11].

$$L_i = \tfrac{1}{2}\rho A_i \sqrt{u_i^2 + w_i^2}\, C_{Li} \begin{Bmatrix} w_i \\ 0 \\ -u_i \end{Bmatrix} \tag{20}$$

$$D_i = -\tfrac{1}{2}\rho A_i V_i C_{Di}^{p} \begin{Bmatrix} u_i \\ v_i \\ w_i \end{Bmatrix} \tag{21}$$

Equation 22 provides the total aerodynamic force on the parafoil canopy.

$$F_A = \sum_{i=1}^{n} T_i \left(L_i + D_i\right) \tag{22}$$

The applied moment about the parafoil's mass center contains contributions from the steady aerodynamic forces and the coupling joint's resistance to twisting. The moment due to a panel's steady aerodynamic forces is computed with a cross product between the distance vector from the mass center of the parafoil to the center of pressure of the panel and the force itself. Equation 23 gives the total moment from the steady aerodynamic forces.

$$M_A = \sum_{i=1}^{n} S_p^{CP_i} T_i \left(L_i + D_i\right) \tag{23}$$

where,

$$T_i = \begin{bmatrix} 1 & 0 & 0 \\ 0 & c_{\alpha_i} & -s_{\alpha_i} \\ 0 & s_{\alpha_i} & c_{\alpha_i} \end{bmatrix} \tag{24}$$

The resistance to twisting of the coupling joint is modeled as a rotational spring and damper given by Equation 25.

$$M_c = \begin{Bmatrix} 0 \\ 0 \\ K_c\left(\tilde{\psi}_p - \tilde{\psi}_b\right) + C_c\left(\dot{\tilde{\psi}}_p - \dot{\tilde{\psi}}_b\right) \end{Bmatrix} \tag{25}$$

The angles $\tilde{\psi}_p$ and $\tilde{\psi}_b$ are the modified Euler yaw angles of the parafoil and payload that come from a modified sequence of rotations where the Euler yaw angle is the final rotation. The Euler yaw angles $\tilde{\psi}_p$ and $\tilde{\psi}_b$ for the modified sequence of rotations can be related to the original Euler angles by Equations 26 and 27.

$$\tilde{\psi}_p = \tan^{-1}\left(\frac{s_{\phi_p} s_{\theta_p} c_{\psi_p} - c_{\phi_p} s_{\psi_p}}{c_{\theta_p} c_{\psi_p}}\right) \tag{26}$$

$$\tilde{\psi}_b = \tan^{-1}\left(\frac{s_{\phi_b} s_{\theta_b} c_{\psi_b} - c_{\phi_b} s_{\psi_b}}{c_{\theta_b} c_{\psi_b}}\right) \tag{27}$$

From the same modified sequence of rotations $\dot{\tilde{\psi}}_p$ and $\dot{\tilde{\psi}}_b$ are given in Equations 28 and 29.

$$\dot{\tilde{\psi}}_p = -c_{\tilde{\psi}_p} t_{\tilde{\theta}_p} p_p + s_{\tilde{\psi}_p} t_{\tilde{\theta}_p} q_p + r_p \tag{28}$$

$$\dot{\tilde{\psi}}_b = -c_{\tilde{\psi}_b} t_{\tilde{\theta}_b} p_b + s_{\tilde{\psi}_b} t_{\tilde{\theta}_b} q_b + r_b \tag{29}$$

where,

$$t_{\tilde{\theta}_p} = \frac{c_{\phi_p} s_{\theta_p} c_{\psi_p} + s_{\phi_p} s_{\psi_p}}{c_{\theta_p} c_{\psi_p}} c_{\tilde{\psi}_p} \tag{30}$$

$$t_{\tilde{\theta}_b} = \frac{c_{\phi_b} s_{\theta_b} c_{\psi_b} + s_{\phi_b} s_{\psi_b}}{c_{\theta_b} c_{\psi_b}} c_{\tilde{\psi}_b} \tag{31}$$

Given the state vector of the system, the 12 linear equations in Equation 4 are solved using LU decomposition and the equations of motion described above are numerically integrated using a fourth order Runge-Kutta algorithm to generate the trajectory of the system from it's point of release.

FLIGHT TEST AIRCRAFT DESCRIPTION

The parafoil canopy consists of 22 cells that are formed by airfoil-shaped fabric ribs, has a surface area of 13.1 ft^2 and an aspect ratio of 3.6. The canopy is connected to the payload through two sets of suspension lines with each set consisting of four spanwise rows and three chordwise columns. Each grid of suspension lines is collected into a single suspension line that is then connected to the payload. Four control lines, two on each side, control the parafoil. The control lines on each side originate from half the chord length on the outboard edge of the canopy and 16" form the outboard edge on the rear of the canopy and are collected into a single control line for the side as shown in Figures 2.1 and 2.2.

The payload consists of an aluminum frame, three control servos, a 0.40 series glow engine and 10 x 6 pusher propeller, and an electronic control unit (ECU). Control of the system is accomplished through three servos, one for the engine throttle and two for the canopy control lines. The engine and propeller allow flight testing to be repeated easily and inexpensively by enabling the parafoil and payload aircraft to be launched from ground level and flown to appropriate altitudes where the engine is stopped and non-powered flight is commenced. The payload is shown in Figure 2.4 and the complete system is shown during flight in Figure 2.5. The ECU completes three tasks, recording control inputs, receiving Global Positioning Satellite (GPS) information, and wireless transmission to a computer on the ground. The internal electronics of the ECU contain the radio receiver for the control servos, Motorola Oncore GPS receiver, MaxStream wireless transceiver, batteries, and supporting electronics.

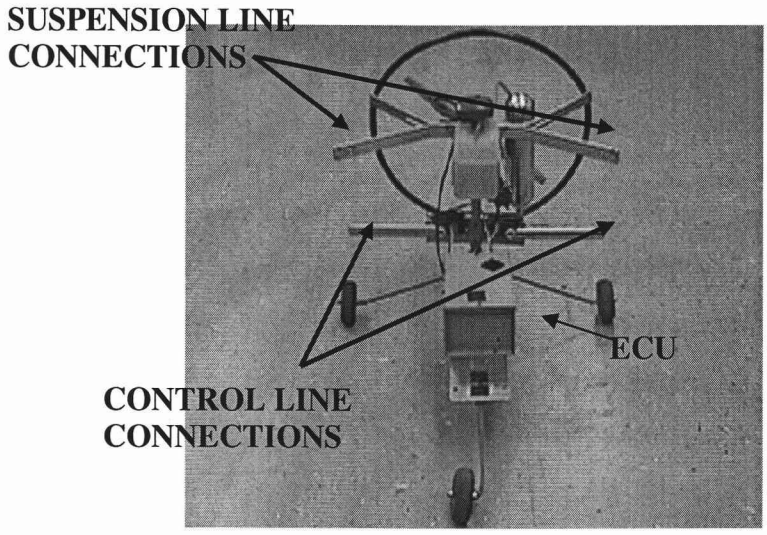

Figure 2.4 Payload

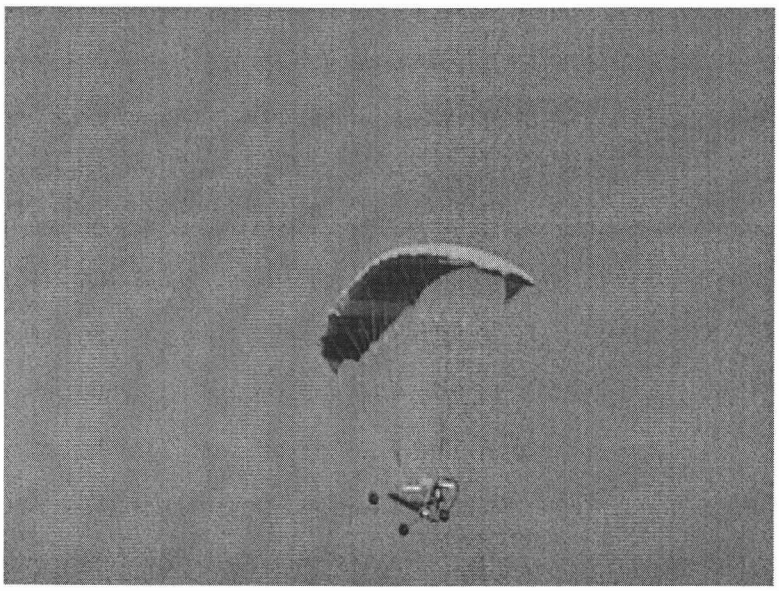

Figure 2.5 Parafoil and Payload in Flight

FLIGHT TEST DESCRIPTION

A total of five flight tests were completed. Flight tests 1, 3, and 5 were given equal control deflections of increasing magnitude on both sides. Flights 2 and 4 had no

control deflection on the left side of the canopy and the same deflection as 3 and 5 respectively on the right side. The control scheduling for the flights are summarized in Table 2.1 .

Table 2.1 Flight Testing Control Deflections

Flight Test Number	Control Deflection
1	(L 0"/R 0")
2	(L 0"/R 1.375")
3	(L 1.375"/R 1.375")
4	(L 0"/R 2.875")
5	(L 2.875"/R 2.875")

Flights 1, 3, and 5 were to maintain cross range to a minimum with the parafoil and payload aircraft gliding down range to establish the glide rate. Aerodynamic coefficients of the parafoil and payload aircraft are then estimated. Flights 2 and 4 create a steady turn by constant deflection of the right control line with equal magnitudes to flights 3 and 5.

Flight tests were initiated by powering the ECU and allowing a 3-D satellite fix to be achieved by the GPS receiver, usually occurring in less than 180 sec. Once a 3-D fix was achieved the glow engine was started and the parafoil and payload aircraft was hand launched. The parafoil and payload aircraft was powered and climbed to an altitude of at least 350 ft above the ground. At sufficient altitude, control was used to minimize any turn rates of the aircraft and the engine was stopped. Control inputs for the flight tests were immediately commanded at the onset of non-powered flight. During non-powered portions of flights 1, 3, and 5 small control inputs were used to minimize cross range without disturbing glide rates. Complete results from flight 1 are shown in Figures 2.6 through 2.8 with a square designating the point where a steady state glide begins and a circle where control inputs are used initiate a flare maneuver. In Figure 2.6 the first 30 seconds of data are used to acquire a 3-D fix with

the GPS receiver. Launching of the system occurs at a time of 30 sec and from a time of 30 to 120 sec altitude data is erratic due to maneuvering during initial climb. After 120 sec the aircraft trims to a steady climb and less dramatic turn rates occur. Engine power is stopped at a time of 165 sec when a ground altitude of 375 ft is achieved. The non-powered portion of flight 1 lasts 51 sec at which time the control lines are used to create a soft landing. Figure 2.7 shows the 2-D position of the parafoil system during the flight. Figure 2.8 shows the control deflections used during the flight.

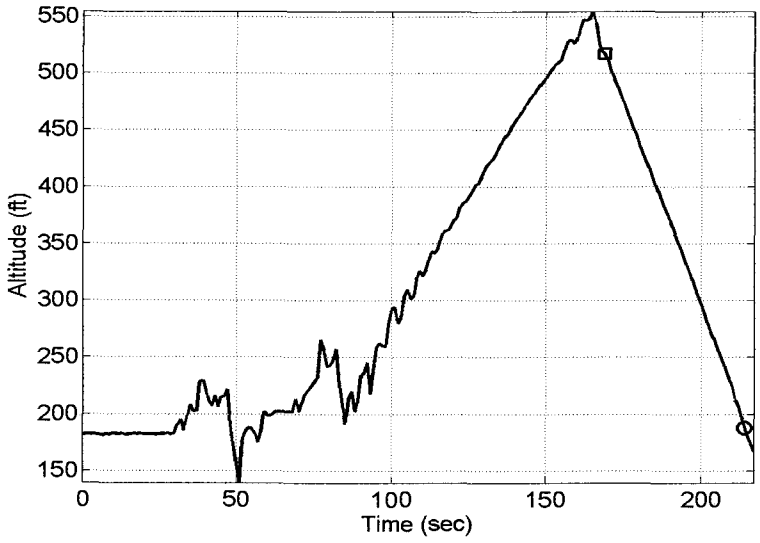

Figure 2.6 Flight 1 (L 0"/R 0") Altitude

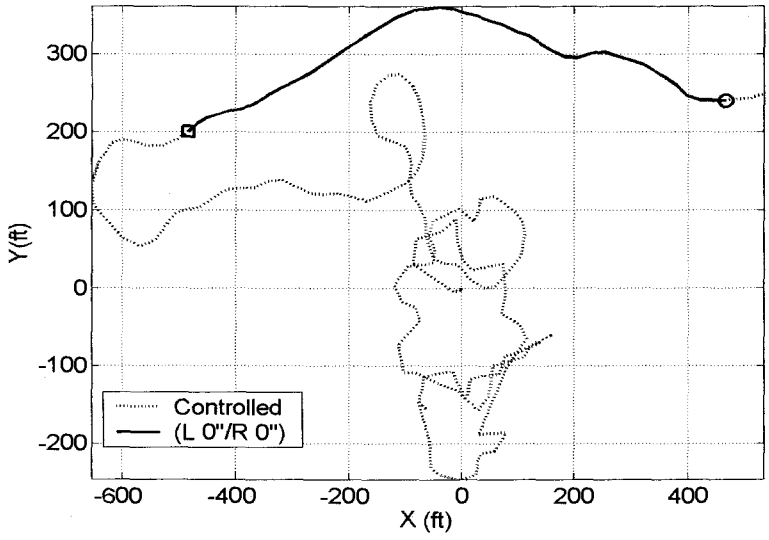

Figure 2.7 Flight 1 (L 0"/R 0") 2-D Position

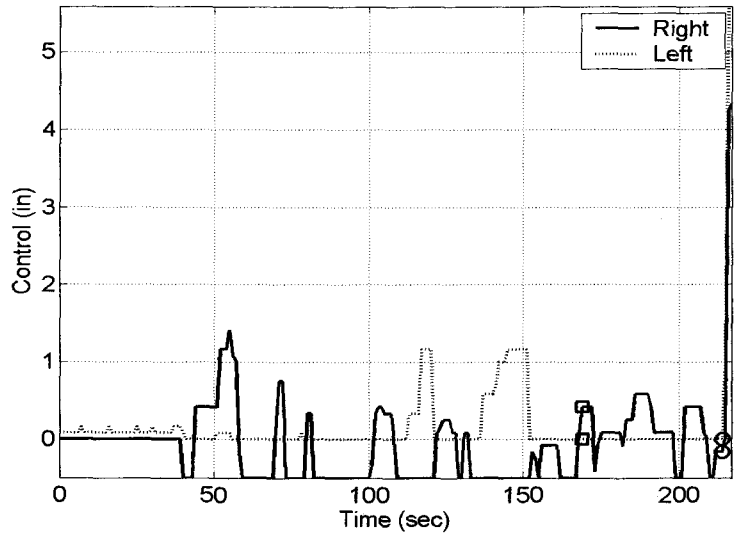

Figure 2.8 Flight 1 (L 0"/R 0") Control Deflections

The same procedure from flight 1 was followed for flight 2, however once the engine was stopped only the right control line was deflected and a steady turn results. Figure 2.9 shows the full 2-D path of flight 2 with the solid line representing the time of constant right brake deflection and a square representing the start of non-powered

flight. A circle indicates the beginning of a flare maneuver. Flight 2 control deflections are shown in Figure 2.10. The procedure from flight 1 was repeated for flights 3 and 5 while increasing control deflections. Flight 4 followed a similar procedure to flight 2.

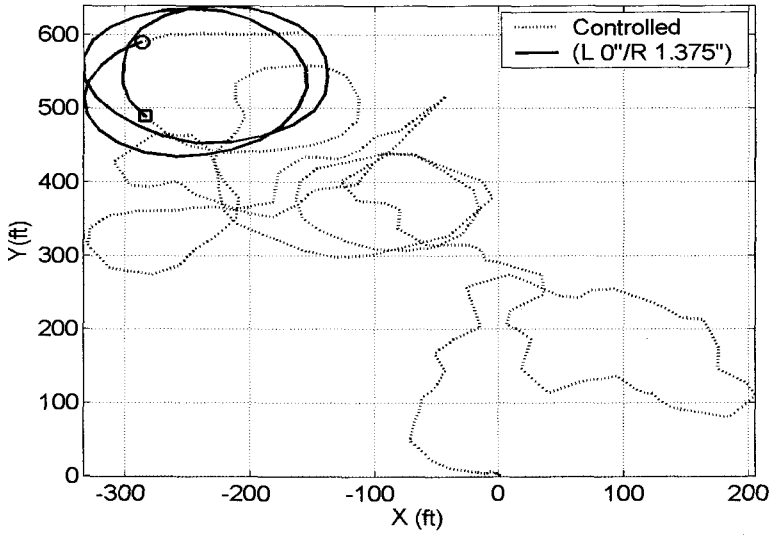

Figure 2.9 Flight 2 (L 0"/R 1.375") 2-D Position

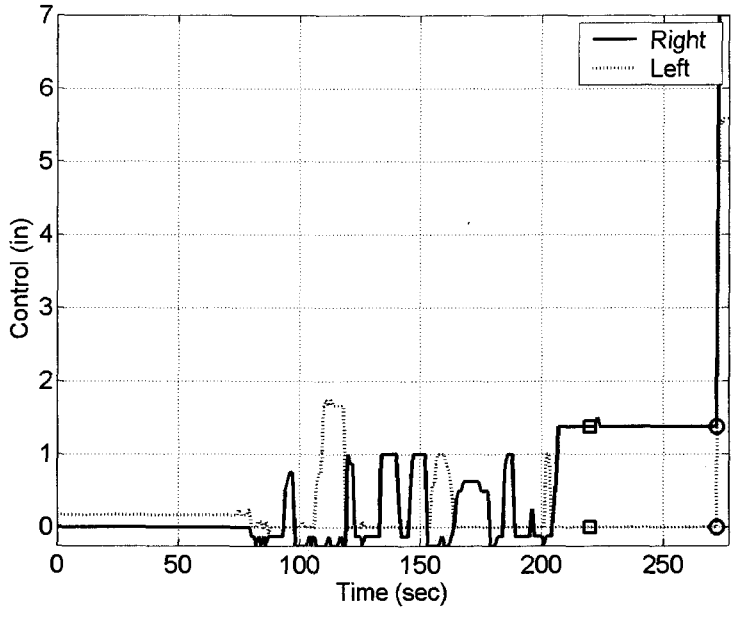

Figure 2.10 Flight 2 (L 0"/R 1.375") Control Deflection

RESULTS

Flights 1, 3, and 5 are used to estimate the glide rates for the three control cases: (L 0" / R 0"), (L 1.375"/R 1.375") and (L 2.875"/R 2.875"). Glide rates are estimated by first removing the section of non-powered flight after steady glide rate has begun but before the final flare maneuver is started, which is shown for flight 1 as the solid line in Figure 2.6. Next, the 2-D positions are converted to total distance traveled because as seen in Figure 2.6 the parafoil does not travel a straight line due to small disturbances and non-zero yaw and roll rates at the onset of non-powered flight. Finally, the total distance traveled is plotted vs. altitude. Figure 2.11 shows the glide rates for flights 1, 3, and 5 where the altitude at initial steady glide rate for all three cases was started at zero for comparison. Glide rates are estimated to be –0.32, –0.29 and –0.23 by a linear least squares fit to the flight data.

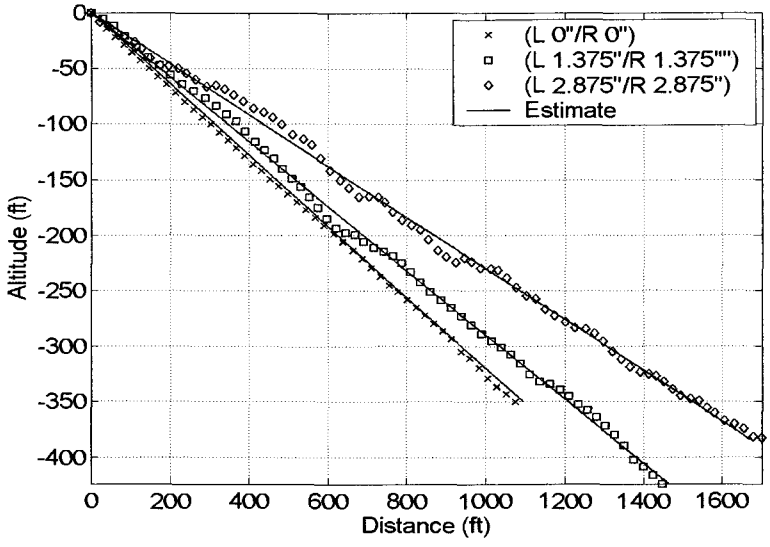

Figure 2.11 Estimated Glide Rates

The estimated glide rates are used to estimate the lift and drag coefficients needed in the dynamic model. Considering flight 1, the estimated glide rate of –0.32 can be supplemented by the average velocity of the non-powered flight estimated to be 22.4 ft/s by using the total distance traveled of 1073 ft and the flight time of 48 sec.

Parafoil lift and drag coefficients are a linear function of angle of attack with the zero angle of attack coefficients being about two-thirds the trimmed aerodynamic coefficients. The dynamic model using the physical parameters listed in Table 2.2 and the six apparent mass coefficients based on formulas by Lissaman and Brown [14] listed in Table 2.3 are used to estimate the aerodynamic coefficients. The estimated aerodynamic coefficients are listed in Table 2.4.

Table 2.2 Physical Parameters

Parameter	Value	Description
n	5	Number of Panels
α_1	25 deg	Panel 1 Angle
α_2	-25 deg	Panel 2 Angle
α_3	20 deg	Panel 3 Angle
α_4	-20 deg	Panel 4 Angle
α_5	0 deg	Panel 5 Angle
η	-11.5 deg	Incidence Angle
S	2.61 ft^2	Panel Area
t	4 in	Panel thickness
w_p	0.45 lbf	Parafoil Weight
w_s	4.1 lbf	Payload Weight

Table 2.3 Apparent Mass Coefficients

Coefficient	Value
A	0.0019
B	0.00021
C	0.044
I_A	0.11
I_B	0.010
I_C	0.0070

Table 2.4 Estimated Aerodynamic Coefficients

Parameter	Flight 1	Flight 3	Flight 5
α (deg)	7.4	5.7	2.8
$C_L(\alpha_T)$	.571	.757	1.08
$C_D(\alpha_T)$	.168	.169	.161

Using the estimated aerodynamic coefficients the dynamic model is used to compare the turn rates from the simulations of flight 2 (L 0"/R 1.375") and flight 4 (L 0"/R 2.875"). Figures 2.12 and 2.13 show the cross range and turn rates from the simulation of flight 2. With only the effect of parafoil brake deflection in the model, response to right control deflection is a sharp spiraling turn with negative turn rates, in contrast to the smooth positive turn rate measured from the experimental system.

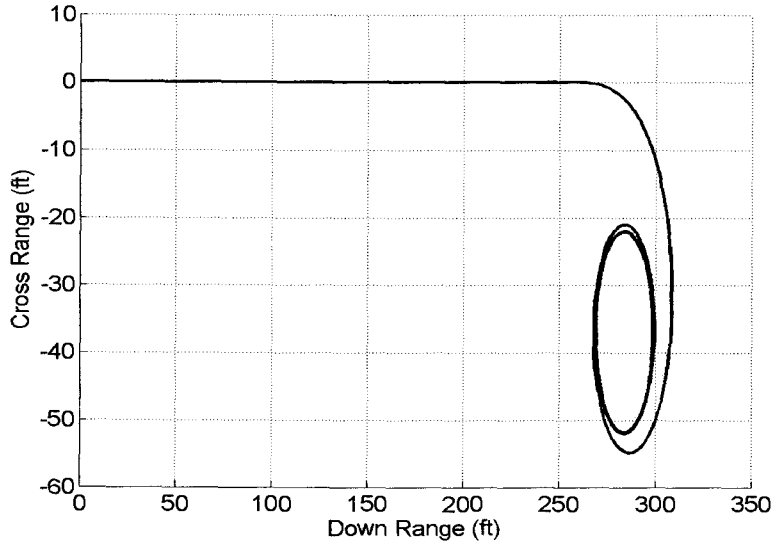

Figure 2.12 Model Prediction of Flight 2 (L 0"/R 1.375") Cross Range

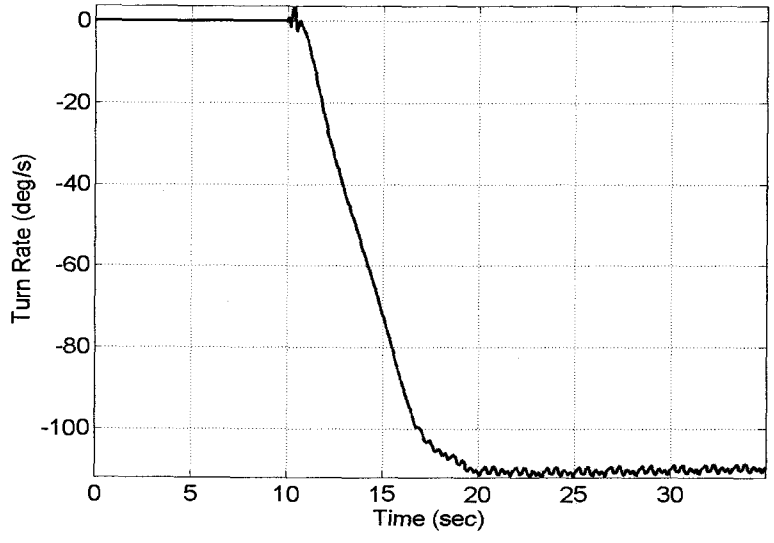

Figure 2.13 Model Prediction of Flight 2 (L 0"/R 1.375") Turn Rate

This response is caused by the large predicted increase in lift from control deflection required for the glide rates in flights 3 and 5. Now that only one side has a control deflection the increased lift causes a banking of the canopy to the opposite direction. Modeling the deflection of one control line more than the other simply by a rear panel

deflection does not adequately capture the dynamics for this experimental system. The control line on each side is attached to both a rear flap and the edge of the canopy as shown in Figure 2.1. Deflection of the control on one side more than the other side not only deflects the rear flaps but also creates subtle tilting of the canopy to one side. This suggests that the model should also adjust the panel angles during control inputs. The exact amount of canopy tilting falls between two extreme cases of zero and full canopy tilt. Figure 2.14 presents the geometry for the control arms and the range of canopy tilt for flight 1 is between 0 and 5.5 deg and between 0 and 10.4 deg for flight 2, with the actual canopy tilt falling between the two extremes. Using the 9 DOF model it was found that 1.375 deg of canopy tilt was required to replicate the turn rates from flight 2 and 2.970 deg for flight 4. Figures 2.15 and 2.16 show measured and simulated turn rates for flights 2 and 4 with canopy tilt added to the simulation model.

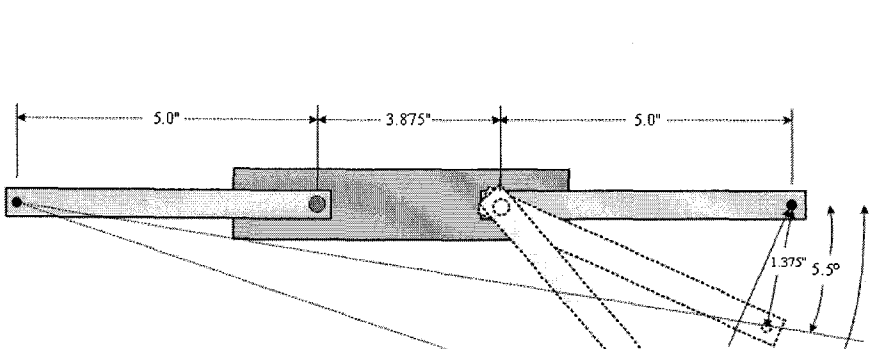

Figure 2.14 Servo Geometry

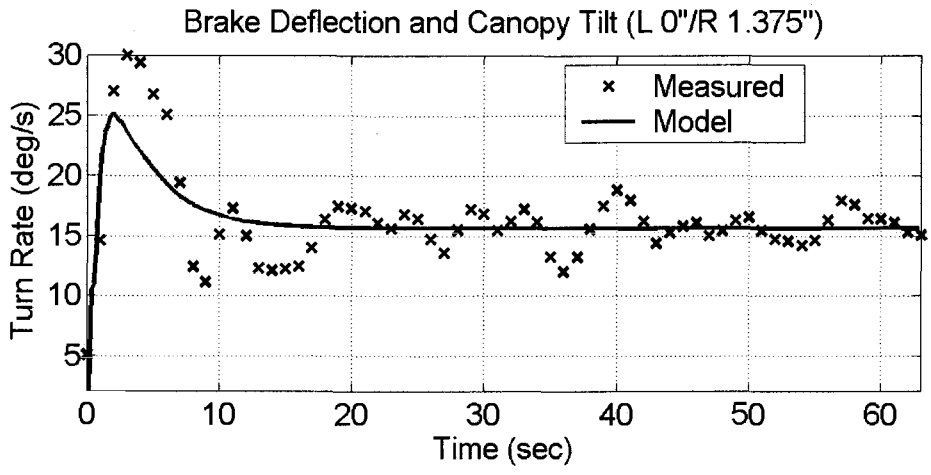

Figure 2.15 Canopy Tilt Corrected Model
Prediction of Flight 2 (L 0"/R 1.375") Turn Rate

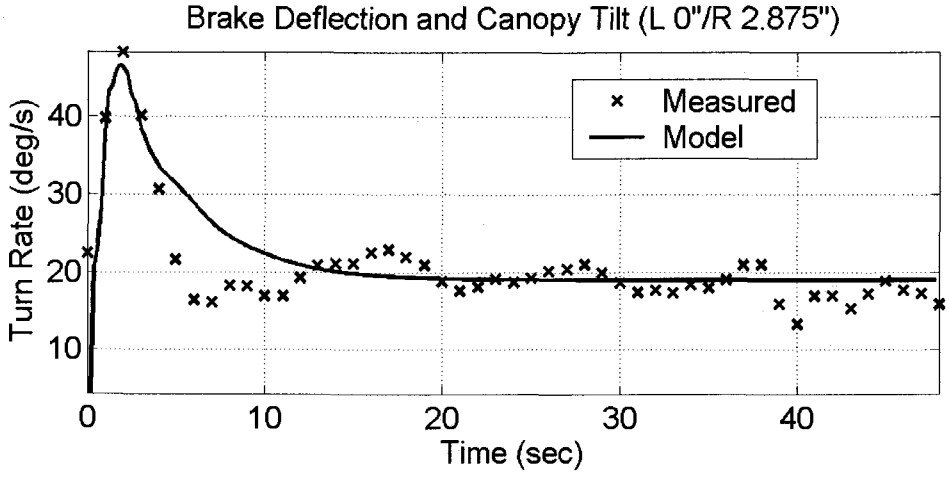

Figure 2.16 Canopy Tilt Corrected Model
Prediction of Flight 4 (L 0"/R 2.875") Turn Rate

Due to fact that parafoil canopies are flexible membranes, pulling down on the canopy on one side causes the parafoil brake to deflect and also causes the parafoil canopy to tilt down on the side where the brakes are deflected. This phenomenon is true not only for configurations where one or more of the control lines is connected to the side of the parafoil but also configurations where the control lines are connected to the outboard rear of the canopy only. It is also interesting to note that the effects of

parafoil brake deflection and canopy tilt cause response in different directions. For low glide rate parafoils where the lift to drag ratio is large, parafoil brake deflection causes a roll steer effect where a small brake deflection creates increased lift leading to roll and yaw. Thus the effect of pure right parafoil brake deflection may causes a left turn when the parafoil lift to drag ratio is large. On the other hand when the canopy tilts to the right the lift force also tilts to the right leading to a right turn. The actual control response is a complex phenomenon where two opposing effects are combined for overall control response.

CONCLUSIONS

Dynamic simulation models for flight mechanics of parafoil and payload aircraft most often employ a 6 or 9 DOF representation. During flight, the parafoil canopy is modeled as a rigid body. Conventionally, the affects of control inputs are idealized by deflection of parafoil brakes on the left and right side of the parafoil. Using a small parafoil and payload aircraft, glide rate and turn performance was measured and compared against a 9 DOF simulation model. The experimental aircraft control line connection to the parafoil consisted of two lines on the outboard rear section of the parafoil and two lines on the outboard side of the parafoil causing both effective brake deflection along with canopy tilt. When contrasting the flight test data with simulation results, it was found that using only parafoil brake deflection in the model could not replicate the turn response of the aircraft. In fact, with only parafoil brake deflection in the model, steering in the opposite direction of experimental data are exhibited. However, when both parafoil brake deflection and canopy tilt is included in the simulation model, turn performance of the system can be well replicated. Thus, for controllable parafoil and payload aircraft a dynamic model should include the effect of right and left parafoil brake deflection and canopy tilt to replicate system turning dynamics.

REFERENCES

[1] Wolf, D., "Dynamic Stability of Nonrigid Parachute and Payload System," *Journal of Aircraft*, Vol. 8 No. 8, pp. 603-609, 1971.

[2] Doherr, K., Schiling, H., "9 DOF-simulation of Rotating Parachute Systems," AIAA 12th. Aerodynamic Decelerator and Balloon Tech. Conf, 1991.

[3] Hailiang, M., Zizeng, Q., "9-DOF Simulation of Controllable Parafoil System for Gliding and Stability," *Journal of National University of Defense Technology*, Vol. 16 No. 2, pp. 49-54, 1994.

[4] Iosilevskii, G., "Center of Gravity and Minimal Lift Coefficient Limits of a Gliding Parachute," *Journal of Aircraft*, Vol. 32 No. 6, pp. 1297-1302, 1995.

[5] Brown, G.J, "Parafoil Steady Turn Response to Control Input," AIAA Paper 93-1241.

[6] Zhu, Y., Moreau, M., Accorsi, M., Leonard J.,Smith J., "Computer Simulation of Parafoil Dynamics," AIAA 2001-2005, AIAA 16th Aerodynamic Decelerator Systems Technology Conference, May 2001.

[7] Gupta, M., Xu, Z., Zhang, W., Accorsi, M., Leonard, J., Benney R., Stein., "Recent Advances in Structural Modeling of Parachute Dynamics," AIAA 2001-2030, AIAA 16th Aerodynamic Decelerator Systems Technology Conference, May 2001.

[8] Ware, G.M., Hassell, Jr., J.L., "Wind-Tunnel Investigation of Ram-Air_Inflated All-Flexible Wings of Aspect Ratios 1.0 to 3.0," NASA TM SX-1923,1969.

[9] Iacomini, C.S., Cerimele, C.J., "Lateral-Directional Aerodynamics from a Large Scale Parafoil Test Program," AIAA Paper 99-1731.

[10] Iacomini, C.S., Cerimele, C.J., "Longitudinal Aerodynamics from a Large Scale Parafoil Test Program," AIAA Paper 99-1732.

[11] Lissaman, P.B.S., Brown, G. J., "Apparent Mass Effects on Parafoil Dynamics," AIAA Paper 93-1236

ON THE USE OF RIGGING ANGLE AND CANOPY TILT FOR CONTROL OF A PARAFOIL AND PAYLOAD SYSTEM

Nathan Slegers and Mark Costello

AIAA Atmospheric Flight Mechanics Conference and Exhibit
AIAA Paper 2003-5609, Austin, Texas

ON THE USE OF RIGGING ANGLE AND CANOPY TILT FOR CONTROL OF A PARAFOIL AND PAYLOAD SYSTEM

Nathan Slegers* Mark Costello†
Department of Mechanical Engineering
Oregon State University
Corvallis, Oregon 97331

ABSTRACT

Controllable parafoil and payload aircraft are typically controlled with downward deflection of left and right parafoil brakes. Lateral control is obtained by differential deflection while longitudinal control is created by collective deflection of the left and right side parafoil brakes. The work reported considers an alternative method to control parafoil and payload air vehicles by tilting the parafoil canopy for lateral control and changing rigging angle for longitudinal control. Using a nonlinear 9 degree-of-freedom (DOF) simulation model, it is shown that canopy tilt provides a powerful lateral control mechanism and rigging angle provides a viable longitudinal control mechanism.

* Graduate Research Assistant, Department of Mechanical Engineering, Member AIAA.
† Associate Professor, Department of Mechanical Engineering, Member AIAA.

NOMENCLATURE

x, y, z : Components of position vector of point C in an inertial frame.

ϕ_b, θ_b, ψ_b : Euler roll, pitch and yaw angles of payload.

ϕ_p, θ_p, ψ_p : Euler roll, pitch and yaw angles of parafoil.

$\dot{x}, \dot{y}, \dot{z}$: Components of velocity vector of point C in an inertial frame.

p_b, q_b, r_b : Components of angular velocity of payload in payload reference frame (b).

p_p, q_p, r_p : Components of angular velocity of parafoil in parafoil reference frame (p).

m_b, m_p : Mass of payload and parafoil.

I_b, I_p : Inertia matrix of payload and parafoil with respect to their mass centers.

I_F, I_M : Apparent mass force and moment coefficient matrices.

η : Rigging Angle.

τ : Canopy tilt.

T_p : Transformation matrix from inertial reference frame to parafoil reference frame.

T_b : Transformation matrix from inertial reference frame to payload reference frame.

F_A^b, F_A^p : Aerodynamic force components on payload and parafoil in their respective frames.

W_b, W_p : Weight payload and parafoil in their respective body frames.

M_C : Constraint moment components at Joint C.

S_c^a : Skew symmetric cross product operator distance vector from joint C to apparent mass center.

S_c^p : Skew symmetric cross product operator of distance vector from joint C to parafoil canopy mass center.

S_p^a : Skew symmetric cross product operator of distance vector from parafoil canopy mass center to apparent mass center.

S_{ω}^{p} : Skew symmetric cross product operator of parafoil angular velocity.

S_{ω}^{b} : Skew symmetric cross product operator of payload angular velocity.

INTRODUCTION

Compared to conventional fixed wing aircraft configurations, parafoil and payload air vehicles are compact and lightweight before launch, exhibit relatively long endurance, fly at low speed, and impact ground with low vertical velocity. For some air vehicle missions these characteristics are quite attractive, particularly for autonomous micro aircraft with long-term sensing or sensitive equipment delivery requirements.

The most common means to steer a parafoil is through deflection of right and left brakes on the parafoil. Iacomini and Cerimele [1] performed a detailed study on the turn performance of the X-38 parafoil and demonstrated extraction of lateral-directional aerodynamic coefficients from flight data. This data was inserted into an 8 degree-of-freedom parafoil and payload model for flight simulation validation. They noted that under certain conditions, adverse turn rates can be experienced, which they attributed to parafoil brake reflex. Jann [2] considered turn performance of the ALEX parafoil to support the development of a guided parafoil and payload system. Flight test data of parafoil turning angle was fit to a first order filter driven by brake deflection angle. Slegers and Costello [3] also considered turning performance of parafoil and payload systems and like Iacomini and Cerimele [1] found turning performance to be a complex function of canopy curvature, rigging angle, and brake deflection. They showed right and left parafoil brake deflection exhibit two basic modes of lateral control, namely, skid and roll steering, which generate lateral response in opposite directions. This control reversal is a complex function of rigging angle, canopy curvature, aerodynamic properties of the parafoil, as well as parafoil

brake deflection magnitude and is particularly bothersome for autonomous systems that must automate control activity.

While left and right parafoil brake deflection is far and away the most common method of control, other control mechanisms for parafoil and payload systems are possible. For example, a method to affect turn control for a parafoil and payload system is to create an asymmetry in the suspension line lengths on both sides of the parafoil leading to a tilted canopy. Also, rigging angle has a powerful effect on the descent rate of the system. Large negative rigging angles lead to larger descent rates but are more stable at higher forward speed while rigging angles close to zero lead to lower descent rates but are less stable at high forward speed. For longitudinal control, the rigging angle can be dynamically changed in flight. While direct canopy tilt and dynamic rigging angle control appear on the surface to offer a viable control mechanism they have to date been unexplored in literature.

The work reported here explores the capability of canopy tilt for lateral control and dynamic rigging angle for longitudinal control of parafoil and payload systems. The paper begins with a description of a 9 degree-of-freedom (DOF) simulation model used to make predictions and is followed by employing the model to predict control performance of a small autonomous parafoil and payload system. The effect of canopy tilt angle on turn rate, velocity, angle of attack, and glide rate is documented. Glide rate response for conventional symmetric brake deflection is contrasted against glide rate response with dynamic rigging angle.

PARAFOIL AND PAYLOAD SYSTEM MODEL

Figure 3.1 shows a schematic of the parafoil and payload system. With the exception of movable parafoil brakes, the parafoil canopy is considered to be a fixed shape once it has inflated. The combined system of the parafoil canopy and the payload is represented with a 9 degree-of-freedom model, originally developed by

Slegers and Costello [3]. The degrees-of-freedom include three inertial position components of the joint C as well as the three Euler orientation angles of the parafoil canopy and the payload. The canopy shape is modeled as a collection of panels oriented at fixed angle with respect to each other as shown in Figure 3.2.

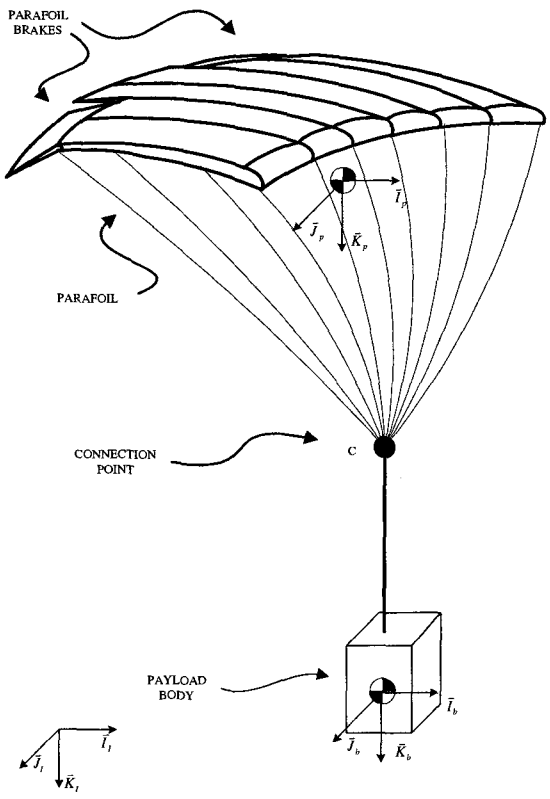

Figure 3.1 Parafoil and Payload

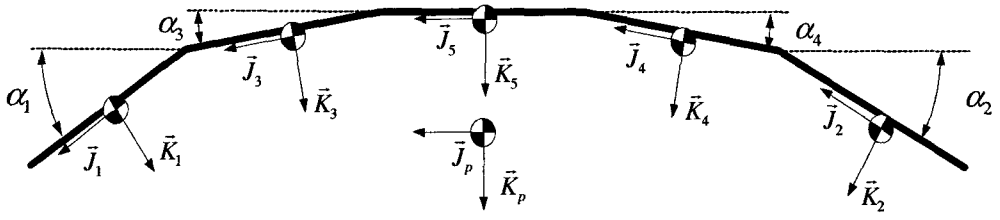

Figure 3.2 Parafoil Canopy Geometry

Connected to the outboard end panels are brakes that locally deflect the canopy downward. The parafoil canopy is connected to joint C by a rigid massless link from the mass center of the canopy. The payload is connected to joint C by a rigid massless link from the mass center of the payload. Both the parafoil and the payload are free to rotate about joint C but are constrained by the force and moment at the joint. Kinematic equations of motion for the parafoil canopy and the payload are provided in Equations 1 through 3.

$$\begin{Bmatrix} \dot{x}_c \\ \dot{y}_c \\ \dot{z}_c \end{Bmatrix} = \begin{Bmatrix} u_c \\ v_c \\ w_c \end{Bmatrix} \tag{1}$$

$$\begin{Bmatrix} \dot{\phi}_b \\ \dot{\theta}_b \\ \dot{\psi}_b \end{Bmatrix} = \begin{bmatrix} 1 & s_{\phi_b} t_{\theta_b} & c_{\phi_b} t_{\theta_b} \\ 0 & c_{\phi_b} & -s_{\phi_b} \\ 0 & s_{\phi_b}/c_{\theta_b} & c_{\phi_b}/c_{\theta_b} \end{bmatrix} \begin{Bmatrix} p_b \\ q_b \\ r_b \end{Bmatrix} \tag{2}$$

$$\begin{Bmatrix} \dot{\phi}_p \\ \dot{\theta}_p \\ \dot{\psi}_p \end{Bmatrix} = \begin{bmatrix} 1 & s_{\phi_p} t_{\theta_p} & c_{\phi_p} t_{\theta_p} \\ 0 & c_{\phi_p} & -s_{\phi_p} \\ 0 & s_{\phi_p}/c_{\theta_p} & c_{\phi_p}/c_{\theta_p} \end{bmatrix} \begin{Bmatrix} p_p \\ q_p \\ r_p \end{Bmatrix} \tag{3}$$

The common shorthand notation for trigonometric functions is employed where $\sin(\alpha) \equiv s_\alpha$, $\cos(\alpha) \equiv s_\alpha$ and $\tan(\alpha) \equiv t_\alpha$.

The kinetic equations of motion are formed by first separating the system at the coupling joint, exposing the joint constraint force and moment acting on both bodies. The translational and rotational dynamics are inertially coupled because the position degrees of freedom of the system are the inertial position vector components of the coupling joint. The constraint force is a quantity of interest to monitor during the simulation so it is retained in the dynamic equations rather than being algebraically eliminated. Equation 4 represents the translational and rotational dynamic equations of both the parafoil and payload concatenated into matrix form.

$$\begin{bmatrix} -m_b S_c^b & 0 & m_b T_b & -T_b \\ 0 & -I_F S_c^a - m_p S_c^p & I_F T_p + m_p T_p & T_p \\ I_b & 0 & 0 & S_c^b T_b \\ 0 & I_M + I_p - S_p^a I_F S_c^a & S_p^a I_F T_p & -S_c^p T_p \end{bmatrix} \begin{Bmatrix} \dot{p}_b \\ \dot{q}_b \\ \dot{r}_b \\ \cdots \\ \dot{p}_p \\ \dot{q}_p \\ \dot{r}_p \\ \cdots \\ \ddot{x}_c \\ \ddot{y}_c \\ \ddot{z}_c \\ \cdots \\ F_{xc} \\ F_{yc} \\ F_{zc} \end{Bmatrix} = \begin{Bmatrix} B_1 \\ B_2 \\ B_3 \\ B_4 \end{Bmatrix} \tag{4}$$

The matrix in Equation 4 is a block 4 x 4 matrix where each element is a 3 x 3 matrix. Rows 1-3 in Equation 4 are forces acting on the payload mass center expressed in the payload frame and rows 7-9 are the moments about the payload mass center also in the payload frame. Rows 4-6 in Equation 4 are forces acting on the parafoil mass center expressed in the parafoil frame and rows 10-12 are the moments about the parafoil mass center also in the parafoil frame. Equations 5 through 8 provide the right hand side vector of Equation 4.

$$B_1 = W_b + F_A^b - m_b S_\omega^b S_\omega^b \begin{Bmatrix} x_{cb} \\ y_{cb} \\ z_{cb} \end{Bmatrix} \tag{5}$$

$$\begin{aligned} B_2 = W_p + F_A^p - I_F \dot{T}_p \begin{Bmatrix} \dot{x} \\ \dot{y} \\ \dot{z} \end{Bmatrix} - S_\omega^p I_F \begin{Bmatrix} u_A \\ v_A \\ w_A \end{Bmatrix} \\ - m_p S_\omega^p S_\omega^p \begin{Bmatrix} x_{cp} \\ y_{cp} \\ z_{cp} \end{Bmatrix} \end{aligned} \tag{6}$$

$$B_3 = M_c - S_w^b I_b \begin{Bmatrix} p_b \\ q_b \\ r_b \end{Bmatrix} \tag{7}$$

$$B_4 = M_A - T_p T_b^T M_c - S_\omega^p (I_p + I_M) \begin{Bmatrix} p_p \\ q_p \\ r_p \end{Bmatrix} - S_p^a I_F \dot{T}_p \begin{Bmatrix} \dot{x} \\ \dot{y} \\ \dot{z} \end{Bmatrix} - S_p^a S_\omega^p I_F \begin{Bmatrix} u_A \\ v_A \\ w_A \end{Bmatrix} \quad (8)$$

Equation 4 is solved using LU decomposition and the equations of motion described above are numerically integrated using a fourth order Runge-Kutta algorithm to simulate the motion of the system.

The focus of this paper is to analytically investigate the control response caused by direct canopy tilt and dynamic rigging angle. Canopy tilt is modeled by rotating the canopy about an outboard edge as shown in Figure 3.3. Canopy tilt can be implemented by mounting control lines along left and right outboard edges of the canopy. Dynamic rigging angle is modeled by rotating all parafoil canopy sections with respect to the massless link that connects the parafoil to point C. This is pictured in Figure 3.4. Dynamic rigging angle induces no change in brake deflection.

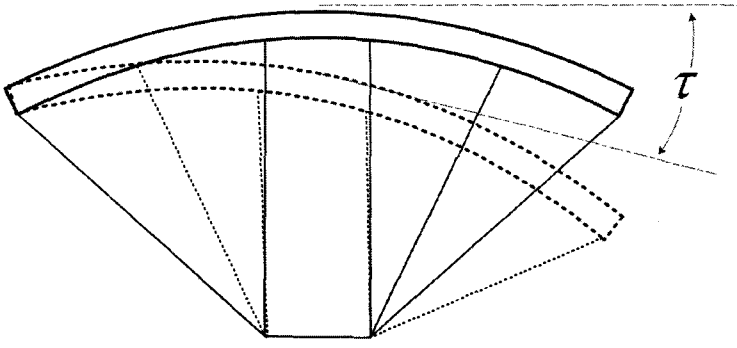

Figure 3.3 Canopy Tilting

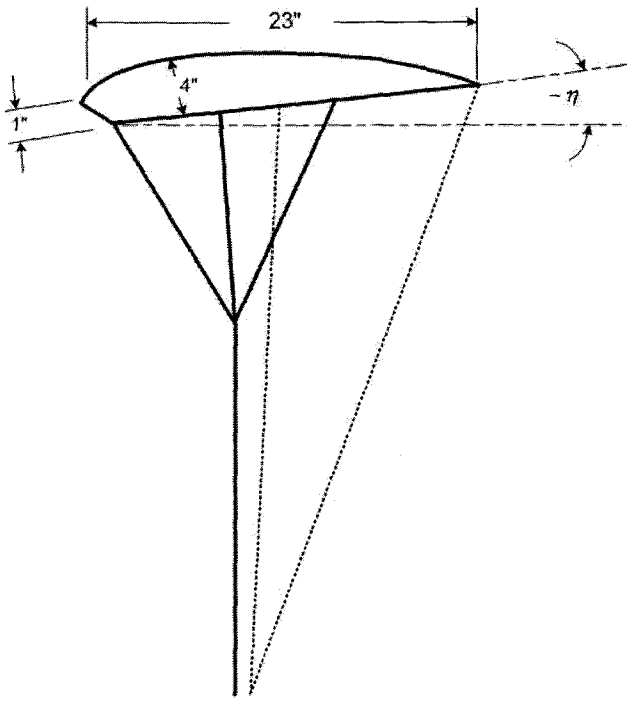

Figure 3.4 Angle of Incidence

RESULTS

In order to explore the viability of canopy tilt and rigging angle as control mechanisms for parafoil and payload systems, the model described above is used to predict steady state control response of a parafoil and payload aircraft for various canopy tilt, rigging angle, and parafoil brake settings. The parafoil and payload aircraft is identical to the configuration used by Slegers and Costello [4]. Physical parameters are listed in Tables 3.1 and 3.2. Aerodynamic coefficients were obtained from Slegers and Costello [4] and are listed in Table 3.3.

Table 3.1 Physical Parameters

Parameter	Value	Description
n	5	Number of Panels
α_1	25 deg	Panel 1 Angle
α_2	-25 deg	Panel 2 Angle
α_3	20 deg	Panel 3 Angle
α_4	-20 deg	Panel 4 Angle
α_5	0 deg	Panel 5 Angle
η	-11.5 deg	Incidence Angle
S	2.61 ft^2	Panel Area
t	4 in	Panel thickness
w_p	0.45 lbf	Parafoil Weight
w_b	4.1 lbf	Payload Weight

Table 3.2 Apparent Mass Coefficients

Coefficient	Value
A	0.0019
B	0.00021
C	0.044
I_A	0.11
I_B	0.010
I_C	0.0070

Table 3.3 Estimated Aerodynamic Coefficients

Parameter	Flight 1	Flight 3	Flight 5
α (deg)	7.4	5.7	2.8
$C_L(\alpha_T)$	.571	.757	1.08
$C_D(\alpha_T)$	.168	.169	.161

In all cases the system is launched at an altitude of 1000 *ft* with a level speed of 25 *ft/s* and is permitted to settle to a steady state condition with no control input. For the configuration under consideration this process takes 12 sec. At a prespecified time after launch, the appropriate control input is injected and held constant for the remainder of the flight. Steady turn rates are computed for canopy tilt angles from 0.0 to 3.0 *deg* in increments of 0.5 *deg* and right brake deflection from 0.0 to 2.875 *in* by increments of 0.0479 *in* and are plotted in Figure 3.5.

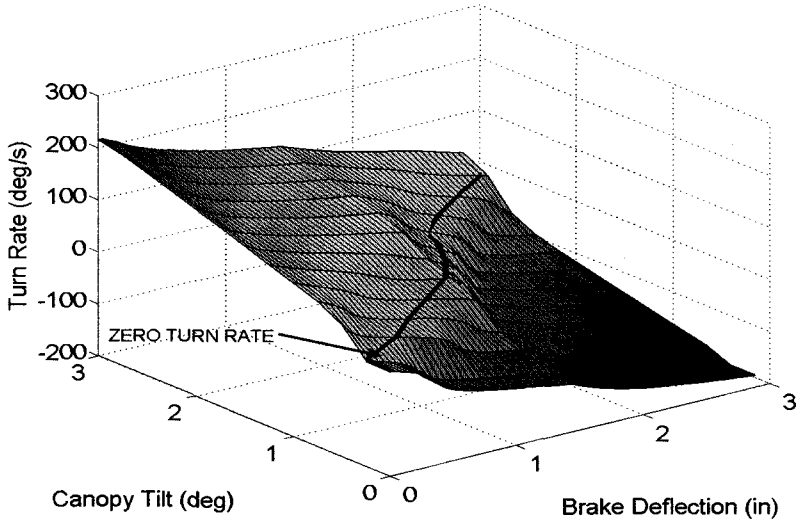

Figure 3.5 Turn Response Brake Deflection on Right Side and Positive Canopy Tilt

Canopy tilt is considered positive when the right outboard edge is moved lower. Increasing amounts of pure right brake deflection produce increasingly more negative turn rates with a turn rate of –177 *deg/s* reached for a full right brake of 2.875 *in.* Increasing amounts of pure canopy tilt produces larger positive turn rates with a maximum of 215 *deg/s* reached at 3 *deg* of canopy tilt. The extreme cases of large brake deflections with no canopy tilt and large canopy tilt with no brake deflection produce extremely large turn rates. Thus, canopy tilt provides a powerful mechanism for parafoil and payload turning.

Large positive turn rates predicted by pure canopy tilt are a result of the total canopy roll sensitivity to canopy tilt. Figure 3.6 shows the resulting canopy roll induced by canopy tilt. Total canopy roll quickly becomes large and reaches a maximum of 61 deg at 1.5 deg of canopy tilt before slightly decreasing. Canopy tilt is amplified and results in larger overall roll angles of the parafoil. Figure 3.7 shows the amplification factor of a canopy tilt input. The largest amplification factor of 83 occurs at 0.55 deg of canopy tilt. The amplification of canopy tilt into larger total canopy roll explains predicted sensitivity to small canopy tilt.

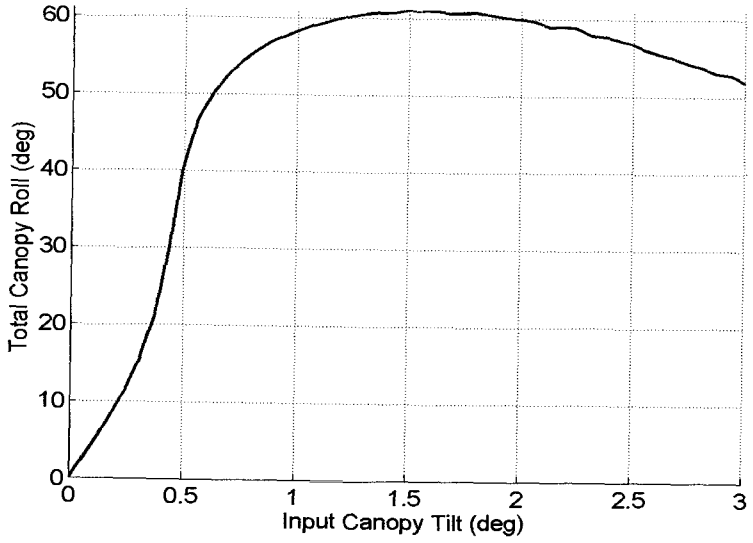

Figure 3.6 Canopy Roll Induction By Tilt

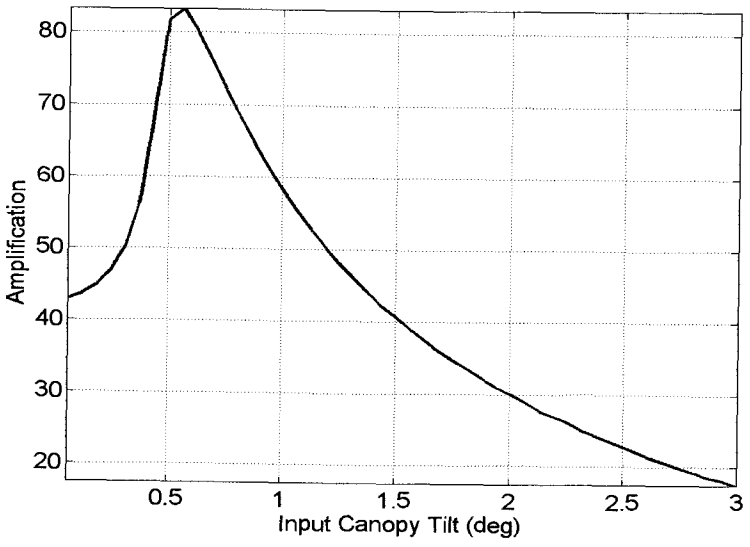

Figure 3.7 Roll Amplification

Commonly, parafoils exhibit positive turn rates when the right brake is deflected fully, opposite that predicted by a pure right brake in Figure 3.5. If right brake and positive canopy tilt are coupled so that deflecting the right brake also pulls the right outboard edge down, turn response dramatically changes from pure right brake response. A solid line in Figure 3.5 shows the intersection of the control response surface with zero turn response plane. Brake deflection causes both positive and negative turn rates depending on the amount of canopy tilt associated. Parafoil canopies are highly flexible membranes even when inflated, so that deflection of a parafoil brake on one side also tilts the canopy down on that side. The amount of canopy tilt induced by brake deflection is strongly dependent on connection of the control lines to the canopy and the number of lines on the canopy. Thus, turn performance of the parafoil and payload systems is caused by the difference of the two powerful turning mechanisms.

For longitudinal control, in flight modification of the glide slope and total velocity of the parafoil and payload system is also desirable. Commonly, speed and glide slope is controlled by deflecting both brakes simultaneously. Dynamically changing rigging angle in flight also controls glide slope and speed. Figure 3.8 shows

predicted glide slopes from symmetric brake deflection and rigging angle. Glide slope is reduced from 0.328 to under 0.248 over the range of symmetric brake deflection while reducing rigging angle from -13.5 deg to -2 deg only achieves a reduction in glide slope from 0.331 to .307.

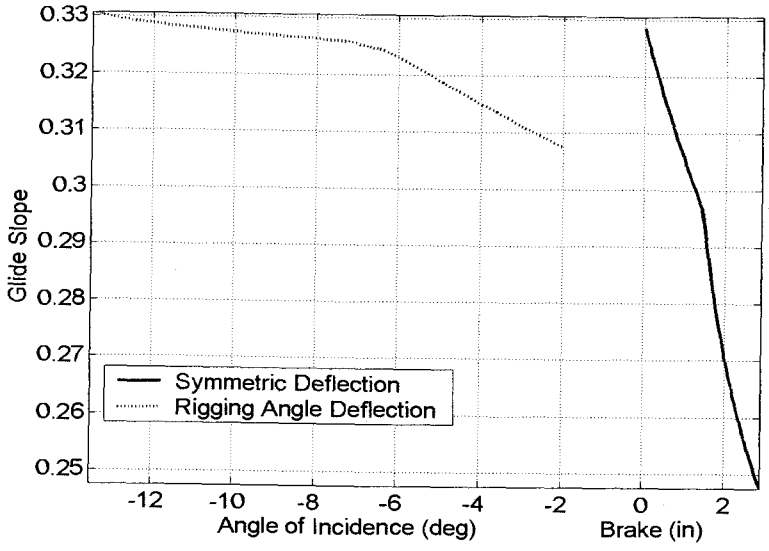

Figure 3.8 Glide Slope

Figure 3.9 shows that rigging angle deflection over the range of –13.5 deg to –2 deg yields a reduction in total velocity from 23.9 ft/s to 19.7 ft/s and from symmetric brake deflection a reduction from 22.8 ft/s to 21.1 ft/s. Figure 3.10 shows that rigging angle deflection effectively increases angle of attack thus reducing overall velocity of the system. Symmetric brake deflection only slightly alters angle of attack. Thus, decreased glide slope is not from increasing the angle of attack like dynamic rigging but instead from increasing of lift thus reducing the angle of attack. Rigging angle and symmetric brake deflections both reduce glide slope and total velocity of a parafoil and payload system but use different mechanisms. Rigging angle modification can effectively reduce the total velocity of the parafoil system and reduce the glide slope resulting in a viable longitudinal control mechanism.

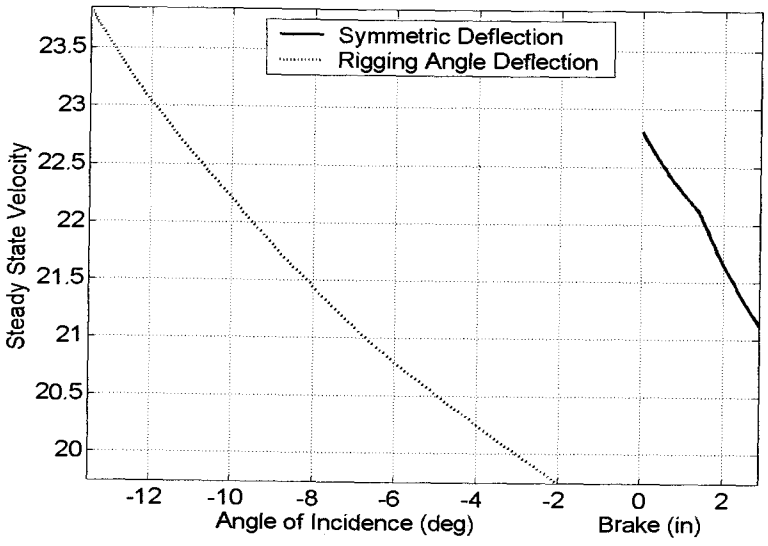

Figure 3.9 Steady State Total Velocity

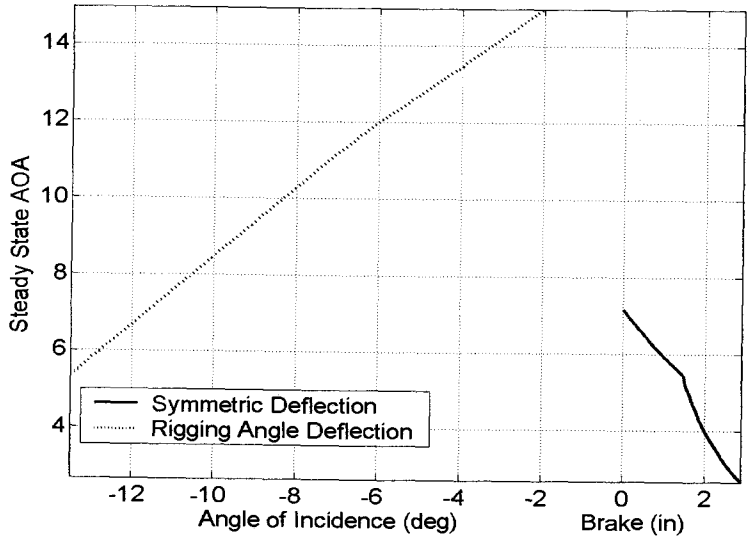

Figure 3.10 Steady State Angle of Attack

CONCLUSIONS

Due to the fact that the parafoil canopy is a flexible membrane, deflection of the control arms on one side of the parafoil may also create tilt of the canopy. Both these effects combine together to form the overall turning response. The parafoil and payload system discussed exhibits high lateral sensitivity to subtle canopy tilting. The high sensitivity to canopy tilt illustrates the importance of design parameters that alter the flexibility of the canopy namely suspension line quantity and arrangement and control line configuration. Canopy tilting can be exploited to eliminate conventional parafoil brakes for lateral direction control.

Symmetric brake deflection and rigging angle modification both demonstrate the ability to effectively alter glide slope and total velocity of the system but in different methods. Rigging angle modification alters the glide slope and total velocity by largely altering the aerodynamic angle of attack while symmetric brake deflection increases the lift only slightly increasing the angle of attack. In comparison symmetric brake deflections are more effective in altering the glide slopes and rigging angle modifications more effectively alter the total velocity.

Conventional parafoil brakes for lateral and longitudinal control could be replaced by a combination of canopy tilting for lateral control and rigging angle modification for longitudinal control. A benefit of this alternate control method is the possibility of decoupling the lateral and longitudinal control mechanisms.

REFERENCES

[1] Iacomini, C.S., Cerimele, C.J., "Lateral-Directional Aerodynamics from a Large Scale Parafoil Test Program," AIAA Paper 99-1731.

[2] Jann, T., "Aerodynamic Model Identification and GNC Design for the Parafoil-Load- System ALEX," AIAA Paper 2001-2015.

[3] Slegers, N., Costello M., "Aspects of Control for a Parafoil and Payload System," Journal of Guidance, Control and Dynamics, Vol. 26, No. 6, December 2003

[4] Slegers, N., Costello M., "Comparison of Measured and Simulated Motion of a Controllable Parafoil and Payload System," AIAA Paper 2003-5611, 2003

MODEL PREDICTIVE CONTROL OF A PARAFOIL AND PAYLOAD SYSTEM

Nathan Slegers and Mark Costello

AIAA Atmospheric Flight Mechanics Conference
AIAA Paper 2004-4705, Providence, RI 2004

MODEL PREDICTIVE CONTROL OF A PARAFOIL AND PAYLOAD SYSTEM

Nathan Slegers* Mark Costello†
Department of Mechanical Engineering
Oregon State University
Corvallis, Oregon 97331

ABSTRACT

A model predictive control strategy is developed for an autonomous parafoil and payload system. Since the technique requires a linear dynamic model of the system, a reduced state linear model based on a nonlinear 6 degree-of-freedom parafoil and payload model is established. In order to use the reduced state linear model for model predictive control the desired trajectory in the x-y plane is mapped into a desired heading angle using Lagrange interpolating polynomials. Flight test results demonstrate that a model predictive control strategy is a natural and effective method of achieving trajectory tracking in a parafoil and payload system.

* Graduate Research Assistant, Department of Mechanical Engineering, Member AIAA.
† Associate Professor, Department of Mechanical Engineering, Member AIAA.

NOMENCLATURE

x, y, z: Components of position vector of the system mass center in an inertial frame.

ϕ, θ, ψ: Euler roll, pitch and yaw angles of system.

$\dot{x}, \dot{y}, \dot{z}$: Components of velocity vector of the system mass center in an inertial frame.

p, q, r: Components of angular velocity of the system in body reference frame.

m_T: Combined mass of payload and parafoil.

I_T: Inertia matrix of combined parafoil and payload system with respect to its mass center.

T: Transformation matrix from inertial reference frame to body reference frame.

F_A: Aerodynamic force components in the body reference frame.

F_W: Combined weight of the parafoil and payload in the body frame.

S_ω: Skew symmetric cross product operator of parafoil and payload system angular velocity.

V_a: Total aerodynamic velocity of the parafoil and payload system.

$C_{L0}, C_{L\alpha}, C_{L\delta a}$: Aerodynamic lift coefficients for the parafoil and payload.

$C_{D0}, C_{D\alpha 2}, C_{D\delta a}$: Aerodynamic drag coefficients for the parafoil and payload.

$C_{l\phi}, C_{lp}, C_{l\delta a}$: Aerodynamic roll coefficients for the parafoil and payload.

$C_{m0}, C_{m\alpha}, C_{mq}$: Aerodynamic pitch coefficients for the parafoil and payload.

$C_{nr}, C_{n\delta a}$: Aerodynamic yaw coefficients for the parafoil and payload.

δ_a: Asymmetric control deflection.

δ_{bias}: Control bias.

$\overline{d}$: Control flap width.

H_p: Prediction horizon.

σ: Intersect parameter defining second point in desired path.

INTRODUCTION

An air vehicle that is light weight, flies at low speed, provides "soft" landing capability, and is compact before deployment is the parafoil and payload aircraft configuration. As the name suggests, the vehicle is comprised of a parafoil canopy connected to a payload body with suspension lines. Control is affected by two primary means, namely, deflection of left and right parafoil brakes and movement of the mass center of the complete system. These aircraft are commonly used as recreational air vehicles by aviation enthusiasts. In this case, the right and left parafoil brakes are deflected by the pilot pulling down on the right and left side control lines. The center of mass of the system is changed by the pilot through appropriate body movement. The dynamics are sufficiently slow such that expert paraglider pilots can track a desired trajectory and attain accurate ground impact. Subconsciously these pilots continuously project the trajectory forward in time and compare the results with the desired path. The error between the projected and desired path are used to determine control action.

Parafoil and payload aircraft are also particularly well suited as an autonomous air vehicle for sensing applications. These air vehicles can be released at altitude from a parent delivery aircraft or can be hand launched from the ground. For autonomous control, each individual sensor payload is fitted with an inexpensive guidance and control module. A control strategy that mimics how human pilots control paragliders is model predictive control. In model predictive control, a dynamic model of the system is used to project the state into the future and subsequently use the estimated future state to determine control action. It has been found to be a practical and powerful control technique in industrial control when future reference states are known. This paper uses model predictive control as the flight control system strategy for a parafoil and payload system. Performance of the autonomous flight control system is shown through flight tests of the system under a variety of conditions.

MODEL PREDICTIVE CONTROL

Consider a simple SISO discrete system described in state space form as given in Equation 1.

$$\begin{aligned} x_{k+1} &= Ax_k + Bu_k + D \\ y_k &= Cx_k \end{aligned} \tag{1}$$

Assume that the system matrices A, B, C and D are known and that x_k is the state vector, u_k is the control input, and y_k is the output at time k. The model described above can be used to estimate the future state of the system. Assuming a desired trajectory is known an estimated error signal $\tilde{e}_k = w_k - \tilde{y}_k$ is computed over a finite set of future time instants called the prediction horizon, H_p, where w_k is the desired output and the symbol ~ is used to represent an estimated quantity. In model predictive control, the control computation problem is cast as a finite time discrete optimal control problem. To compute the control input at a given time instant, a quadratic cost function is minimized through the selection of the control history over the control horizon. The cost function can be written as:

$$J = \left(W - \tilde{Y}\right)^T \left(W - \tilde{Y}\right) + U^T R U \tag{2}$$

where,

$$W = \begin{bmatrix} w_{k+1} & w_{k+2} & \cdots & w_{k+H_p} \end{bmatrix}^T \tag{3}$$

$$\tilde{Y} = K_{CA} x_k + K_{CAB} U + K_{CAD1} \tag{4}$$

$$U = \begin{bmatrix} u_k & u_k & \cdots & u_{k+H_p-1} \end{bmatrix}^T \tag{5}$$

and R is a symmetric positive semi-definite matrix of size H_p. Equation 1 is used to express the predicted output vector $\tilde{Y}$ in terms of the system matrices.[4]

$$K_{CA} = \begin{bmatrix} CA \\ CA^2 \\ \vdots \\ CA^{HP} \end{bmatrix} \tag{6}$$

$$K_{CAB} = \begin{bmatrix} CB & 0 & 0 & 0 & 0 \\ CAB & CB & 0 & 0 & 0 \\ CA^2B & CAB & CB & 0 & 0 \\ \vdots & \vdots & & \ddots & 0 \\ CA^{H_p-1}B & \cdots & CA^2B & CAB & CB \end{bmatrix} \tag{7}$$

$$K_{CAD1} = \begin{bmatrix} CD \\ CAD + CD \\ CA^2D + CAD + CD \\ \vdots \\ CA^{H_p-1}D + CA^{H_p-2} + \cdots + CD \end{bmatrix} \tag{8}$$

Equations 6 through 8 can be substituted into the cost function of Equation 2 resulting in the cost function in Equation 9 that is in terms of the system state x_k, desired trajectory W, control vector U and system matrices A, B, C, D and R.

$$J = \left(W - K_{CA}x_k - K_{CAB}U - K_{CAD1}\right)^T \left(W - K_{CA}x_k - K_{CAB}U - K_{CAD1}\right) + U^T RU \tag{9}$$

The control U, which minimizes Equation 9 is

$$U = \mathrm{K}\left(W - K_{CA}x_k - K_{CAD1}\right) \tag{10}$$

where,

$$\mathrm{K} = \left(K_{CAB}{}^{T} K_{CAB} + R\right)^{-1} K_{CAB}{}^{T} \tag{11}$$

Equation 10 contains the optimal control inputs over the entire control horizon, however at time k only the first element u_k is needed. The first element u_k can be extracted from Equation 10 by defining K_1 as the first row of K. The optimal control over the next time sample becomes

$$u_k = \mathrm{K}_1\left(W - K_{CA} x_k - K_{CAD1}\right) \tag{12}$$

where, calculation of the first element of the optimal control sequence requires the desired trajectory W over the prediction horizon and the current state x_k.

PARAFOIL AND PAYLOAD SYSTEM MODEL

The combined system of the parafoil canopy and the payload is represented with 6 degrees-of-freedom (DOF) including three inertial position components of the system mass center as well as the three Euler orientation angles of the parafoil and payload system. Kinematic equations of motion for the parafoil and payload system are provided in Equations 13 and 14.

$$\begin{Bmatrix} \dot{x} \\ \dot{y} \\ \dot{z} \end{Bmatrix} = T^{T} \begin{Bmatrix} u \\ v \\ w \end{Bmatrix} \tag{13}$$

$$\begin{Bmatrix} \dot{\phi} \\ \dot{\theta} \\ \dot{\psi} \end{Bmatrix} = \begin{bmatrix} 1 & s_\phi t_\theta & c_\phi t_\theta \\ 0 & c_\phi & -s_\phi \\ 0 & s_\phi / c_\theta & c_\phi / c_\theta \end{bmatrix} \begin{Bmatrix} p \\ q \\ r \end{Bmatrix} \tag{14}$$

The matrix T represents the transformation matrix from an inertial reference frame to the body reference frame.

$$T = \begin{bmatrix} c_\theta c_\psi & c_\theta s_\psi & -s_\theta \\ s_\phi s_\theta c_\psi - c_\phi s_\psi & s_\phi s_\theta s_\psi + c_\phi c_\psi & c_\theta s_\phi \\ c_\phi s_\theta c_\psi + s_\phi s_\psi & c_\phi s_\theta s_\psi - s_\phi c_\psi & c_\phi c_\theta \end{bmatrix} \tag{15}$$

The common shorthand notation for trigonometric functions is employed where $\sin(\alpha) \equiv s_\alpha$, $\cos(\alpha) \equiv c_\alpha$ and $\tan(\alpha) \equiv t_\alpha$. The dynamic equations of motion are provided in Equations 16 and 17.

$$\begin{Bmatrix} \dot{u} \\ \dot{v} \\ \dot{w} \end{Bmatrix} = \frac{1}{m_T} \left(\vec{F}_A + \vec{F}_W \right) - T S_\omega T^T \begin{Bmatrix} u \\ v \\ w \end{Bmatrix} \tag{16}$$

$$\begin{Bmatrix} \dot{p} \\ \dot{q} \\ \dot{r} \end{Bmatrix} = I_T{}^{-1} \left(\vec{M}_A - S_\omega I_T \begin{Bmatrix} p \\ q \\ r \end{Bmatrix} \right) \tag{17}$$

where,

$$S_\omega = \begin{bmatrix} 0 & -r & q \\ r & 0 & -p \\ -q & p & 0 \end{bmatrix} \tag{18}$$

$$I_T = \begin{bmatrix} I_{XX} & 0 & I_{XZ} \\ 0 & I_{YY} & 0 \\ I_{XZ} & 0 & I_{ZZ} \end{bmatrix} \tag{19}$$

$$I_T^{-1} = \begin{bmatrix} I_{XXI} & 0 & I_{XZI} \\ 0 & I_{YYI} & 0 \\ I_{XZI} & 0 & I_{ZZI} \end{bmatrix} \tag{20}$$

The weight force vector in the body reference frame is given in Equation 21.

$$\vec{F}_W = m_T g \begin{Bmatrix} -s_\theta \\ s_\phi c_\theta \\ c_\phi c_\theta \end{Bmatrix} \tag{21}$$

The aerodynamic forces acting at the system mass center and the aerodynamic moments about the system mass center are given in Equations 22 and 23 respectively.

$$\begin{aligned} \vec{F}_A = & \frac{1}{2}\rho S V_A \left(C_{L0} + C_{L\alpha}\alpha + C_{L\delta a}\delta_a\right) \begin{Bmatrix} w \\ 0 \\ -u \end{Bmatrix} \\ & -\frac{1}{2}\rho S V_A \left(C_{D0} + C_{D\alpha 2}\alpha^2 + C_{D\delta a}\delta_a\right) \begin{Bmatrix} u \\ v \\ w \end{Bmatrix} \end{aligned} \tag{22}$$

$$\vec{M}_A = \frac{1}{2}\rho S \bar{c} V_A^{\,2} \begin{Bmatrix} C_{l\phi}\phi + \dfrac{C_{lp}\bar{c}p}{2V_{air}} + \dfrac{C_{l\delta a}\delta_a}{\bar{d}} \\ C_{m0} + C_{m\alpha}\alpha + \dfrac{C_{mq}\bar{c}q}{2V_{air}} \\ \dfrac{C_{nr}\bar{c}r}{2V_{air}} + \dfrac{C_{n\delta a}\delta_a}{\bar{d}} \end{Bmatrix} \tag{23}$$

Model predictive control requires a linear model of the states to be controlled. The desired states to control in a parafoil and payload system are the inertial positions x and y. Equations 13 through 23 describing the parafoil and payload system are nonlinear and in order to apply standard model predictive control, must be linearized. Consider a parafoil and payload in a steady turn performing a helix as it falls. All the states excluding the inertial positions x, y and z and Euler yaw angle reach a steady state. The inertial positions do not appear in any of the equations of motion however; the Euler yaw angle appears in Equation 13 relating the inertial velocities to the body velocities. A linear model that accurately represents the inertial positions x, y and z of the nonlinear model must constrain the yaw angle to only small changes about a nominal yaw angle. Constraining the yaw angle in such a way limits the model to nearly straight flight and is not sufficient for general flight. Observation of a parafoil and payload system shows that the velocities u, v and w expressed in the body reference frame are nearly constant under typical flight conditions. If a reduced state $[\phi \quad \psi \quad p \quad r]^T$ is considered for model predictive control purposes then the equations for $[\dot{\phi} \quad \dot{\psi} \quad \dot{p} \quad \dot{r}]^T$ describing the rolling and pitching in Equations 14 and 17 can be linearized assuming that the aerodynamic velocity V_A is constant. Euler pitch is not included in the reduced state because after linearization pitch becomes uncoupled from both rolling and yawing motion. The equations for the reduced states are linearized about the steady state in Equation 24 and given in Equation 25 with convention that $s^* = s - s_0$.

$$s_0 = \begin{Bmatrix} \phi_0 \\ \theta_0 \\ p_0 \\ q_0 \\ r_0 \\ \delta_{a0} \end{Bmatrix} = \begin{Bmatrix} 0 \\ \theta_0 \\ 0 \\ 0 \\ 0 \\ 0 \end{Bmatrix} \tag{24}$$

$$\begin{Bmatrix} \dot{\phi}^* \\ \dot{\psi}^* \\ \dot{p}^* \\ \dot{r}^* \end{Bmatrix} = \begin{bmatrix} 0 & 0 & A_{13} & 0 \\ 0 & 0 & 0 & A_{24} \\ A_{31} & 0 & A_{33} & A_{34} \\ A_{41} & 0 & A_{43} & A_{44} \end{bmatrix} \begin{Bmatrix} \phi^* \\ \psi^* \\ p^* \\ r^* \end{Bmatrix} + \begin{bmatrix} 0 \\ 0 \\ B_3 \\ B_4 \end{bmatrix} \{\delta_a{}^*\} + \begin{bmatrix} 0 \\ 0 \\ D_1 \\ D_2 \end{bmatrix} \{\delta_{bias}\} \tag{25}$$

where,

$$A_{13} = 1 \tag{26}$$

$$A_{24} = 1/c_{\theta_0} \tag{27}$$

$$A_{31} = \frac{1}{2}\rho S\bar{c} V_{air}{}^2 C_{l\phi} I_{XXI} \tag{28}$$

$$A_{33} = \frac{1}{4}\rho S\bar{c}^2 V_{air} I_{XXI} C_{lp} \tag{29}$$

$$A_{34} = \frac{1}{4}\rho S\bar{c}^2 V_{air} I_{XZI} C_{nr} \tag{30}$$

$$A_{41} = \frac{1}{2}\rho S\bar{c} V_{air}{}^2 I_{XZI} C_{l\phi} \tag{31}$$

$$A_{43} = \frac{1}{4}\rho S\bar{c}^2 V_{air} I_{XZI} C_{lp} \tag{32}$$

$$A_{44} = \frac{1}{4}\rho S\bar{c}^2 V_{air} I_{ZZI} C_{nr} \tag{33}$$

$$B_3 = \frac{\rho S\bar{c} V_{air}{}^2 \left(C_{l\delta a} I_{XXI} + C_{n\delta a} I_{XZI}\right)}{2\bar{d}} \tag{34}$$

$$B_4 = \frac{\rho S\bar{c} V_{air}{}^2 \left(C_{l\delta a} I_{XZI} + C_{n\delta a} I_{ZZI}\right)}{2\bar{d}} \tag{35}$$

$$D_1 = \frac{\rho S\bar{c} V_{air}{}^2 I_{XZI}}{\bar{d}} \tag{36}$$

$$D_2 = \frac{\rho S\bar{c} V_{air}{}^2 I_{ZZI}}{\bar{d}} \tag{37}$$

MAPPING DESIRED X-Y PATH TO DESIRED YAW ANGLE

The typical desired trajectories of a parafoil and payload system are points in the x-y plane and according to Equation 1 the desired output must be a linear combination of the linear model states. In order to use the linear model described in Equation 25 for model predictive control the desired trajectory in the x-y plane must be mapped into a desired trajectory in terms of the reduced states $[\phi \quad \psi \quad p \quad r]^T$. A straightforward mapping is to assume that the side velocity v is small and the parafoil is traveling in the direction of its heading ψ. Equation 38 can then convert the desired path in the x-y plane to a desired heading.

$$\psi_D(t) = \tan^{-1}\left(\left.\frac{dx}{dy}\right|_t\right) \tag{38}$$

The evaluation of Equation 38 requires a continuous expression for dx/dy during the prediction horizon. A technique for determining a polynomial to connect the points $((x_0, y_0), (x_1, y_1) \cdots (x_n, y_n))$ that describe the desired path is to use a parameter t on an interval $[t_0, t_n]$, with $t_0 < t_1 < \cdots < t_n$ and construct approximations $x_i = x(t_i)$ and

$y_i = y(t_i)$ for each $i = 0,1,\cdots n$. The value of t_0 is assumed to be the time when the prediction starts. Assuming that V_A is constant the following times t_i can be approximated by dividing V_A by the distance between points (x_{i-1}, y_{i-1}) and (x_i, y_i). The continuous path in the x-y plane is approximated by constructing $x_i = x(t_i)$ and $y_i = y(t_i)$ from third order Lagrange interpolating polynomials in Equations 39 through 41.[5]

$$x(t_i) = \sum_{n=0}^{3} x_n L_n(t) \tag{39}$$

$$y(t_i) = \sum_{n=0}^{3} y_n L_n(t) \tag{40}$$

$$L_n = \frac{(t-t_0)(t-t_1)(t-t_2)(t-t_3)}{(t_n-t_0)(t_n-t_1)(t_n-t_2)(t_n-t_3)} \tag{41}$$

The continuous time derivatives of $x_i = x(t_i)$ and $y_i = y(t_i)$ are given in Equations 42 through 47.

$$\frac{dx}{dt} = \sum_{n=0}^{3} x_n LD_n \tag{42}$$

$$\frac{dy}{dt} = \sum_{n=0}^{3} y_n LD_n \tag{43}$$

$$LD_0 = \frac{(t-t_1)(t-t_2)+(t-t_1)(t-t_3)+(t-t_2)(t-t_3)}{(t_0-t_1)(t_0-t_2)(t_0-t_3)} \tag{44}$$

$$LD_1 = \frac{(t-t_0)(t-t_2)+(t-t_0)(t-t_3)+(t-t_2)(t-t_3)}{(t_1-t_0)(t_1-t_2)(t_1-t_3)} \tag{45}$$

$$LD_2 = \frac{(t-t_0)(t-t_1)+(t-t_0)(t-t_3)+(t-t_1)(t-t_3)}{(t_2-t_0)(t_2-t_1)(t_2-t_3)} \tag{46}$$

$$LD_3 = \frac{(t-t_0)(t-t_1)+(t-t_0)(t-t_2)+(t-t_1)(t-t_2)}{(t_3-t_0)(t_3-t_1)(t_3-t_2)} \tag{47}$$

Equation 38 can be solved for all time using Equation 48.

$$\left.\frac{dx}{dy}\right|_t = \left.\frac{dx/dt}{dy/dt}\right|_t \tag{48}$$

TEST SYSTEM

The parafoil and payload system used in all testing is shown in Figures 4.1 through 4.3 with the physical parameters in Table 4.1. A test flight commences by launching the system from the ground, a 10-inch propeller powers the test system to altitudes of 250 to 400 ft where the propeller is stopped and gliding commences, lasting approximately 20 seconds for every 100 feet of altitude.

Full state measurement of the parafoil required in the optimal control sequence is achieved through a sensor package that includes three single axis gyroscopes a three-axis accelerometer and a three-axis magnetometer shown in Figure 4.3. Inertial positions x and y required in the mapping of the desired x-y path into a desired yaw angle come from a Wide Area Augmentation System (WAAS) enabled Global Positioning Satellite (GPS) receiver shown in Figure 4.1. The sensors are supplemented with a wireless transceiver that transmits data from the parafoil and receives commands during flight. An operator controlled transmitter can switch control of the parafoil to one of three modes: manual, estimation or autonomous. Manual mode allows the operator to manually fly the parafoil. Estimation mode allows estimation of linear model aerodynamic coefficients required for model predictive control. Autonomous mode controls the parafoil using the optimal control calculated from the model predictive control law.

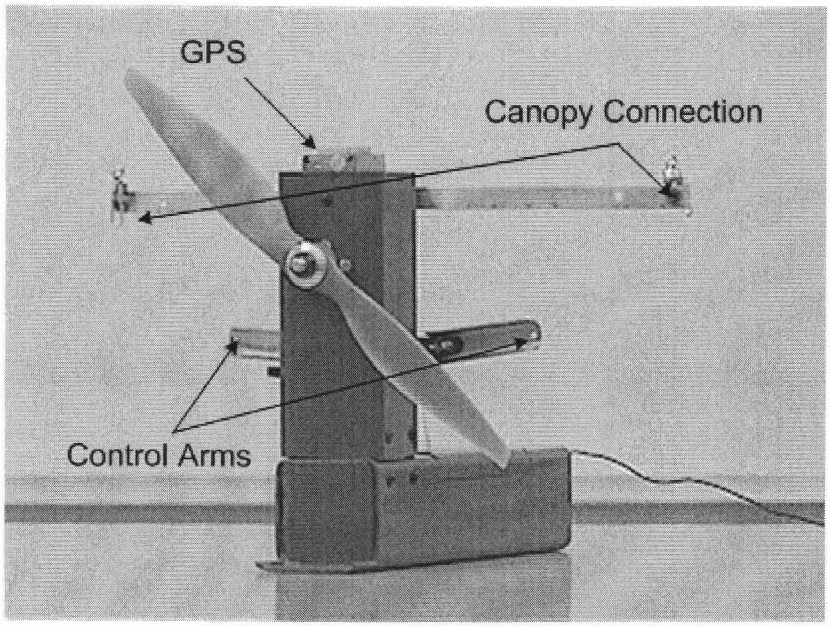

Figure 4.4.1 Payload

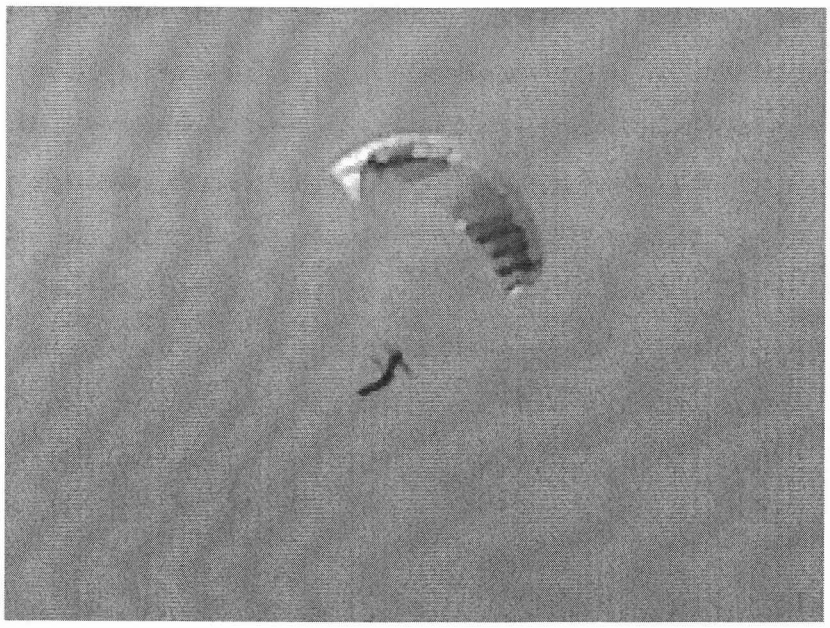

Figure 4.2 Parafoil And Payload System

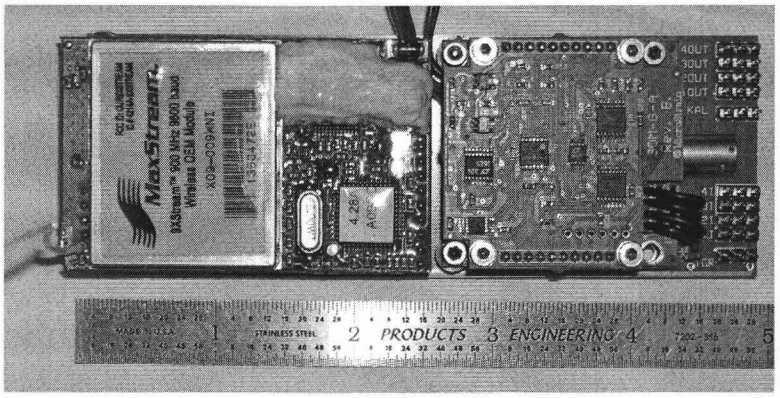

Figure 4.3 System Electronics

Table 4.1 Parafoil and Payload Physical Parameters

Variable	Value	Units
ρ	0.0023784722	Slug/ft^3
Weight	2.0	lbf
S	7.5	ft^2
$\overline{c}$	1.75	ft
$\overline{d}$	2.0	ft
Ixx	0.1357	Slug-ft^2
Iyy	0.1506	Slug-ft^2
Izz	0.0203	Slug-ft^2
Ixz	0.0025	Slug-ft^2
Ixxi	7.3845	1/(Slug-ft^2)
Iyyi	6.6423	1/(Slug-ft^2)
Izzi	49.442	1/(Slug-ft^2)
Ixzi	-0.9032	1/(Slug-ft^2)
Vair	21.6	ft/sec

IDENTIFICATION OF AERODYNAMIC COEFFICIENTS

Application of the reduced order model requires the knowledge of five constant aerodynamic coefficients: $C_{l\phi}, C_{lp}, C_{l\delta a}, C_{nr}, C_{n\delta a}$ and the constant bias term δ_{bias}. The six parameters can be estimated using recursive weighted least-squares estimation when linearly related to measurements as shown in Equation 49 where, $\vec{z}_i$ are measurements, $\vec{x}_i$ are parameters to be estimated and $\vec{n}_i$ is zero mean measurement noise.

$$\vec{z}_i = H_i \vec{x} + \vec{n}_i \tag{49}$$

The recursive weighted least squares estimation to Equation 49 is given in Equations 50 and 51 where, P_i is the covariance estimate of the states at measurement i and Q is the measurement covariance.[6]

$$\hat{x}_i = \hat{x}_{i-1} + P_k H_k{}^T Q^{-1} \left(z_k - H_k \hat{x}_k \right) \tag{50}$$

$$P_i = P_{i-1} - P_{i-1} H_i{}^T \left(Q + H_i P_{i-1} H_i{}^T \right)^{-1} H_i P_{i-1} \tag{51}$$

The matrix H_i giving a linear relationship between the parameters to be estimated and measurements is acquired by linearizing $\dot{p}^*$ and $\dot{r}^*$ in Equation 26 and is given in Equation 52.

$$H_i = \frac{\rho S \bar{c} V_{air}^{\ 2}}{2} \begin{bmatrix} Ixxi\phi_i & Ixzi\phi_i \\ Ixxi\dfrac{\bar{c}p_i}{2V_{air}} & Ixzi\dfrac{\bar{c}p_i}{2V_{air}} \\ Ixxi\dfrac{\delta_a}{\bar{d}} & Ixzi\dfrac{\delta_a}{\bar{d}} \\ Ixzi\dfrac{\bar{c}r_i}{2V_{air}} & Izzi\dfrac{\bar{c}r_i}{2V_{air}} \\ Ixzi\dfrac{\delta_a}{\bar{d}} & Izzi\dfrac{\delta_a}{\bar{d}} \\ \dfrac{Ixzi}{\bar{d}} & \dfrac{Izzi}{\bar{d}} \end{bmatrix}^T \tag{52}$$

The recursive weighted least squares estimation requires the differentiation of the measured roll and yaw rates. The control sequence shown in Figure 4.4 and used in parameter identification was chosen to be sinusoidal in order to ensure that the numerical differentiation of the roll and yaw rates produced significant signals. Figure 4.5 shows the differentiation of the measured roll and yaw rates. The recursive weighted least squares estimation is initialized with P_1 as a 6 by 6 diagonal matrix with 0.05 on each diagonal, $C_{l\phi}, C_{lp}, C_{l\delta a}, C_{nr}, C_{n\delta a}$ and δ_{bias} as -0.1, -0.5, 0.1, -0.1, 0.1 and 0 respectively. The measurement covariance Q was set as a 2 x 2 diagonal matrix with $Q_{1,1} = 0.00475$ and $Q_{2,2} = 0.0005$. The aerodynamic parameter estimations are shown in Figures 4.6 and 4.7 with the final estimates of $C_{l\phi}$, C_{lp}, $C_{l\delta a}$, C_{nr}, $C_{n\delta a}$ and δ_{bias} given in Table 4.2. being –0.0244, -0.0320, 0.0050, -0.0501, 0.0014 and –0.00017.

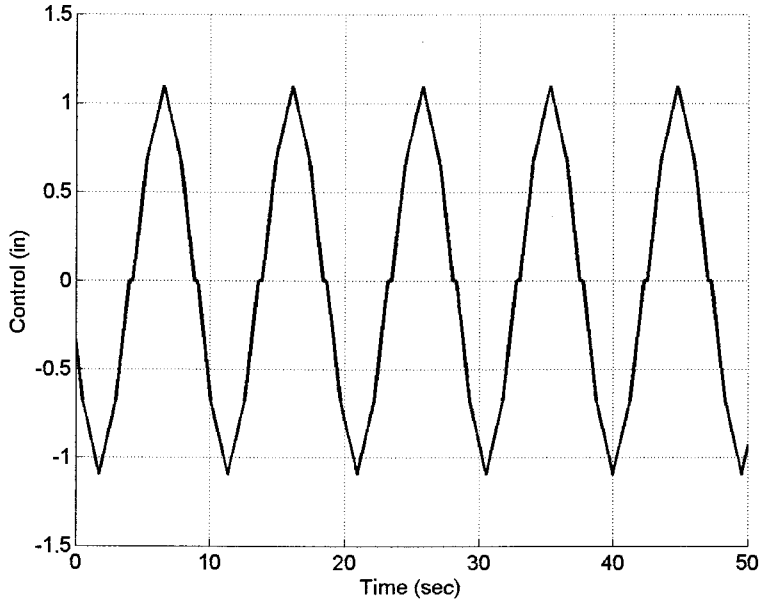

Figure 4.4 Control Sequence

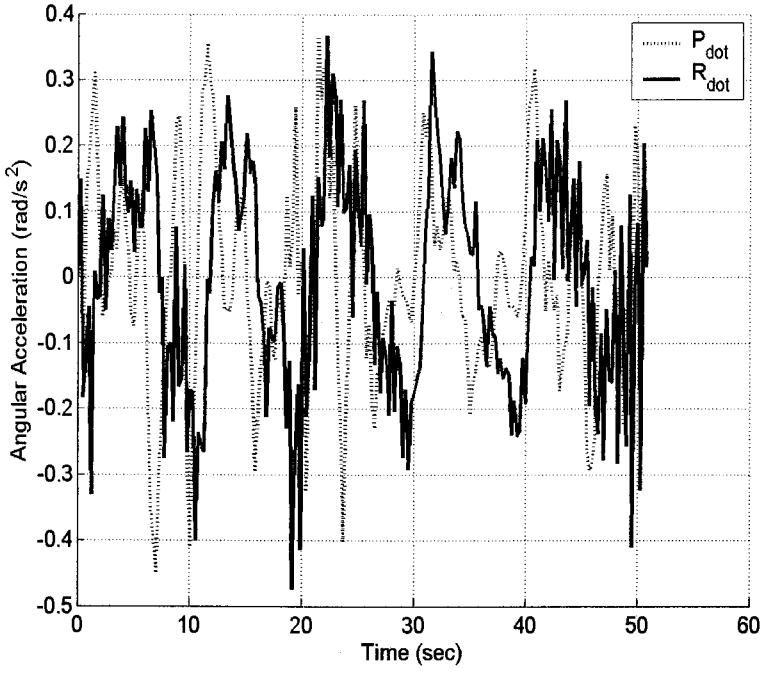

Figure 4.5 Differentiated Measured Body Roll and Yaw Rates

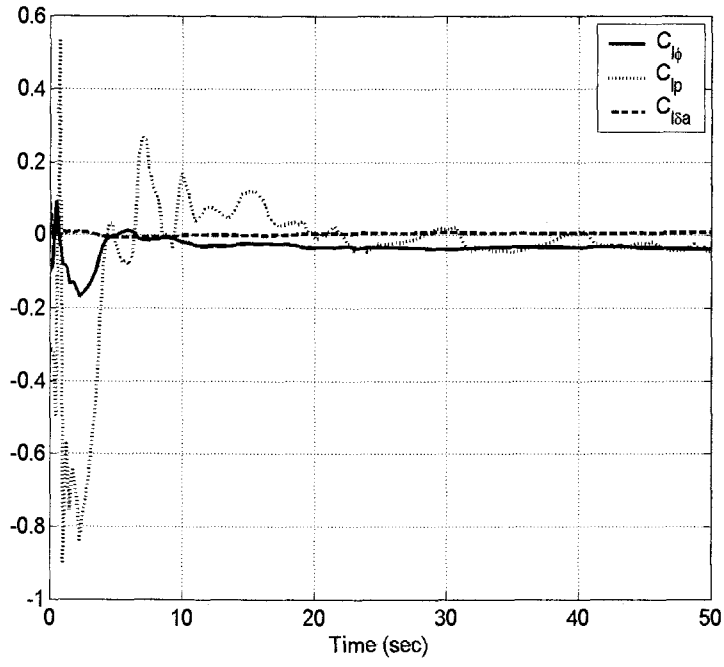

Figure 4.6 Estimated Roll Aerodynamic Coefficients

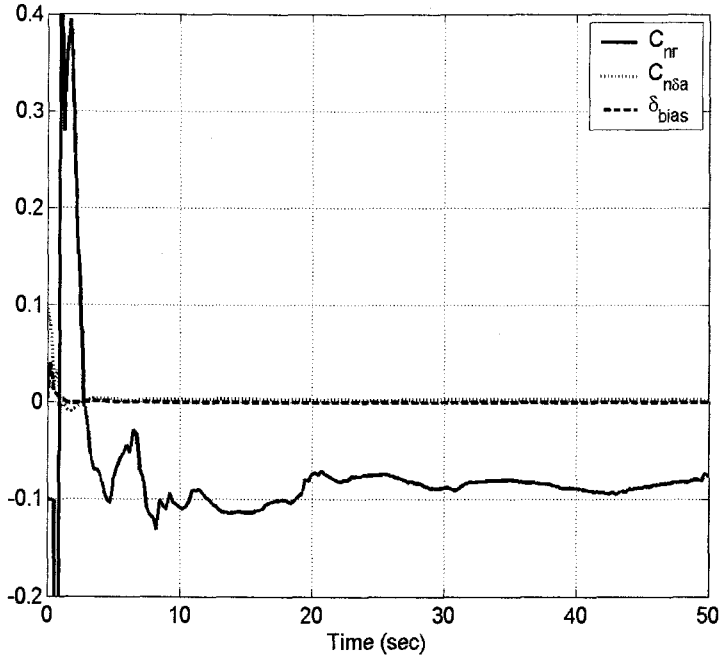

Figure 4.7 Estimated Yaw Aerodynamic Coefficients and Bias

Table 4.2 Estimated Model Coefficients

$C_{l\phi}$	–0.0244
C_{lp}	-0.0320
$C_{l\delta a}$	0.0050
C_{nr}	-0.0501
$C_{n\delta a}$	0.0014
δ_{bias}	–0.00017

The discrete time linear reduced order model is simulated with 1 second sampling, estimated aerodynamic coefficients and the control sequence in Figure 4.4. The model results are compared to the measured states of the test system in Figures 4.8 through 4.11. The reduced order model is able to capture the fundamental dynamics of the parafoil and payload. A bias in the body yaw rate of 2.5 deg/sec is visible in Figure 4.8.

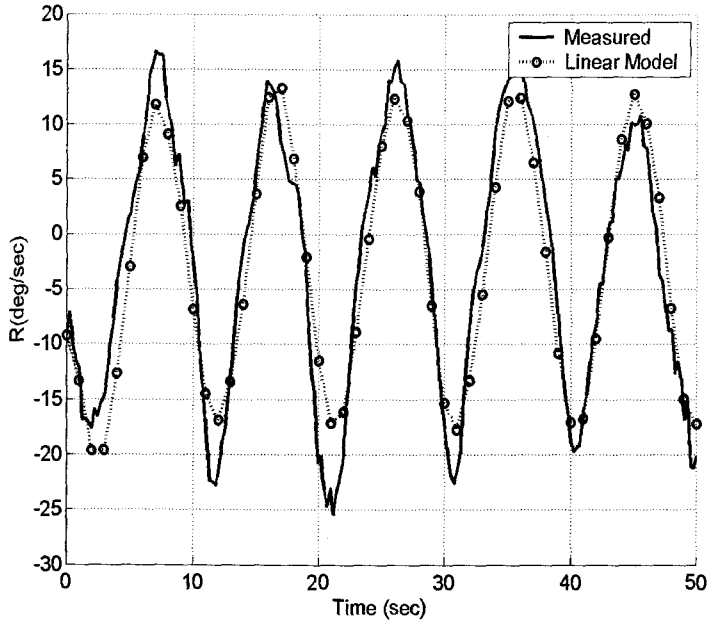

Fig 4.8 Comparison of Measured and Model Yaw Rate

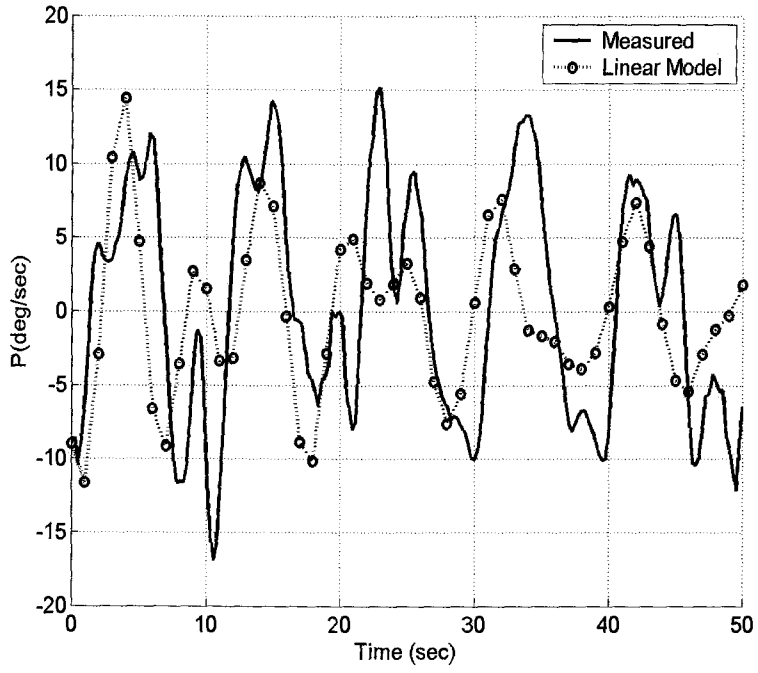

Figure 4.9 Comparison of Measured and Model Roll Rate

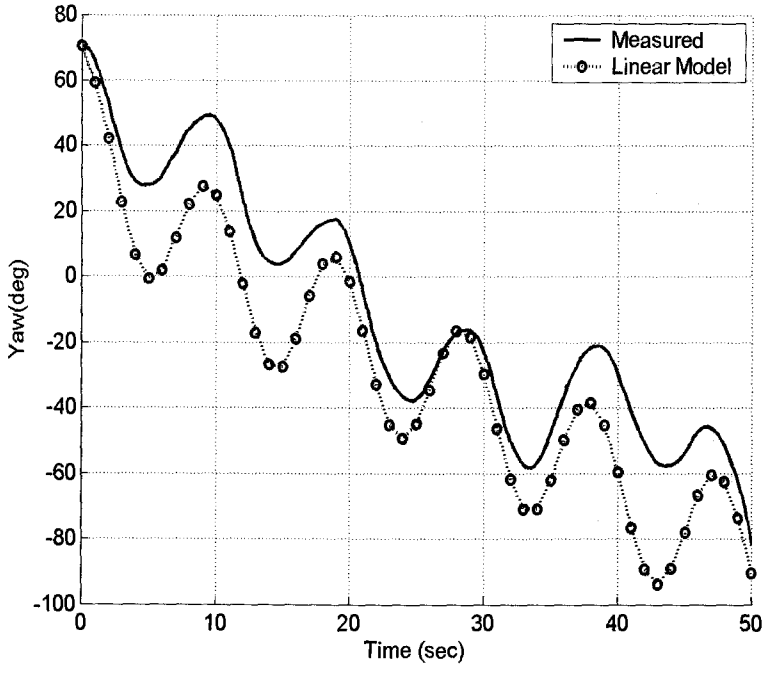

Figure 4.10 Comparison of Measured and Model Yaw Angle

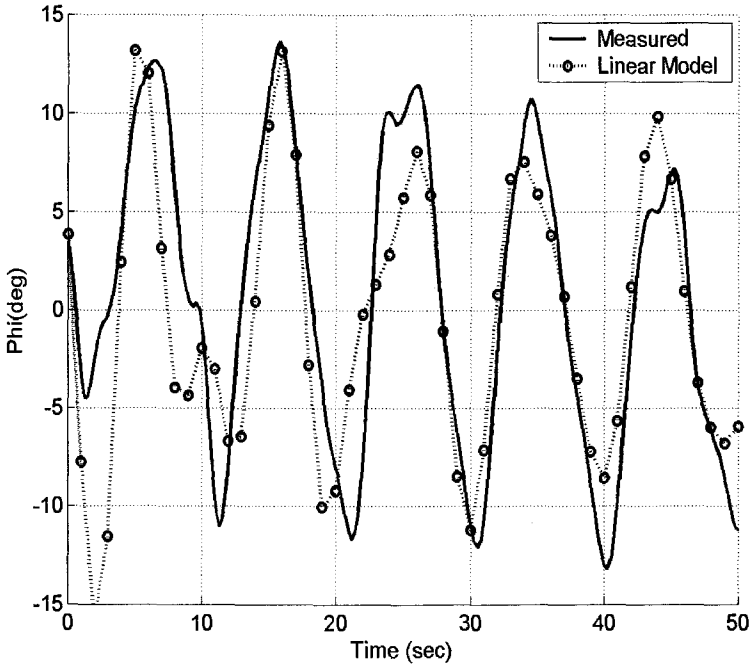

Figure 4.11 Comparison of Measured and Model Roll Angle

MODEL PREDICTIVE CONTROL RESULTS

The prediction of desired heading angle with third order Lagrange interpolating polynomials in Equation 38 requires four desired path points. The first point is defined as the current position of the parafoil and payload system during implementation of the controller. The second point is defined as the location along the desired path that is a distance σ ahead of the current position and called the intersect parameter. The third and fourth points are the next two desired path points. Figure 4.12 shows a desired path and the Lagrange interpolating polynomial found from Equations 38 through 48.

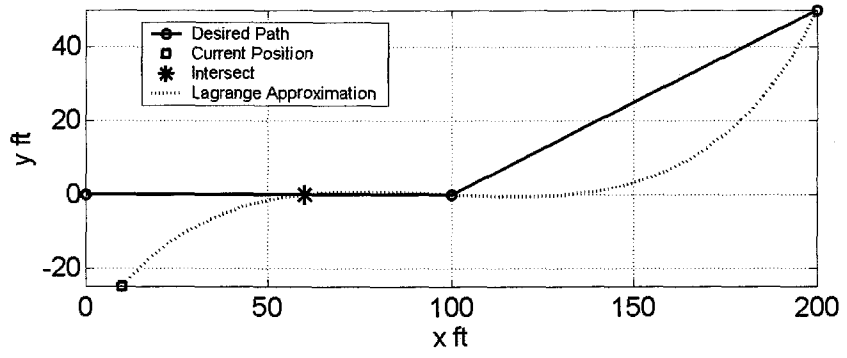

Figure 4.12 Lagrange Approximating Polynomial

The update rate of the model predictive controller was chosen to be 1 second and the linear model is converted to a discrete time system of the form in Equation 1 with a sampling period of 1 sec. The discrete time system matrices A, B, C and D required for the model predictive controller are given in Equations 53-56.

$$A = \begin{bmatrix} 0.4251 & 0 & 0.7677 & 0.0047 \\ 0.0551 & 1.0000 & 0.0236 & 0.7059 \\ -1.0084 & 0 & 0.3713 & 0.0070 \\ 0.0823 & 0 & 0.0593 & 0.4733 \end{bmatrix} \tag{54}$$

$$B = \begin{bmatrix} 0.0573 \\ 0.0945 \\ 0.1010 \\ 0.1693 \end{bmatrix} \tag{55}$$

$$C = \begin{bmatrix} 0 & 1 & 0 & 0 \end{bmatrix} \tag{56}$$

$$D = \begin{bmatrix} 0.0002 \\ -0.0122 \\ 0.0003 \\ -0.0216 \end{bmatrix} \tag{57}$$

The matrix R penalizing the control magnitude in the optimal control sequence is selected as an $H_p \text{x} H_p$ matrix with 0.35 on the diagonal and zeros everywhere else. The test parafoil system with the model predictive control law is simulated with prediction horizons of 2,3,4,5,10 and 20 and shown in Figures 4.13 and 4.14.

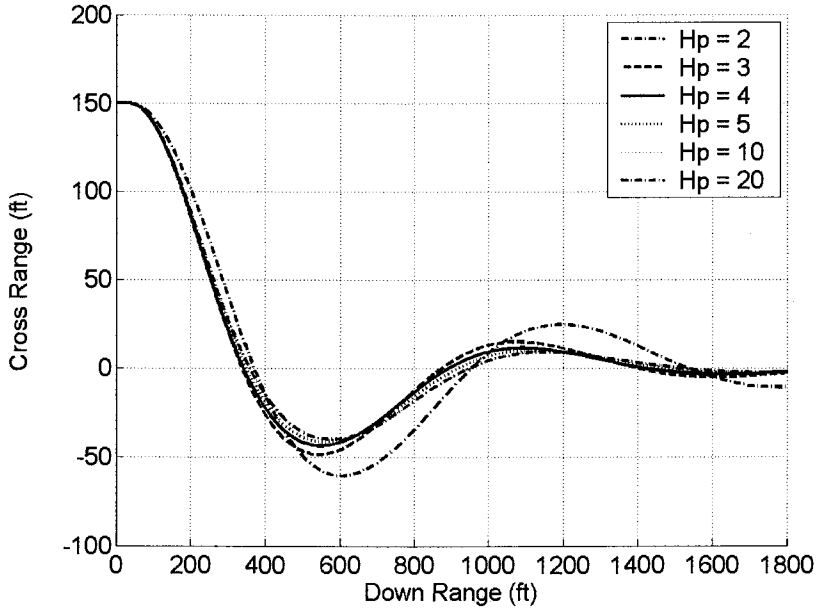

Figure 4.13 Simulated Tracking For Varying Prediction Horizons

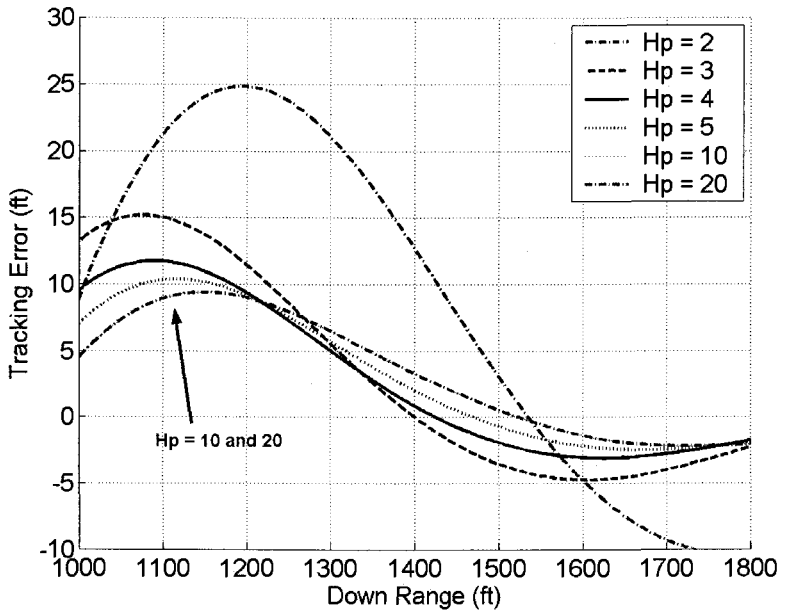

Figure 4.14 Tracking Error Over Final 800 feet

Tracking error is decreased as the prediction horizon H_p is increased from 2 to 10, however, as H_p is further increased from 10 to 20 no change in performance is observed and H_p is selected to be 10 for the test system control law. Results for the model predictive controller are shown in Figures 15 through 20 with H_p = 10 and σ = 100 ft. Figures 4.15 and 4.16 show the measured path of the parafoil and payload compared to a desired straight path and control with no wind. Control is initiated at the origin with the parafoil and payload initially traveling away from the desired path and 40 ft off line. The initial control response is large and negative corresponding to left braking and negative cross range. The parafoil has a maximum error of 75 feet at 100 ft down range then overshoots the desired by path by 39 feet at –510 feet down range before a final error of 9 feet at impact.

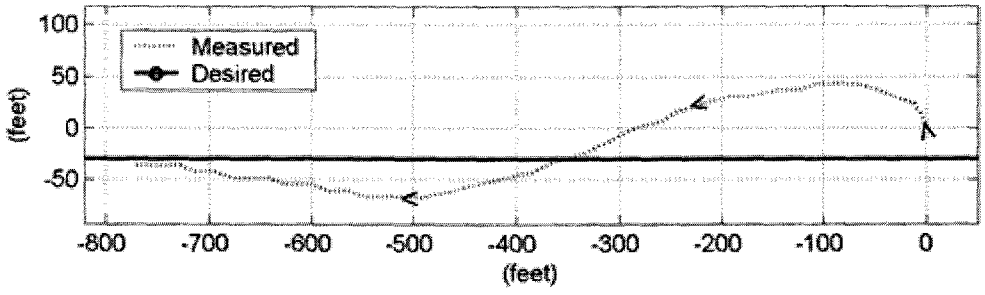

Figure 4.15 Controlled Straight Path With No Wind

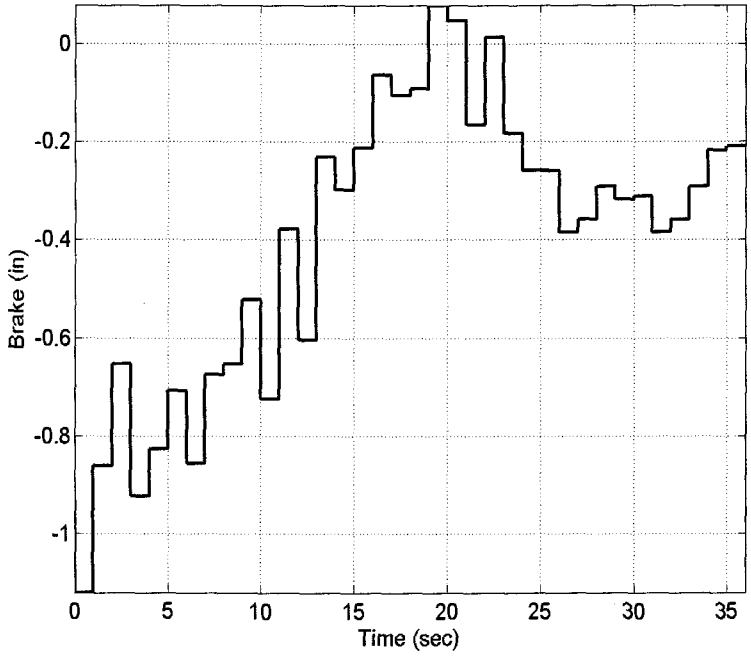

Figure 4.16 Straight Path Control Input With No Wind

Figures 4.17 and 4.18 show the measured path of the parafoil and payload compared to the desired straight path and control with a 12 ft/sec cross wind from positive to negative cross range. Control is again initiated at the origin with the parafoil and payload initially traveling away from the desired path and 100 ft off line. The parafoil has a similar oscillatory response with a maximum error of 119 feet at

230 ft down range as it overshoots the desired path. The parafoil turns back towards the desired path and comes within 18 feet before the wind pushes it further away. The final error at impact is 6 feet. The larger error from the crosswind is due to the difference in measured yaw angle and heading angle because of parafoil sideslip.

Figures 4.19 and 4.20 show the performance of the model predictive controller when tracking the more complicated S-shaped path. Control is initiated when the parafoil and payload are 210 ft offline. The maximum error during the flight is 45 feet at 550 feet down and –550 ft cross range. The model predictive controller is able to predict the required control input so that the parafoil and payload system are able to achieve close proximity to the desired points as they are passed.

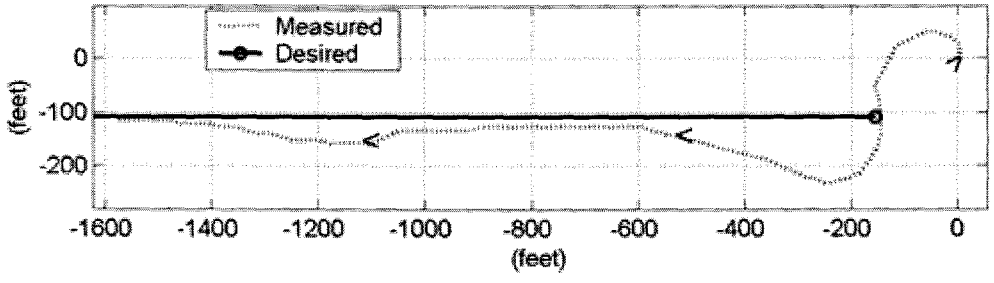

Figure 4.17 Controlled Straight Path With Cross Wind

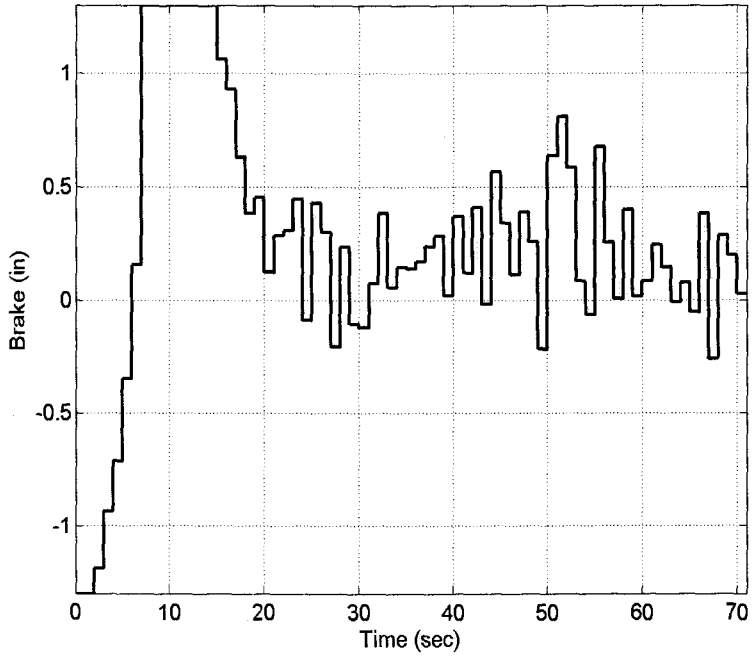

Figure 4.18 Straight Path Control Input With Cross Wind

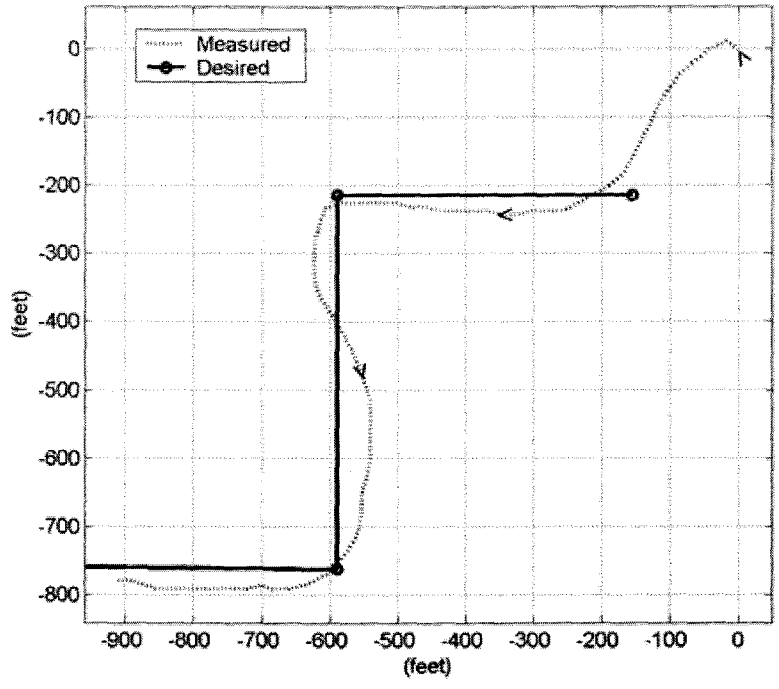

Figure 4.19 Controlled "S" Path With No Wind

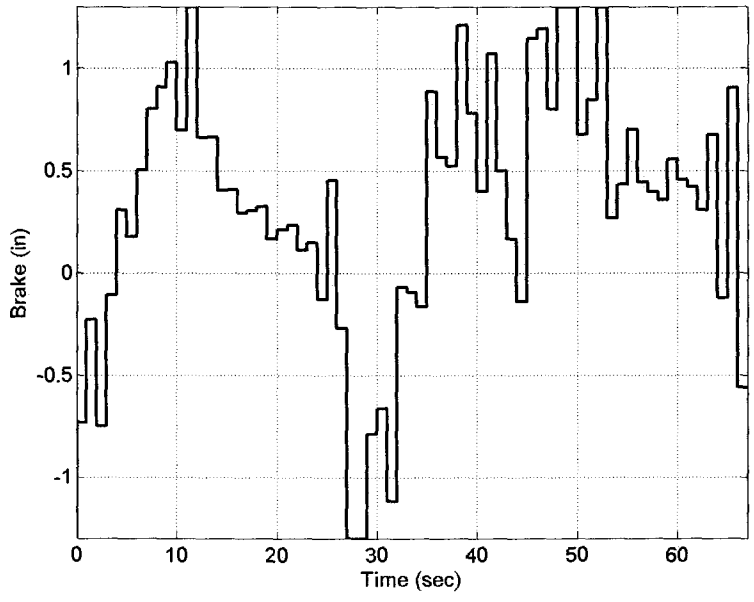

Figure 4.20 "S" Path Control Input With No Wind

CONCLUSIONS

A model predictive control strategy was developed for a parafoil and payload system. To support the flight control law, a reduced state linear model was created that uses roll angle, yaw angle, body roll rate, and body yaw rate of the parafoil and payload system. Application of the reduced order model requires the knowledge of five constant aerodynamic coefficients: $C_{l\phi}, C_{lp}, C_{l\delta a}, C_{nr}, C_{n\delta a}$ and a constant bias term δ_{bias}. A recursive weighted least squares estimation was used to estimate the six parameters. The estimated parameters and reduced state model were then compared with flight data and it was shown that they adequately modeled the parafoil and payload system. In order to use the reduced state linear model, the desired x-y trajectory was mapped into desired yaw angles using Lagrange interpolating polynomials and assuming a constant aerodynamic velocity. Three flight tests were

presented that showed model predictive control to be a natural and effective way to autonomously control the trajectory of a parafoil and payload system.

REFERENCES

[1] Mei, G., Kareem, A., "Model Predictive Control of Wind-Excited Building: Benchmark Study." *Journal Of Engineering Mechanic.*, vol. 130, pp. 459-465, Apr. 2004.

[2] Tsai, C. C., Huang, C. H., "Model Reference Adaptive Predictive Control for a Variable-Frequency Oil-Cooling Machine." *IEEE Transactions On Industrial Electronics.*, vol. 51, No. 2, pp. 330-339, Apr. 2004.

[3] Kvaternik, Piatak, Nion, Langston, Singleton, Bennett, Brown, "An experimental evaluation of generalized predictive control for tiltrotor aeroelastic stability augmentation in airplane mode of flight." *Journal of the American Helicopter Society*, v 47, n 3, July, 2002, p 198-208

[4] Ikonen, E., Najim, K., *Advanced Process Identification and Contro*l, Marcel Dekker Inc., New York, 2002.

[5] Faires, Burden, *Numerical Methods*, PWS Publishing Company, Boston, 1993.

[6] DeRusso, P., Roy, R., Close C., Desrochers A., *State Variables for Engineers*, John Wiley and Sons, Inc., New York, 1998.

GENERAL CONCLUSION

Using a 9 DOF flight dynamic model, it has been shown that parafoil and payload systems exhibit two basic modes of directional control, skid steering and roll steering for small brake deflections. For a particular configuration the mode of directional control depends on the angle of incidence and the panel orientation. The parafoil's mode of directional control is skid steering for canopies of "high" curvature and "smaller" negative angles of incidence. The mode of directional control transitions toward roll steering as the canopy curvature decreases or the angle of incidence becomes more negative. The mode of directional control also transitions away from the roll steering mode as the magnitude of the brake deflection increases and for "large" brake deflections most parafoils will always skid steer. Control reversal is usually undesirable and since parafoils have a tendency to skid steer for large brake deflections care needs to be taken to know and avoid the range of small braking that may induce roll steering. With careful design a parafoil and payload system can be properly modified so that roll steering can be eliminated all together.

Due to the fact that the parafoil canopy is a flexible membrane, deflection of the control arms on one side of the parafoil may also create tilt of the canopy. Both these effects combine to form the overall turning response. The parafoil and payload system discussed exhibits high lateral sensitivity to subtle canopy tilting. The high sensitivity to canopy tilt illustrates the importance of design parameters that alter the flexibility of the canopy namely suspension line quantity and arrangement and control line configuration. Canopy tilting can be exploited to eliminate conventional parafoil brakes for lateral direction control.

A common modeling technique for parafoils is to model the canopy as a rigid body. The affect of control inputs is idealized by deflection of parafoil brakes on the left and right side of the parafoil. Using a small parafoil and payload aircraft, glide rate and turn performance was measured and compared against a 9 DOF simulation model. The experimental aircraft control line connection to the parafoil consisted of

two lines on the outboard rear section of the parafoil and two lines on the outboard side of the parafoil causing both effective brake deflection along with canopy tilt. When contrasting the flight test data with simulation results, it was found that using only parafoil brake deflection in the model could not replicate the turn response of the aircraft. In fact, with only parafoil brake deflection in the model, steering in the opposite direction of the experimental data was exhibited. However, when both parafoil brake deflection and canopy tilt was included in the simulation model, turn performance of the system was well replicated. Thus, for controllable parafoil and payload systems a dynamic model should include the effect of right and left parafoil brake deflection and canopy tilt to replicate system turning dynamics.

Symmetric brake deflection and rigging angle modification both demonstrate the ability to effectively alter glide slope and total velocity of the system but in different methods. Rigging angle modification alters the glide slope and total velocity by largely altering the aerodynamic angle of attack while symmetric brake deflection increases the lift and only slightly increasing the angle of attack. In comparison symmetric brake deflections are more effective in altering the glide slopes and rigging angle modifications more effectively alter the total velocity. Conventional parafoil brakes for lateral and longitudinal control could be replaced by a combination of canopy tilting for lateral control and rigging angle modification for longitudinal control. A benefit of this alternate control method is the possibility of decoupling the lateral and longitudinal control mechanisms.

A model predictive control strategy was developed for a parafoil and payload aircraft. To support the flight control law, a reduced state linear model was created that uses roll angle, yaw angle, body roll rate, and body yaw rate of the parafoil and payload system. Application of the reduced order model required the knowledge of five constant aerodynamic coefficients: $C_{l\phi}, C_{lp}, C_{l\delta a}, C_{nr}, C_{n\delta a}$ and a constant bias term δ_{bias}. A recursive weighted least squares estimation was used to estimate the six parameters. The estimated parameters and reduced state model were then compared with flight data and it was shown that they adequately modeled the parafoil and

payload system. In order to use the reduced state linear model, the desired x-y trajectory was mapped into desired yaw angles using Lagrange interpolating polynomials and assuming a constant aerodynamic velocity. Three flight tests were presented that showed model predictive control to be a natural and effective way to autonomously control the trajectory of a parafoil and payload system.

BIBLIOGRAPHY

Brown, G.J, "Parafoil Steady Turn Response to Control Input," AIAA Paper 93-1241.

DeRusso, P., Roy, R., Close C., Desrochers A., *State Variables for Engineers*, John Wiley and Sons, Inc., New York, 1998.

Doherr, K., Schiling, H., "9 DOF-simulation of Rotating Parachute Systems," AIAA 12th. Aerodynamic Decelerator and Balloon Tech. Conf, 1991.

Ellison, R.K., "Determination of a parafoil Submunition Payload and Aerodynamic Control," AFATL-TR-85-74.

Faires, Burden, *Numerical Methods*, PWS Publishing Company, Boston, 1993.

Gupta, M., Xu, Z., Zhang, W., Accorsi, M., Leonard, J., Benney R., Stein., "Recent Advances in Structural Modeling of Parachute Dynamics," AIAA 2001-2030, AIAA 16th Aerodynamic Decelerator Systems Technology Conference, May 2001.

Hailiang, M., Zizeng, Q., "9-DOF Simulation of Controllable Parafoil System for Gliding and Stability," *Journal of National University of Defense Technology*, Vol. 16 No. 2, pp. 49-54, 1994.

Iacomini, C.S., Cerimele, C.J., "Lateral-Directional Aerodynamics from a Large Scale Parafoil Test Program," AIAA Paper 99-1731.

Iacomini, C.S., Cerimele, C.J., "Longitudinal Aerodynamics from a Large Scale Parafoil Test Program," AIAA Paper 99-1732.

Ikonen, E., Najim, K., *Advanced Process Identification and Control*, Marcel Dekker Inc., New York, 2002.

Iosilevskii, G., "Center of Gravity and Minimal Lift Coefficient Limits of a Gliding Parachute," *Journal of Aircraft*, Vol. 32 No. 6, pp. 1297-1302, 1995.

Jann, T., "Aerodynamic Model Identification and GNC Design for the Parafoil-Load-System ALEX," AIAA Paper 2001-2015.

Kvaternik, Piatak, Nion, Langston, Singleton, Bennett, Brown, "An experimental evaluation of generalized predictive control for tiltrotor aeroelastic stability augmentation in airplane mode of flight." *Journal of the American Helicopter Society*, v 47, n 3, July, 2002, p 198-208

Lissaman, P.B.S., Brown, G. J., "Apparent Mass Effects on Parafoil Dynamics," AIAA Paper 93-1236.

McCormick, B., "Aerodynamics and Aeronautics and Fight Mechanics", John Wiley and Sons Inc, New York, NY, 1979.

Mei, G., Kareem, A., "Model Predictive Control of Wind-Excited Building: Benchmark Study." *Journal Of Engineering Mechanic.*, vol. 130, pp. 459-465, Apr. 2004.

Slegers, N., Costello M., "Aspects of Control for a Parafoil and Payload System," Journal of Guidance, Control and Dynamics, Vol. 26, No. 6, December 2003.

Slegers, N., Costello M., "Comparison of Measured and Simulated Motion of a Controllable Parafoil and Payload System," AIAA Paper 2003-5611, 2003.

Tsai, C. C., Huang, C. H., "Model Reference Adaptive Predictive Control for a Variable-Frequency Oil-Cooling Machine." *IEEE Transactions On Industrial Electronics.*, vol. 51, No. 2, pp. 330-339, Apr. 2004.

Ware, G.M., Hassell, Jr., J.L., "Wind-Tunnel Investigation of Ram-Air_Inflated All-Flexible Wings of Aspect Ratios 1.0 to 3.0," NASA TM SX-1923,1969.

Wolf, D., "Dynamic Stability of Nonrigid Parachute and Payload System," *Journal of Aircraft*, Vol. 8 No. 8, pp. 603-609, 1971.

Wolfe, W.P., Peterson, C.W., "Modeling of Parachute Line Wrap," AIAA 2001-2030, AIAA 16th Aerodynamic Decelerator Systems Technology Conference, May 2001.

Zhu, Y., Moreau, M., Accorsi, M., Leonard J.,Smith J., "Computer Simulation of Parafoil Dynamics," AIAA 2001-2005, AIAA 16th Aerodynamic Decelerator Systems Technology Conference, May 2001.